United States Nuclear Regulatory Commission

Protecting People and the Environment

RIL 2021-07

ANL/EVS-20/18

RADIATION EFECTS ON CONCRETE

An Approach for Modeling Degradation of Concrete Properties

Manuscript Completed: December 21, 2020
Date Published: August 2021

Prepared by:
Y. Xi
Y. Jing
Department of Civil, Environmental and Architectural Engineering
University of Colorado
Boulder, CO 80309-0428

B. Biwer
Environmental Science Division
Argonne National Laboratory
Lemont, IL 60439

Madhumita Sircar, NRC
Technical Lead and Project Manager

Research Information Letter
Office of Nuclear Regulatory Research

Disclaimer

ABSTRACT

Evaluation of concrete and reinforced concrete structures in nuclear power plants under long-term irradiation is important to help ensure safe and reliable operation of nuclear reactors beyond a 60-year lifespan. A comprehensive framework of theoretical models was developed to predict the various properties and deformation of nuclear-irradiated concrete. The Generalized Self-Consistent (GSC) model and the Mori-Tanaka model were used to characterize the mechanical and transport properties of concrete with multiple phases and multiple-scale internal structures. The damage to the concrete's mechanical properties resulting from neutron irradiation and elevated temperature was estimated using a composite damage mechanics approach. A coupled damage-creep model of concrete was developed by employing the generalized Maxwell model combined with a damage model for the mechanical damage, and the composite damage model, for the effect of irradiation-induced damage, to evaluate the creep of concrete. The coupled damage-creep model was implemented in ABAQUS/standard via a custom subroutine. The transport of neutrons and gamma rays in degraded concrete was calculated using multi-group diffusion equations, taking into account the temperature gradient and the damage induced by neutrons. The transport properties of the degraded concrete were estimated by means of a cross-correlation theory using the mechanical properties of the degraded concrete. Finally, all models were combined and implemented in a finite element code. The capability of the code was demonstrated by a coupled radio-thermo-mechanical analysis to predict the long-term mechanical and transport responses of concrete. The results of the project represent a comprehensive framework that can be used as user-defined material models combined with commercial finite element software products for future application of numerical analysis of concrete and reinforced concrete structures in nuclear power plants. The case studies in the project provided sensitivity analyses of the influential material parameters on the properties of concrete. Future research topics to enable further development and validation of the present models are discussed.

FOREWORD

The Office of Regulatory Research (RES) of the U.S. Nuclear Regulatory Commission (NRC) initiated research on the effects of irradiation on concrete structures to support subsequent license renewal activities for nuclear power plants. The research was undertaken in response to a 2015 user need request from the Office of Nuclear Reactor Regulation (NRR). In Staff Requirements Memorandum SRM-SECY-014-0016, NRC directed the staff to keep the Commission informed regarding progress on concrete research activities, including the effects of irradiation on concrete. NUREG/CR 7153 Vol. 4, ‘Expanded Materials Degradation Assessment (EMDA): Aging of Concrete and Civil Structures,’ 2014, identified irradiation-related concrete degradation as an area of low knowledge and high significance. Such degradation has been identified as a potential issue for two-loop and three-loop pressurized water reactors because they accumulate higher neutron fluence in the concrete around the reactor pressure vessel during long-term operations.

The RES research program addresses technical issues for which uncertainties challenge applicants, as well as staff guidance and reviews.

The RES research activities on irradiation-induced concrete degradation include:

1. Review of radiation-induced concrete degradation and potential implications for structures exposed to high-level, long-term radiation in nuclear power plants, Argonne National Laboratory (ANL), NUREG/CR - 7280, July 2021.

2. English translation of the Japanese Nuclear Regulation Authority (JNRA)/MRI Report on concrete irradiation tests, December 2019. [ML19346E734]

3. Review and feedback on selected Electric Power Research Institute (EPRI) reports, October 2017.

4. Radiation evaluation methodology for concrete structures, Oak Ridge National Laboratory (ORNL), NUREG/CR - 7281, July 2021.

5. Radiation effects on concrete – An approach for modeling degradation of concrete properties, ANL and the University of Colorado, Research Information Letter Report, manuscript completed December 2020.

6. Limited experimentation, modeling, and numerical simulations of irradiated concrete including concrete-steel bonding and methodology for structural evaluation at ORNL (2018–2023).

7. In-house assessment of structural capacity (2019–2023).

8. Harvesting concrete exposed to operational radiation for confirmatory assessment of evidence of concrete damage and site-specific effects.

The research activities and reports on items 1–4 are complete. This report covers research activity 5. In this research, an integrated framework and multiscale and multiphase model have been developed for evaluating the degraded properties of irradiated concrete. Multiscale and multiphase modeling is important because various phases experience different degradation mechanisms, and damage must be tracked from nano-, micro-, and meso-structural scales. The approach for the coupled damage-creep modeling was selected because previous research indicated that creep may reduce the damage from radiation-induced expansion of aggregates. The research includes the coupled radio-thermo model for neutron and gamma transport, heat generation, and the potential change in thermal conductivity and neutron diffusion coefficient of the degraded concrete. No data is currently available on the effects of irradiation on the steel-concrete interface and bonding. As data becomes available, the model can be extended to include the interface transition zone in reinforced concrete.

The framework developed in this research integrates radiation-induced degradation phenomena and mechanisms. The modeling methods used are simple which can be applied for gaining insights into the degradation of concrete properties, distributions of neutron and gamma irradiation levels in concrete structures, and accumulation of heating inside the concrete structures. The models require sets of input parameters and certain material properties. For some properties or parameters, there is a lack of data, and at this time, the framework can be used for sensitivity analysis. Subsequent research needs to focus on characterizing those input parameters. In some cases, this may be done by using more complex modeling and analysis of radiation transport through concrete from which the range of the values for the degradation of those parameters and properties may be verified and calibrated. Also, relevant experimental data and data using concrete harvested from nuclear power plant is extremely valuable for validating the models.

TABLE OF CONTENTS

LIST OF FIGURES

LIST OF FIGURES (CONT.)

LIST OF FIGURES (CONT.)

LIST OF FIGURES (CONT.)

LIST OF TABLES

EXECUTIVE SUMMARY

Theoretical models were developed for analysis of the degradation of the mechanical and transport properties of concrete under nuclear irradiation. The models were implemented in finite element and finite difference codes as the basis for future applications to numerical analysis of concrete and reinforced concrete structures in nuclear power plants.

A theoretical model was developed for the prediction of the mechanical properties and expansion and shrinkage of nuclear irradiated concrete. The model can take into account the degradation mechanisms at multiscale levels and different spatial distributions of the multiphase constituents in concrete. As test data becomes available on the influence of radiation on the concrete–metal reinforcement interface, the model can be extended to include the interface transition zone in reinforced concrete.

In this study, concrete is considered as a multiphase composite with four different scale levels ranging from the meter scale level down to the nanometer level. The scale levels considered are concrete, mortar, cement paste, and clinker (to consider the chemical composition of different Portland cement types) in descending order of scale. The internal structures of concrete at the four scale levels were simplified by using two different models, the Mori-Tanaka model and the Generalized Self-Consistent (GSC) model, based on the structural features at each level. In practice, the obtained properties at the lower scale level can be used as the input for the composite at the upper scale level. In this case, the effective properties of clinker (at the lowest scale level) can be evaluated using the Mori-Tanaka model based on the known properties of its constituent phases. The obtained effective properties of clinker can be used as the input for the Mori-Tanaka model to calculate the effective properties of cement paste. The obtained effective properties of cement paste, in turn, can be used as the input for the GSC model of mortar. This process can be repeated, using the effective properties of mortar as input for the GSC model of concrete. In this manner, the multiscale and multiphase model can take into account the contributions of all constituent phases in the concrete material.

The volume fraction of each constituent phase was calculated based on either the concrete mix design or the hydration reactions of Portland cement. The responses of specific constituent phases, such as the aggregate or the cement paste, to nuclear irradiation and temperature at different scale levels were quantitatively characterized based on the collected test data or estimated based on available models. Damage development in the hardened cement paste in the nuclear irradiated concrete was calculated based on composite damage mechanics. The overall irradiation effect on concrete as a composite material can be calculated by considering the effects of the irradiation and temperature on each constituent phase at each scale level. The model was validated preliminarily with experimental data available in the literature for the modulus of elasticity of distressed concrete. Damage effects on creep and radiation transport in concrete were also included.

The creep of concrete was characterized by the generalized Maxwell model, first using a subroutine UMAT in ABAQUS and then combined with a damage model for the effect of irradiation-induced damage on creep of concrete. The transport characteristics of neutrons and gamma rays in damaged concrete were calculated using multi-group diffusion equations in which the transport parameters of concrete were modeled considering the damage induced by neutrons and the temperature gradient. The results obtained from the present diffusion models were compared with the results of the Monte Carlo N-Particle transport code (MCNP 6.2). Finally, a coupled radio-thermo-mechanical analysis was conducted for a case study, which combined all models developed in this study, including the multiscale and multiphase model for neutron-induced damage, the coupled damage-creep model, and the coupled radio-thermo model for neutron and gamma transport. The case study showed the capability of the models to estimate the long-term mechanical and transport response in concrete and provide a path forward in determining the state of concrete in nuclear power plants under normal operational conditions.

ACKNOWLEDGEMENTS

The work described in this report was sponsored by the U.S. Nuclear Regulatory Commission (NRC), Office of Nuclear Regulatory Research. The authors would like to thank Madhumita Sircar for her capable guidance and valuable comments as the NRC project manager. A number of NRC staff contributed constructive comments on draft versions of this report. Among those, we would like to offer special thanks to Andrew Prinaris, Jinsuo Nie, and Jose Pires for their enthusiasm and insightful observations.

ABBREVIATIONS AND ACRONYMS

CTE	Coefficient of linear thermal expansion
EHM	Equivalent homogeneous medium
GSC	Generalized Self-Consistent model
ITZ	Interface transition zone
NPP	Nuclear power plant
RPV	Reactor pressure vessel

Notations

K_i	Bulk modulus of phase *i*
G_i	Shear modulus of phase *i*
C_1, C_2, C_3	Equation coefficients for shear modulus
E_i	Elastic modulus of phase *i*
ν_i	Poisson's ratio of phase *i*
ε_i	Normal strain of phase *i*
f_i, f_p	Volume fraction of phase *i/p*
P	Interface pressure
P_c	Critical interface pressure
$\mathcal{N}$	Number of constituent phases in the composite
$\boldsymbol{I}$	Symmetric fourth−order unity tensor
$\boldsymbol{A_p}$	Fourth−order strain concentration tensor of phase *p*
$\boldsymbol{C_p}$	Stiffness tensor of phase *p*
$\boldsymbol{S_p}$	Fourth−order Eshelby tensor of phase *p*
θ, φ	Euler angles
α	Overall degree of hydration of the cement-based material
α_i	Degree of hydration for reacting compound *i* in Portland cement
W_i	Weight fraction for reacting compound *i* in Portland cement
w/c	Water-to-cement ratio
ρ	Density
V	Volume
W_s, W_c, W_w W_g	Weight per unit volume of concrete for sand, cement, water, and gravel
ε_u	Saturation value of dimensional change of aggregate
$\mathcal{A}$	Temperature-dependent crystallization efficiency parameter
$\mathcal{B}$	Normalization factor for neutron fluence

N	Neutron fluence
ε_{Ti}	Thermal expansion of the i^{th} constituent phase in concrete
α_i^T	Coefficient of linear thermal expansion (CTE) for the i^{th} constituent phase in concrete
δ	Volumetric strain
$\boldsymbol{\sigma}$	Stress tensor
$\boldsymbol{\varepsilon}$	Strain tensor
σ_r	Stress in the radial direction
σ_θ	Stress in the tangential direction
r	Location coordinate in the radial direction when the center of the inclusion is the origin of the system
r_s	Aggregate radius
r_n	Radius of yield surface at time t_n
I_1	First invariant of the stress tensor
J_2	Second invariant of the deviatoric stress tensor
α, k	Constants in Drucker-Prager plasticity
f_t	Tensile strength of concrete
f_c'	Compressive strength of concrete
f_{ct}	Tensile strength of cement paste
f_{cc}'	Compressive strength of cement paste
Δx	Thickness of the potential cracked zone
E_0	Elastic modulus of the intact material (instantaneous stiffness)
E_d	Elastic modulus of the fully distressed material
t	Time
t'	Time when loads are applied
Y	Relaxation modulus of elasticity
E_m	Elastic modulus of the spring in the element m
E_{end}	Steady-state elastic modulus
ψ	Creep coefficient
ψ_u	Ultimate creep coefficient
τ_m	Relaxation times of the element m
p_m	E_m/E_0
γ_m	Internal variable of the element m
T	Temperature
ΔT	Temperature increment

D	Scalar damage variable
D_{Rad}	Scalar damage variable due to nuclear irradiation
D_{Mech}	Scalar damage variable due to mechanical loads
$\boldsymbol{C}^{e}$	Elastic stiffness tensor
$\boldsymbol{\varepsilon}^{e}$	Elastic strain tensor
$\boldsymbol{\varepsilon}^{c}$	Creep strain tensor
ϵ_i	Principle strains
$\tilde{\epsilon}$	Equivalent tensile strain
$\boldsymbol{\epsilon}^{t}$	Tensile strain tensor
$\boldsymbol{\epsilon}^{c}$	Compressive strain tensor
κ	Threshold of damage in Mazars' damage model
d_t	A damage variable corresponding to tension
d_c	A damage variable corresponding to compression
α_t	*A* weighting coefficient calculated from tensile strain
α_c	*A* weighting coefficient calculated from compressive strain
A_t, B_t, A_c, B_c	Characteristic parameters of the material in Mazars' damage model
n	Angular neutron density
v	Neutron speed
Σ_t	Total macroscopic cross section
Σ_s	Macroscopic scattering cross section
$\boldsymbol{S}$	Internal neutron source term
$\boldsymbol{r}$	Position vector
$\mathcal{E}$	Neutron energy
$\widehat{\boldsymbol{\Omega}}$	Unit vector describing the direction of particle motion
ϕ_i	Scalar neutron flux of group *i*
$\mathcal{D}$	Neutron diffusion coefficient
Σ_a	Macroscopic absorption cross section
Σ_R	Macroscopic removal cross section
Σ_{s12}	Macroscopic fast to thermal group-transfer cross section
x	Location
c_p	Specific heat capacity
k	Thermal conductivity
Q	Volumetric heat source
Σ_c	Macroscopic capture cross section of the transport media for neutrons

$\mathcal{E}_b$	Binding energy for capture reaction of neutrons
d	Volume fraction of the inclusion (distressed phase)
k_0	Thermal conductivity of the intact material
k_d	Thermal conductivity of the fully distressed material
$\mathcal{D}_0$	Neutron diffusion coefficient of the intact material
$\mathcal{D}_d$	Neutron diffusion coefficient of the fully distressed material
Φ	Scalar photon flux
c	Light speed
$\mathbb{D}$	Photon diffusion coefficient
μ_a	Photon absorption coefficient
$\boldsymbol{S_\gamma}$	Internal gamma-ray photon source term
μ_g	Photon attenuation coefficient of group *g* in cm^{-1}
$\mu_{sg'g}$	Photon group-transfer coefficient from group *g′* to group *g*
$\Sigma_{\gamma ig}$	Macroscopic neutron capture cross section from neutron group *i* to photon group *g*
Σ_{ing}	Macroscopic fast neutron inelastic scattering cross section to photon group *g*
Ψ_g	Photon energy fluence in group *g*
$\mathcal{E}_{\gamma g}$	Photon energy in group *g*
$\frac{\mu_{en}}{\rho}$	Mass energy absorption coefficient
μ_{ag}	Linear energy-absorption coefficient for gamma ray photons in group *g*
$\mathbb{D}_0$	Photon diffusion coefficient of the intact material
$\mathbb{D}_d$	Photon diffusion coefficient of the fully distressed material

Notations used in Appendix are not listed. They are listed after the equations.

1 INTRODUCTION

As a fundamental building material, concrete is one of the primary structural materials used in the construction of commercial nuclear power plants (NPPs). It is used in such applications as building foundations, reactor containment, shielding applications, and for support of the reactor pressure vessel (RPV).

The degradation of concrete over time at NPPs has been well studied in most areas and is dependent on its environment (Naus 2007). Concrete degradation issues include chemical attack, thermal cycling, fatigue/vibration, irradiation, and steel reinforcement problems such as loss of bonding, loss of prestress, and corrosion. Until recently, concrete degradation due to irradiation has not been a significant component of aging management programs at U.S. NPPs (NRC 2010, 2017).

A review of the existing data on the irradiation of concrete was conducted to understand the potential effects relevant to long-term commercial NPP operation in the U.S. (Biwer et al. 2020). Information from degradation studies provide some insight as to the effects of neutron and gamma radiation on concrete under light-water reactor operating conditions, but data is sparse and does not cover all conditions or confounding factors. In addition, the ability to translate the impacts of radiation at the nano- and micro-meter scale levels to the NPP component structural level is needed, as explained below. This study builds that translational framework through the development of a material model for the mechanical behavior of concrete exposed to radiation for long-term operation. Information from our earlier review (Biwer et al. 2020) will be used as a guide in parameter development for use at the smaller scales.

As shown in Figure 1-1, concrete is a multiphase heterogeneous material with constituent phases spanning several scale levels from C-S-H (calcium silicate hydrates) at the nanometer level to the crystal phases at the micrometer level such as CH (calcium hydroxide) to sand particles and gravel at the millimeter level (referred to as the meso-scale level). The constituent phases respond to nuclear irradiation differently and thus can affect the overall response of concrete to nuclear radiation.

The multiscale method for characterizing complicated nuclear irradiation processes in concrete is to separate the problem into various scale ranges, each covering the mechanisms acting at one of the scale ranges. Material parameters that appear to be not clearly defined can be studied based on the dominant physical mechanisms and formulated separately. These separately formulated parameters can then be applied in the multiscale model. There are two major advantages of this multiscale modeling. 1) It follows the inherent logic of physical phenomena to be described. Degradation of concrete under nuclear irradiation involves various mechanisms acting over a broad range of scales, from the nanometer to the meter level such as creep, shrinkage, thermal expansion, and the distresses due to neutron and gamma irradiation. Therefore, multiscale modeling is necessary for prediction and simulation of the degradation process. 2) It separates controlling parameters in the degradation processes into several components such that each parameter has a specific physical meaning. The model at each scale level is based only on mechanisms which are active on that level, and models at different scale levels serve as links in the entire chain of the multiscale model (Xi et al. 2000).

The multiscale modeling approach has been used for different effective properties of concrete under combined environmental and mechanical loadings, such as elastic properties and transport properties. In this study, a micro-mechanical model, called the Mori-Tanaka model, and a composite mechanics model, called the Generalized Self-Consistent (GSC) model, will be used to develop a multiscale and multiphase material model, which will provide material parameters for finite element analysis at the structural level, as shown in Figure 1-1 and **Error! Reference source not found.**. More details will be provided in the next chapter. The micro-mechanical and composite models, including the damage mechanisms of the multiscale constituent phases in concrete under nuclear irradiation, can provide an integrated approach to studying the effects of nuclear irradiation and concrete design parameters on the concrete properties.

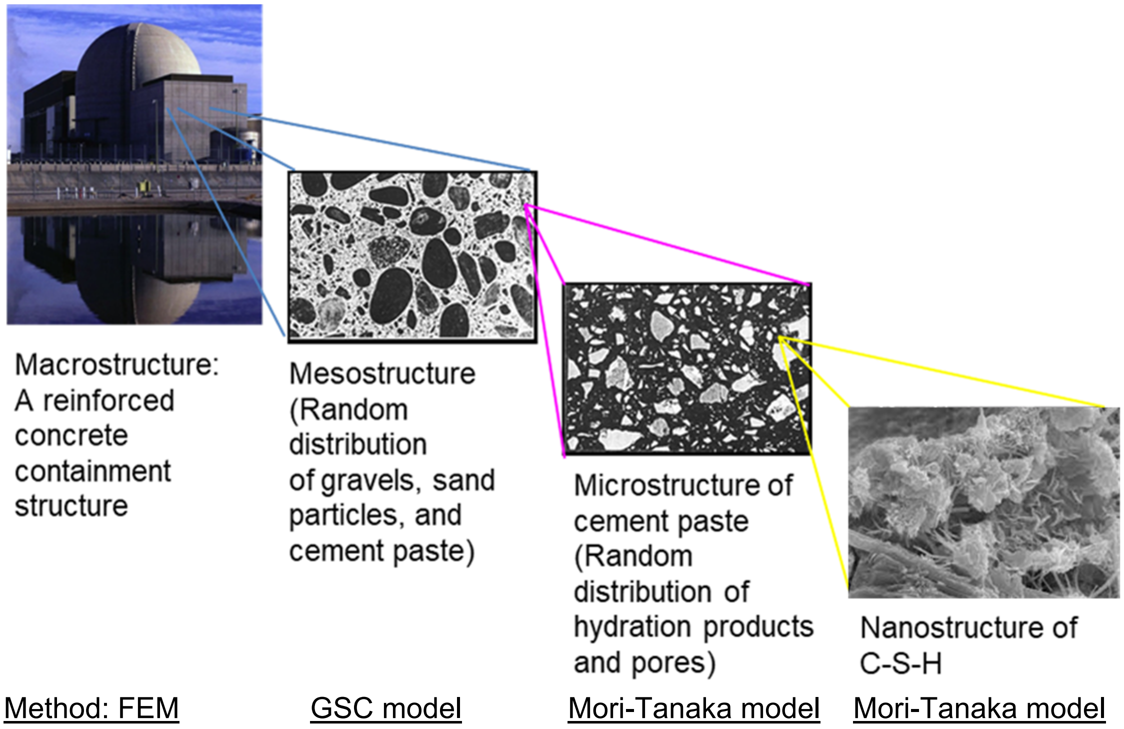

Figure 1-1 Schematic illustration of concrete internal structure

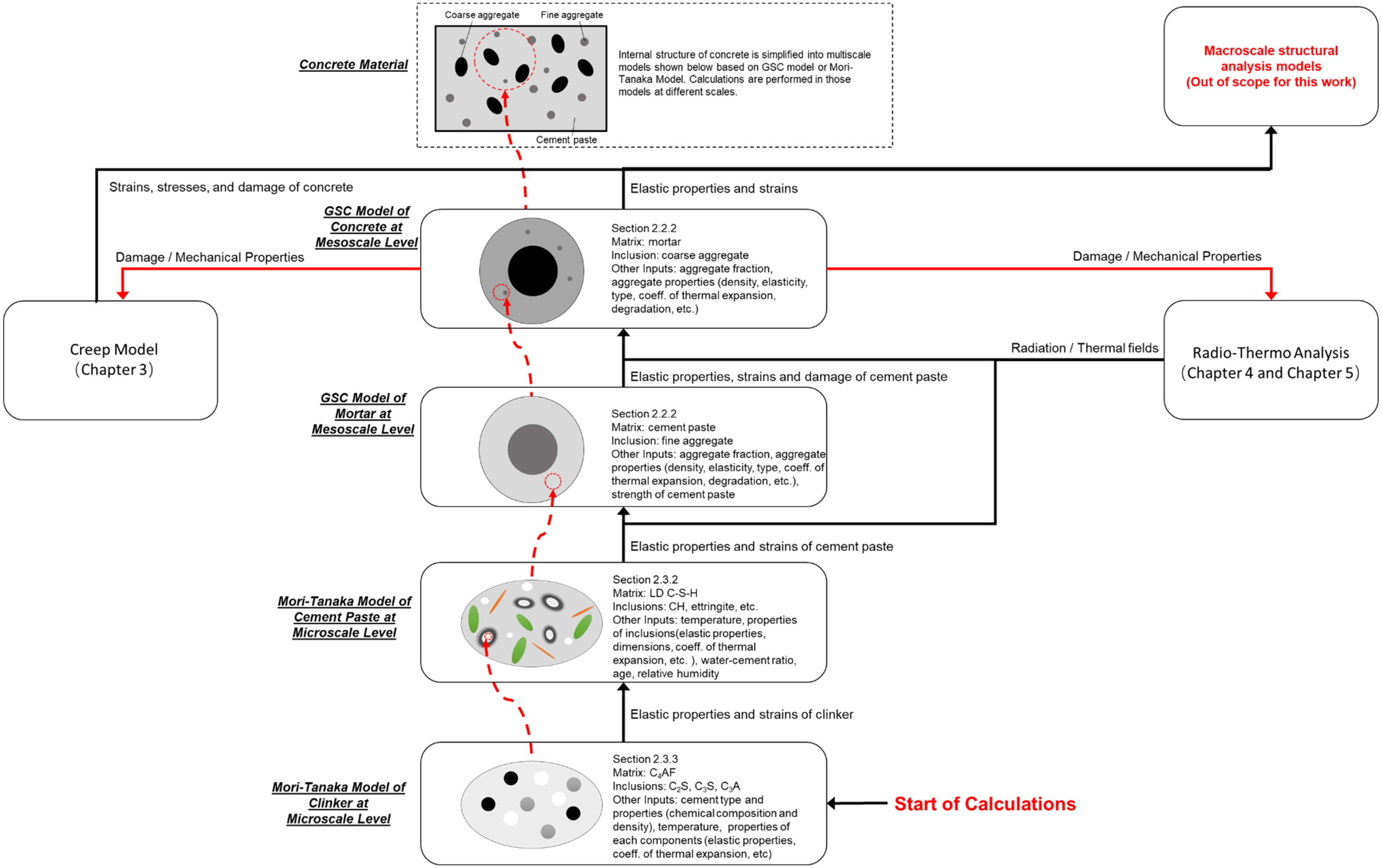

Figure 1-2 Schematic illustration of the multiscale model for concrete degradation

2 MULTISCALE AND MULTIPHASE MODEL OF CONCRETE

Since concrete is a multiphase heterogeneous material with constituent phases spanning several scale levels, the constituent phases respond to nuclear irradiation differently and thus generate different types of damage. In a reinforced concrete structure, the models developed in the present study are for structural concrete with degradation due to nuclear irradiation. A separate model for degraded steel will need to be developed. The interface transition zone (ITZ) between the steel and concrete may behave differently from bulk concrete under nuclear irradiation, and thus, the ITZ needs to be studied experimentally first, and then the test data can be used to calibrate the present models so that the models can be used for the ITZ.

The internal structures of concrete at different scale levels can be simplified. Available analytical models in composite mechanics and/or micromechanics can be used to calculate the effective properties of the composite based on the properties of the constituents. The advantages of the multiscale method were already discussed in Chapter 1. In this chapter, the Generalized Self-Consistent (GSC) model and the Mori-Tanaka model are introduced, and a description of how to use these two methods to characterize the internal structures of concrete, cement paste, and cement clinker will be given; and then, the reduction of the modulus of elasticity of the composite material can be calculated for use in structural analyses.

Figure 2-1 shows the overall scheme of the multiscale and multiphase model of concrete. The multiscale and multiphase model uses concrete design parameters as input (Section 2.6) so that the model can be applied to various concrete materials with different mix designs used in different nuclear power plants. The damage of concrete due to nuclear irradiation is estimated using a composite damage mechanics approach as shown in Section 2.5.2.3. After the multiscale and multiphase model is established, a parametric analysis of the model input parameters is performed in this chapter to analyze their effects on the degradation and deformation of concrete under nuclear irradiation.

2.1 Multiscale Model for the Internal Structure of Concrete

In this study, concrete is considered as a multiphase composite with four different scale levels. The scale levels address concrete, mortar, cement paste, and clinker as shown in Figure 2-2. The internal structures of concrete at the four scale levels were simplified by using two different models based on the structural features at the four levels. These two models are the Mori-Tanaka model and the GSC model, and they are used to determine the effective properties of the composite at each scale.

The four scale levels will be integrated in the following way. The obtained properties at the lower scale level will be used as the input for the composite at the upper scale level. For example, the effective properties of clinker (at the lowest scale level) can be evaluated using the Mori-Tanaka model based on the known properties of its constituent phases. As shown in Figure 2-2, the obtained effective properties of clinker will be used as the input for the Mori-Tanaka model to calculate the effective properties of cement paste. The obtained effective properties of cement paste will then be used as the input for the GSC model of mortar. This process will be repeated at each scale until the largest scale level is reached. In this manner, the multiscale and multiphase model can take into account the contributions of all constituent phases in the concrete material. The detailed descriptions of the models at all scale levels are provided in Sections 2.2 and 2.3.

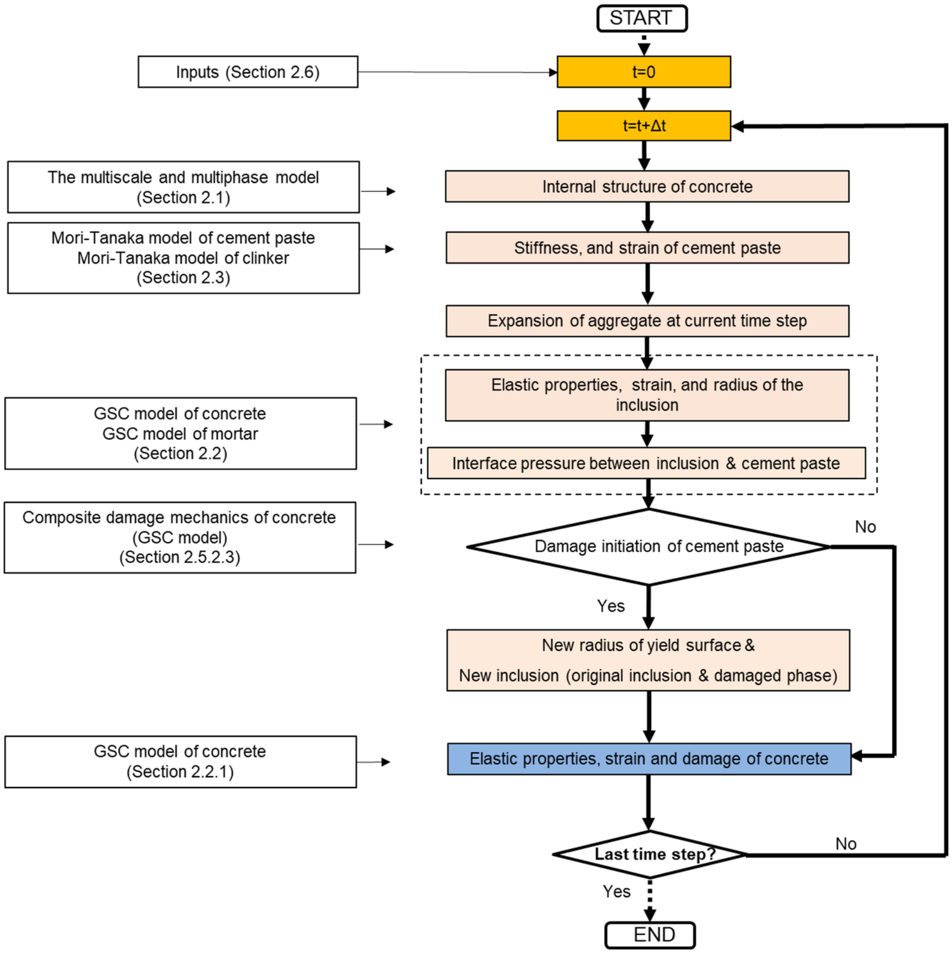

Figure 2-1 Calculation flowchart for multiscale and multiphase model of concrete

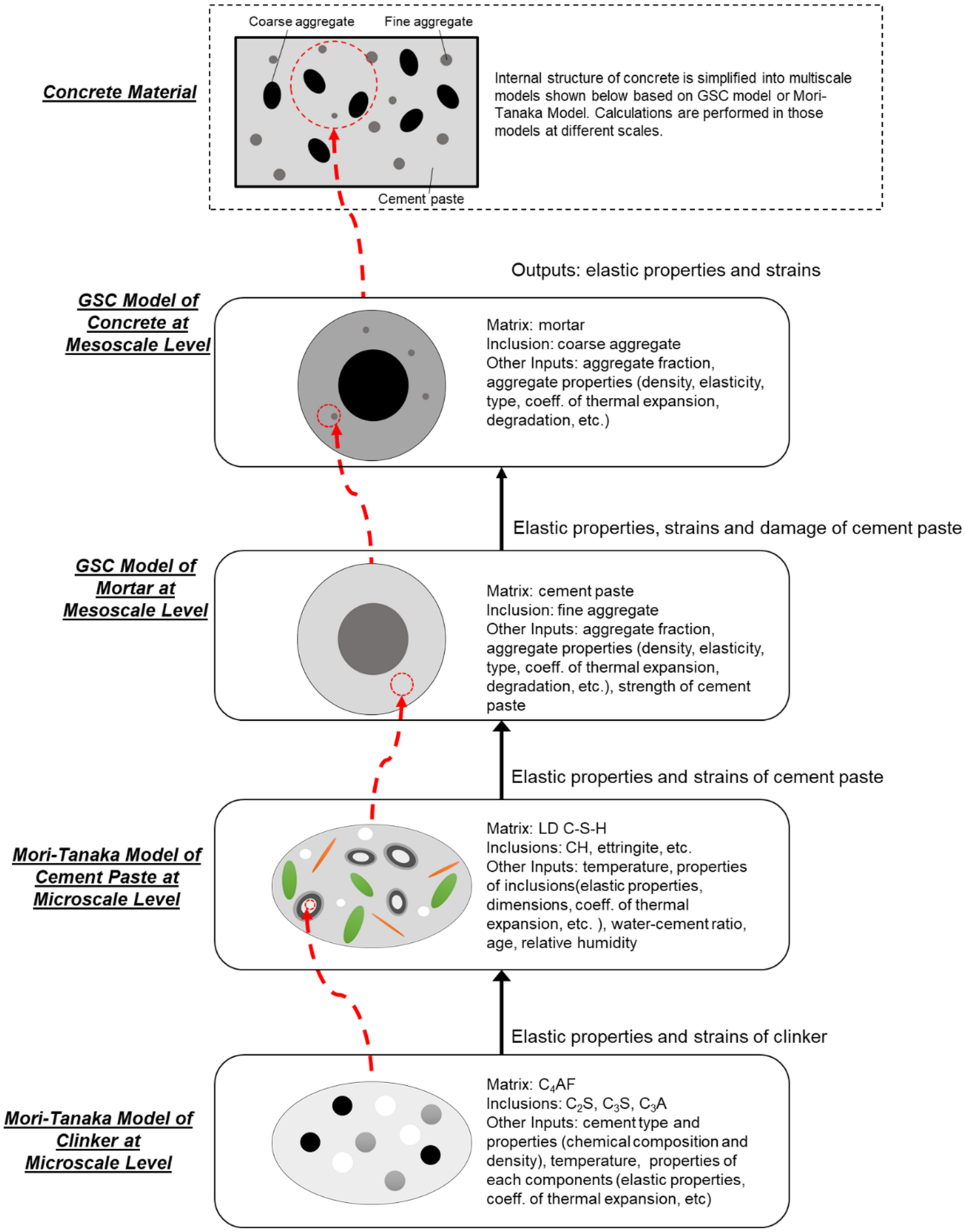

Internal structure of concrete is simplified into multiscale models shown below based on GSC model or Mori-Tanaka Model. Calculations are performed in those models at different scales.

Matrix: mortar
Inclusion: coarse aggregate
Other Inputs: aggregate fraction, aggregate properties (density, elasticity, type, coeff. of thermal expansion, degradation, etc.)

Matrix: cement paste
Inclusion: fine aggregate
Other Inputs: aggregate fraction, aggregate properties (density, elasticity, type, coeff. of thermal expansion, degradation, etc.), strength of cement paste

Matrix: LD C-S-H
Inclusions: CH, ettringite, etc.
Other Inputs: temperature, properties of inclusions(elastic properties, dimensions, coeff. of thermal expansion, etc.), water-cement ratio, age, relative humidity

Matrix: C_4AF
Inclusions: C_2S, C_3S, C_3A
Other Inputs: cement type and properties (chemical composition and density), temperature, properties of each components (elastic properties, coeff. of thermal expansion, etc)

Figure 2-2 Schematic view of the multiscale model for concrete

2.2 Mesostructure of Concrete

At the mesoscale level, concrete can be considered as a matrix-inclusion composite. Various sizes of large aggregates are embedded in the mortar and can be treated as inclusions. Similarly, for the mortar, the fine aggregates can be considered as the inclusions where the cement paste is the matrix. With this approach, these two scale levels can be modeled using the GSC model to estimate the effective properties of the mortar, and subsequently, the effective properties of the concrete.

2.2.1 Generalized Self-Consistent Model

At the millimeter scale (called mesoscale), the concrete contains sand and gravel particles (fine and coarse aggregates). In order to simplify the mesostructure of composite materials, many composite models have been proposed over the years. The GSC model is one of them. The GSC model was first developed by Christensen (1979) for the effective bulk modulus and thermal conductivity of composite materials. In this model, a heterogeneous composite material with two phases can be partitioned into different regions or elements, as shown in Figure 2-3 (a). The scales of the elements should be much smaller than that of the whole composite material. The sizes of the elements could be different, but the volume fractions of the phases in each element are the same. This partitioning of the internal structure can be further simplified by considering each element to have a spherical shape that can vary in size, and thus the internal structure of each element is a concentric layered sphere, as shown in Figure 2-3 (b). This configuration requires a specific size distribution of elements such that each element has the same internal structure, while the smaller elements fill the gaps between adjacent elements. Therefore, a broad and smooth particle size distribution is required. Since the volume fractions of the constituent phases (inclusion and matrix) in each element are the same, the ratios of the radius for the layers in each element are constants and do not depend on the absolute size of the elements. Under the concentric spherical system, the strain and stress components can be simplified from three dimensions to one dimension.

It should be emphasized that there is a strong phase association in the GSC model. The inclusions can be randomly distributed particles, and the matrix must be the phase surrounding the inclusions. As a result, the GSC model is good for characterizing those materials with strong phase association features, such as the coarse and fine aggregate particles randomly distributed in concrete. The aggregates in concrete are not like crystalline needles and plates, and they usually have low angularities; thus, the spherical model can be used to simulate the internal structure of concrete. Other suitable models are available for inclusions with large angularities, which are described in the next section together with cement paste.

In the GSC model, first, the “three-phase model” shown in Figure 2-3(c) is solved following Christensen (2005), which is a basic element in the internal structure shown in Figure 2-3(b). In Figure 2-3(c), the inclusion and the matrix are the two constituent phases, and the effective medium is the material outside of the basic element, which is a combination of the two phases; thus, the effective medium represents the composite material.

This method has been used in many studies on the durability issues of concrete, such as the shrinkage of concrete (Xi and Jennings 1997), thermal conduction of concrete (Meshgin and Xi 2013), moisture diffusion in concrete (Eskandari-Ghadi et al. 2013), and damage under high temperature (Lee et al. 2009). The model predictions showed good agreement with the experimental results. The model for the shrinkage of hardened cement paste and concrete developed by Xi and Jennings (1997) can also be used to predict the expansion of any heterogeneous multiphase medium. As shown later, the dominant damage mechanism of concrete under nuclear irradiation is the mismatch between volume changes of its components. Thus, the GSC model for effective volumetric expansion of the composite based on the volumetric expansions of the constituent phases will be very useful in this study.

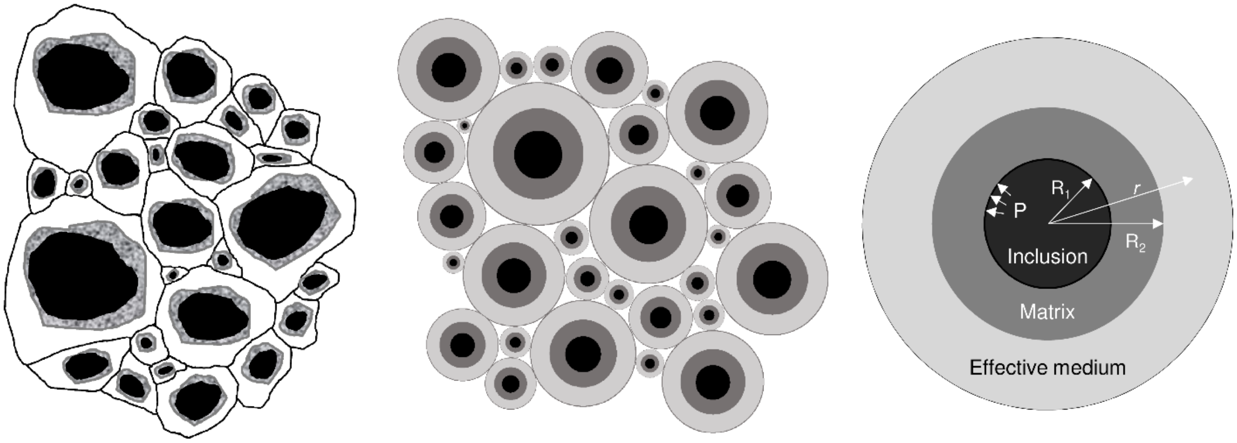

(a) (b) (c)

Figure 2-3 Multiphase GSC model: (a) partitioning multiphase composite into different elements; (b) partitioning multiphase composite using spherical elements; (c) internal structure of each element (Jing and Xi 2017)

The goal of the GSC model is to calculate the effective properties of the composite using the properties and proportions of its constituents. Specifically for this study, as shown in Figure 2-1, the effective properties such as effective modulus of elasticity and overall expansion or shrinkage of the concrete can be calculated using the strains and elastic moduli of the constituent phases. For example, the effective strain, bulk modulus, and shear of concrete can be calculated based on the GSC model using Equation (2-1), Equation (2-2), and Equation (2-3). These three equations will be used in later sections. The derivation details are shown in Appendix A.1

$$\varepsilon_{eff} = \frac{K_1 \varepsilon_1 f_1 (3K_2 + 4G_2) + K_2 \varepsilon_2 (1 - f_1)(3K_1 + 4G_2)}{K_2(3K_1 + 4G_2) - 4 f_1 G_2 (K_2 - K_1)} \tag{2-1}$$

$$K_{eff} = K_2 + \frac{f_1 (K_1 - K_2)}{1 + (1 - f_1)\dfrac{K_1 - K_2}{K_2 + \frac{4}{3} G_2}} \tag{2-2}$$

$$C_1 \left(\frac{G_{eff}}{G_2}\right)^2 + 2C_2 \left(\frac{G_{eff}}{G_2}\right) + C_3 = 0 \tag{2-3}$$

where

K_i = bulk modulus of phase *i* (MPa),

G_i = shear modulus of phase *i* (MPa),

ε_i = normal strain of phase *i* (dimensionless),

f_i = volume fraction of phase *i* (dimensionless), and

C_1, C_2, C_3 = equation coefficients (dimensionless), their expressions can be found in Appendix A.1 .

The subscript i with a value of 1, 2, or eff represents the inclusion, matrix, or effective medium, respectively. Determination of f_i can be found in Section 2.4 .

When any phase in the composite material shown in Figure 2-3(c) deforms and the deformations of the constituent phases do not match each other, called volumetric mismatch, there will be a nonzero internal pressure at the interfaces. In this case, there will be a pressure (P) at the inclusion-matrix interface, which is solved in Appendix A.1 .

$$P = \frac{12K_1K_2G_2(1-f_1)}{K_2(3K_1+4G_2)-4f_1G_2(K_2-K_1)}(\varepsilon_1-\varepsilon_2) \tag{2-4}$$

This equation will be discussed and used in later sections for the interface pressure generated by the expansion of aggregates due to, for example, neutron irradiation.

The "three-phase model" (the three phases are the inclusion, the matrix, and the effective medium as shown in Figure 2-3(c)) was generalized further and applied to composite materials composed of any number of phases. Figure 2-4 illustrates the basic idea of the generalization from three-phase to $\mathcal{N}$-phase. A recursive method can be used for a multiphase composite based on the multi-layered concentric spherical model. The general forms of the effective bulk modulus and the effective shrinkage (or expansion) of a composite material made of $\mathcal{N}$ constituent phases ($\mathcal{N} \geq 2$) can be obtained as follows (Xi and Jennings 1997):

$$(K_{eff})_i = K_i + \frac{c_{i-1,i}\left[\left(K_{eff}\right)_{i-1} - K_i\right]}{1+\left(1-c_{i-1,i}\right)\dfrac{\left(K_{eff}\right)_{i-1}-K_i}{K_i+\frac{4}{3}G_i}} \tag{2-5}$$

$$(\varepsilon_{eff})_i = \frac{\left(K_{eff}\right)_{i-1}(\varepsilon_{eff})_{i-1}c_{i-1,i}(3K_i+4G_i) - K_i\varepsilon_i(1-c_{i-1,i})\left[3\left(K_{eff}\right)_{i-1}+4G_i\right]}{K_i\left[3\left(K_{eff}\right)_{i-1}+4G_i\right]-4c_{i-1,i}G_i\left[K_i-\left(K_{eff}\right)_{i-1}\right]} \tag{2-6}$$

where $c_{i-1,i} = \frac{\sum_{j=1}^{i-1} f_j}{\sum_{j=1}^{i} f_j}$ if $i \neq \mathcal{N}$; $c_{i-1,i} = 1 - f_i$ if $i = \mathcal{N}$

$$(K_{eff})_1 = K_1;\ (\varepsilon_{eff})_1 = \varepsilon_1$$

The N-phase model is used to take into account the effect of damage in the cement paste shown in Section 2.5.2.3. In this case, the aggregate as the core is phase 1, the damaged cement paste as the first layer is phase 2, the original cement paste as the second layer is phase 3, and the effective medium is the degraded cement paste to be calculated.

In the literature, available test data are for the Young's modulus of concrete, and available effective models for composite materials are for the bulk modulus and the shear modulus. So, for the purposes of comparing the experimental data with theoretical predictions, the effective Young's modulus E of concrete is obtained based on the effective bulk modulus from Equation (2-2) and the effective shear modulus from Equation (2-3), as shown in Equation (2.7). On the other hand, these two effective moduli of a composite can be determined based on the known Young's moduli and Poisson's ratios of the constituents as shown in Equations (A-29) to (A-33) in Appendix A.1

$$E_{eff} = \frac{9K_{eff}G_{eff}}{3K_{eff} + G_{eff}} \tag{2-4}$$

More details about how to calculate the quantities in the above equation can be found in Appendix A.1.

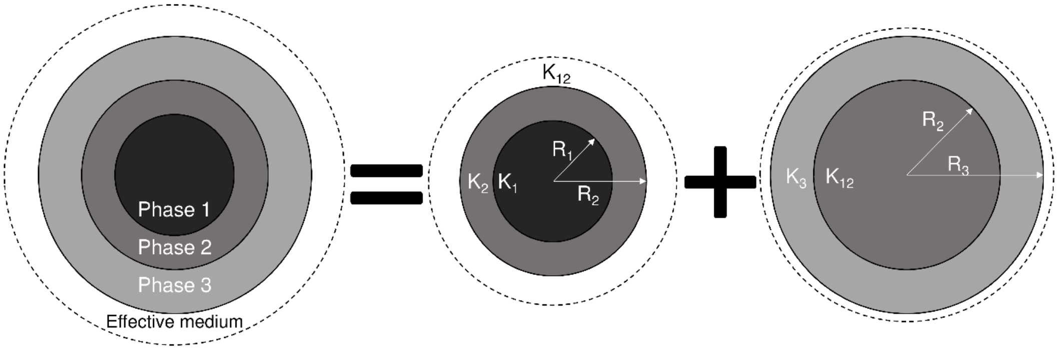

Figure 2-4 Generalization of the three-phase model to a multiphase model

2.2.2 Mesoscale Models for Concrete and Mortar

To reiterate, two scale levels are considered. The first one at the mesoscale level is concrete, in which the coarse aggregates are inclusions, the mortar is the matrix, and the GSC model is used for determining the effective properties of concrete. The second one is the mortar, in which the fine aggregates are inclusions, the cement paste is the matrix, and the GSC model is used for determining the effective properties of mortar.
Figure 2-5 shows the theoretical model for the two scale levels for concrete.

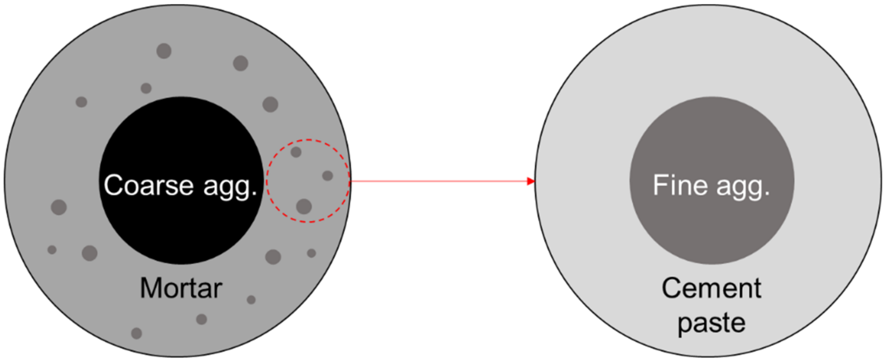

Figure 2-5 Theoretical model for concrete and mortar

2.3 Microstructure of Cement Paste

The internal structure of cement paste at the micrometer level involves various hydration products, such as C-S-H and CH, which are quite different from the mesostructure of concrete at the millimeter level, as described in the previous section. The CH and other crystals in the cement paste are randomly distributed particles. We need a different approach from the GSC model. The Mori-Tanaka model is used for cement paste.

2.3.1 Mori-Tanaka Model

The Mori-Tanaka model (Benveniste 1987; Mori and Tanaka 1973) is a good approach to estimate the effective mechanical properties of a composite material based on its simplified internal structure and the given properties of the constituents. This model can consider a porous media with various morphologies of microstructural components, making it suitable for modeling the effective properties of cement paste.

As shown in Figure 2-6, a heterogeneous composite material can be generalized to an equivalent homogeneous medium (EHM) with different inclusions (phases) within the material. Based on the physical characteristics of each phase, the inclusions can be simplified and categorized into three groups: elliptical inclusions with various orientations (*P1*), spherical inclusions (*P2*), and elliptical inclusions with a known identical orientation (*P3*). All of them are embedded in the matrix phase (*M*). For the constituent phases and the composite material as a whole, these are not one-dimensional problems like the one shown for the GSC model. Therefore, a three-dimensional formulation must be used, in which the three-dimensional stress and strain components are linked together by a stiffness tensor. So, instead of calculating the effective modulus of elasticity (which is for a one-dimensional formulation), the effective stiffness tensor must be obtained. Similar to the GSC model, the effective stiffness tensor can be calculated based on the stiffness tensors of the constituent phases and the volume fractions of the phases. In addition, another tensor will be needed in the formulation to consider the shapes of the phases. The effective stiffness tensor of the composite material can be expressed as (Chen et al. 2014):

$$\boldsymbol{C_{comp}} = \sum_{p=P_1,P_2,P_3,M} f_p \boldsymbol{C_p} : \boldsymbol{A_p} \tag{2-8}$$

where

f_p = volume fraction of phase *p* (unitless),

$\boldsymbol{C_p}$ = fourth order stiffness tensor of phase *p*,

$\boldsymbol{A_p}$ = fourth order strain concentration tensor of phase *p*,

and the double dot product: is defined as $X:Y=X_{ij}Y_{ij}$ with tensor notation.

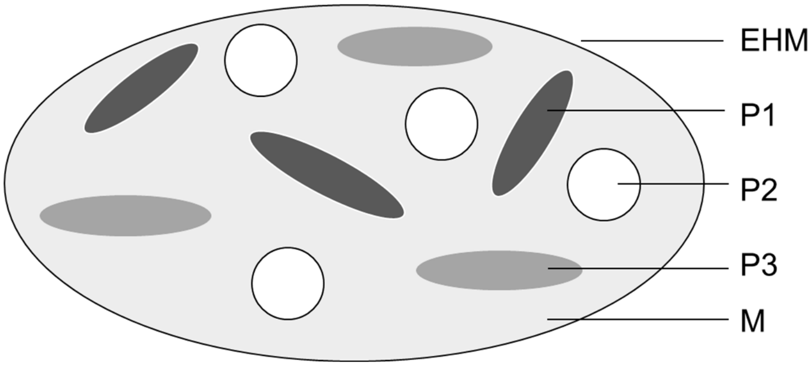

Figure 2-6 Random representation of a composite material

If it can be assumed that each phase is homogenous within its domain, then $\boldsymbol{A_p}$, which is the tensor to consider the shapes of the constituent phases, can be obtained as (Chen et al. 2014):

$$\boldsymbol{A_p} = \left[\boldsymbol{I} + \boldsymbol{S_p} : \left(\boldsymbol{C_M^{-1}} : \boldsymbol{C_p} - \boldsymbol{I}\right)\right]^{-1} : \left\{ \sum_{p=P_1,P_2,P_3} f_p \left[\boldsymbol{I} + \boldsymbol{S_p} : \left(\boldsymbol{C_M^{-1}} : \boldsymbol{C_p} - \boldsymbol{I}\right)\right]^{-1} \right\}^{-1} \tag{2-9}$$

where

$\boldsymbol{I}$ = symmetric fourth order unity tensor and

$\boldsymbol{S_p}$ = fourth order Eshelby tensor of phase p.

The subscript p is the index for inclusions and M is the index for matrix.

The Eshelby tensor $\boldsymbol{S_p}$ considers the response of an ellipsoidal inclusion with shape factor (ratio of the length of the axis of revolution to the length of an axis orthogonal to it) to a homogeneous static strain. For the sake of simplicity, the average Eshelby tensor is used (Damien et al. 2019). The stiffness tensor of the composite material shown in Figure 2-6 is given as:

$$\begin{aligned} \boldsymbol{C_{comp}} = & \left\{ \int_{\theta=0}^{\pi} \int_{\varphi=0}^{2\pi} f_{P_1} \boldsymbol{C_{P_1}} : \left[\boldsymbol{I} + \boldsymbol{S_{P_1}}(\theta,\varphi) : \left(\boldsymbol{C_M^{-1}} : \boldsymbol{C_{P_1}} - \boldsymbol{I}\right)\right]^{-1} \frac{\sin(\theta)}{4\pi} d\theta d\varphi \right. \\ & \left. + \sum_{p=P_2,P_3} f_p \boldsymbol{C_p} : \left[\boldsymbol{I} + \boldsymbol{S_p} : \left(\boldsymbol{C_M^{-1}} : \boldsymbol{C_p} - \boldsymbol{I}\right)\right]^{-1} + f_M \boldsymbol{C_M} \right\} \\ & : \left\{ \int_{\theta=0}^{\pi} \int_{\varphi=0}^{2\pi} f_{P_1} \left[\boldsymbol{I} + \boldsymbol{S_{P_1}}(\theta,\varphi) : \left(\boldsymbol{C_M^{-1}} : \boldsymbol{C_{P_1}} - \boldsymbol{I}\right)\right]^{-1} \frac{\sin(\theta)}{4\pi} d\theta d\varphi \right. \\ & \left. + \sum_{p=P_2,P_3} f_p \left[\boldsymbol{I} + \boldsymbol{S_p} : \left(\boldsymbol{C_M^{-1}} : \boldsymbol{C_p} - \boldsymbol{I}\right)\right]^{-1} + f_M \boldsymbol{I} \right\}^{-1} \end{aligned} \tag{2-10}$$

where

θ, φ = Euler angles which describe the orientation of a rigid body with respect to a fixed coordinate system.

Comparing Figure 2-6 for the Mori-Tanaka model and Figure 2-4 for the GSC model, it is clear that the Mori-Tanaka model is good for those materials with multiple randomly distributed phases with different shapes, while the GSC model is suitable for the internal structures with phase associations. The Mori-Tanaka model is applied to cement paste in the next section, where the specific phases in cement paste are assigned to the inclusions shown in Figure 2-6.

2.3.2 Micro-scale Level Model for Cement Paste

Figure 2-7 shows the microstructure of hardened cement paste. The hardened cement paste can be treated as a multiphase composite in which clinker, calcium hydroxide (CH) and aluminate, and capillary pores are embedded in the calcium silicate hydrate (C-S-H) gel matrix. Vandamme et al. (2010) and Chen et al. (2014) differentiate C-S-H gel into three different phases: low density (LD) C-S-H, high density (HD) C-S-H and ultrahigh density (UHD) C-S-H. The LD C-S-H is considered as the matrix of the cement paste. The UHD C-S-H forms surrounding the clinker. The HD C-S-H locates between them. Therefore, it can be treated as a multiscale problem: the clinker and UHD C-S-H are considered as the sub-inclusion, and this inclusion and HD C-S-H form the equivalent inclusion, as shown in Figure 2-8. Figure 2-8 also shows the theoretical model of hardened cement paste including each component's morphology. According to Stora et al. (2006), the clinker can be modeled as half of an oblate spheroid and half of a prolate spheroid with an aspect ratio of 0.81. The HD and UHD C-S-H are assumed to orient parallel to the clinker, and thus they have the same aspect ratio. The

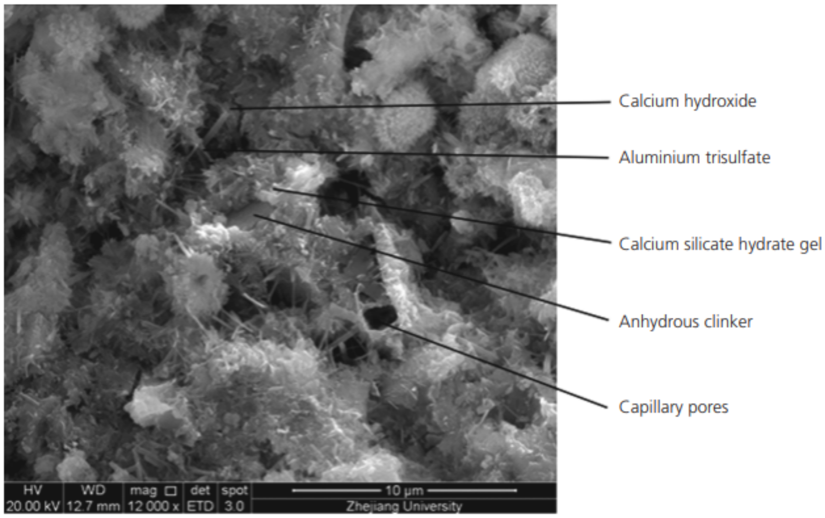

Figure 2-7 Environmental scanning electron microscopy micrograph of a hardened cement paste specimen with a water/cement ratio of 0.35 at age 28 days (Republished with permission of ICE Publishing from Chen et al. 2014, "A nano-model for micromechanics-based elasticity prediction of hardened cement paste." Magazine of Concrete Research, 66(22), 1145–1153; permission conveyed through Copyright Clearance Center, Inc.)

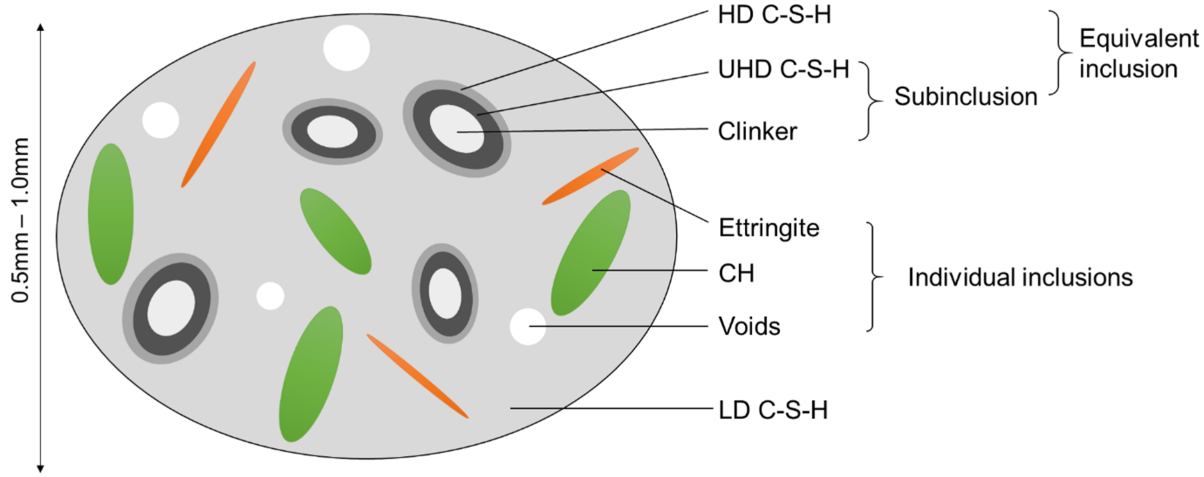

Figure 2-8 Theoretical model representing each inclusion's morphology in cement paste

aluminate, also named as ettringite, has an intrinsic needle-like morphological effect and is considered as a prolate spheroid with an aspect ratio of 0.69. CH is modeled as a prolate spheroid with an aspect ratio of 0.7. The voids are assumed to be spherical.

According to Figure 2-8 and Equation (2-10), the stiffness tensor of the sub-inclusion is

$$\begin{aligned}\boldsymbol{C_{subinc}} = &\left\{\boldsymbol{f_{clin}^{subinc}}\boldsymbol{C_{clin}}:\left[\boldsymbol{I} + \boldsymbol{S_{clin}}:\left(\boldsymbol{C_{UHD\,CSH}^{-1}}:\boldsymbol{C_{clin}} - \boldsymbol{I}\right)\right]^{-1} + \boldsymbol{f_{UHD\,CSH}^{subinc}}\boldsymbol{C_{UHD\,CSH}}\right\} \\ &:\left\{\boldsymbol{f_{clin}^{subinc}}\left[\boldsymbol{I} + \boldsymbol{S_{clin}}:\left(\boldsymbol{C_{UHD\,CSH}^{-1}}:\boldsymbol{C_{clin}} - \boldsymbol{I}\right)\right]^{-1} + \boldsymbol{f_{UHD\,CSH}^{subinc}}\,\boldsymbol{I}\right\}^{-1}\end{aligned} \qquad (2\text{-}11)$$

The stiffness tensor of the equivalent inclusion is

$$\begin{aligned}\boldsymbol{C_{EI}} = &\left\{f_{subinc}^{EI}\boldsymbol{C_{subinc}}:\left[\boldsymbol{I} + \boldsymbol{S_{subinc}}:\left(\boldsymbol{C_{HD\,CSH}^{-1}}:\boldsymbol{C_{subinc}} - \boldsymbol{I}\right)\right]^{-1} + f_{HD\,CSH}^{EI}\boldsymbol{C_{HD\,CSH}}\right\} \\ &:\left\{f_{subinc}^{EI}\left[\boldsymbol{I} + \boldsymbol{S_{subinc}}:\left(\boldsymbol{C_{HD\,CSH}^{-1}}:\boldsymbol{C_{subinc}} - \boldsymbol{I}\right)\right]^{-1} + f_{HD\,CSH}^{EI}\,\boldsymbol{I}\right\}^{-1}\end{aligned} \qquad (2\text{-}5)$$

The stiffness tensor of the hardened cement paste is

$$\begin{aligned}\boldsymbol{C_{cp}} = &\left\{f_{LD}\boldsymbol{C_{LD\,CSH}} + f_{cap}\boldsymbol{C_{cap}}:\left[\boldsymbol{I} + \boldsymbol{S_{cap}^{M}}:\left(\boldsymbol{C_{LD\,CSH}^{-1}}:\boldsymbol{C_{cap}} - \boldsymbol{I}\right)\right]^{-1}\right. \\ &+ f_{EI}\boldsymbol{C_{EI}}:\int_{\theta=0}^{\pi}\int_{\varphi=0}^{2\pi}\left[\boldsymbol{I} + \boldsymbol{S_{EI}^{M}}(\theta,\varphi):\left(\boldsymbol{C_{LD\,CSH}^{-1}}:\boldsymbol{C_{EI}} - \boldsymbol{I}\right)\right]^{-1}\frac{sin(\theta)}{4\pi}d\theta d\varphi \\ &+ f_{AFt}\boldsymbol{C_{AFt}}:\int_{\theta=0}^{\pi}\int_{\varphi=0}^{2\pi}\left[\boldsymbol{I} + \boldsymbol{S_{AFt}^{M}}(\theta,\varphi):\left(\boldsymbol{C_{L\,CSH}^{-1}}:\boldsymbol{C_{AFt}} - I\right)\right]^{-1}\frac{sin(\theta)}{4\pi}d\theta d\varphi \\ &\left.+ f_{CH}\boldsymbol{C_{CH}}:\int_{\theta=0}^{\pi}\int_{\varphi=0}^{2\pi}\left[\boldsymbol{I} + \boldsymbol{S_{CH}^{M}}(\theta,\varphi):\left(\boldsymbol{C_{LD\,CSH}^{-1}}:\boldsymbol{C_{CH}} - \boldsymbol{I}\right)\right]^{-1}\frac{sin(\theta)}{4\pi}d\theta d\varphi\right\}\end{aligned} \qquad (2\text{-}6)$$

$$
\begin{aligned}
&:\left\{f_{LD}\boldsymbol{I} + f_{cap}\left[\boldsymbol{I} + \boldsymbol{S}^{\boldsymbol{M}}_{\boldsymbol{cap}}:\left(\boldsymbol{C}^{-\boldsymbol{1}}_{\boldsymbol{LD}\,\boldsymbol{CSH}}:\boldsymbol{C}_{\boldsymbol{cap}} - \boldsymbol{I}\right)\right]^{-1}\right. \\
&\qquad + \int_{\theta=0}^{\pi}\int_{\varphi=0}^{2\pi} f_{EI}\left[\boldsymbol{I} + \boldsymbol{S}^{\boldsymbol{M}}_{\boldsymbol{EI}}(\theta,\varphi):\left(\boldsymbol{C}^{-\boldsymbol{1}}_{\boldsymbol{LD}\,\boldsymbol{CSH}}:\boldsymbol{C}_{\boldsymbol{EI}} - \boldsymbol{I}\right)\right]^{-1}\frac{sin(\theta)}{4\pi}d\theta d\varphi \\
&\qquad + \int_{\theta=0}^{\pi}\int_{\varphi=0}^{2\pi} f_{AFt}\left[\boldsymbol{I} + \boldsymbol{S}^{\boldsymbol{M}}_{\boldsymbol{AFt}}(\theta,\varphi):\left(C^{-\boldsymbol{1}}_{\boldsymbol{LD}\,\boldsymbol{CSH}}:\boldsymbol{C}_{\boldsymbol{AFt}} - I\right)\right]^{-1}\frac{sin(\theta)}{4\pi}d\theta d\varphi \\
&\qquad \left. + \int_{\theta=0}^{\pi}\int_{\varphi=0}^{2\pi} f_{CH}\left[\boldsymbol{I} + \boldsymbol{S}^{\boldsymbol{M}}_{\boldsymbol{CH}}(\theta,\varphi):\left(\boldsymbol{C}^{-\boldsymbol{1}}_{\boldsymbol{LD}\,\boldsymbol{CSH}}:\boldsymbol{C}_{\boldsymbol{CH}} - \boldsymbol{I}\right)\right]^{-1}\frac{sin(\theta)}{4\pi}d\theta d\varphi\right\}^{-1}
\end{aligned}
$$

2.3.3 The Theoretical Model for Clinker

In order to consider the effects of the cement type and water-cement ratio, clinker can be considered as an individual sub-phase of cement paste. The composition of clinker from Taylor (1997) is shown in Figure 2-9. Instead of considering clinker as an isotropic and homogeneous material, it is more reasonable to treat the clinker as a composite material with four phases. The phases are belite (C_2S), alite (C_3S), tricalcium aluminate (C_3A), and ferrite (C_4AF). Their corresponding chemical formulas are listed in Table 2-1. The C_3S is considered as the matrix of the clinker, while the other three phases are treated as individual spherical inclusions. The theoretical model for the clinker is shown in Figure 2-10 based on the morphology given by Termkhajornkit et al. (2014) and may be described by the Mori-Tanaka model.

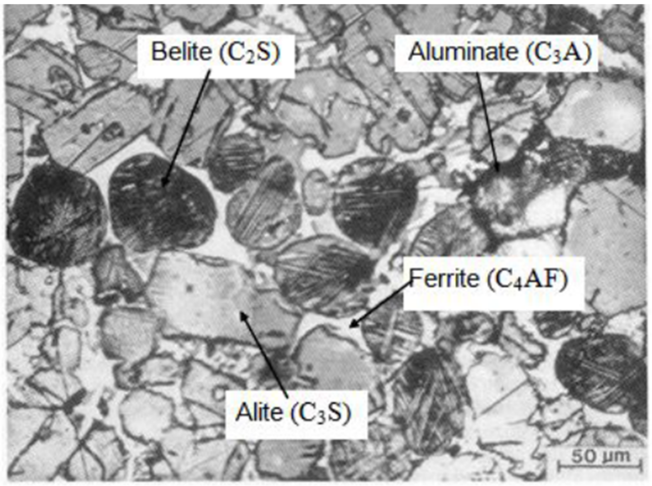

Figure 2-9 Composition of clinker (Republished with permission of ICE Publishing from Taylor, H. F. (1997). *Cement chemistry, 2nd ed.*, Thomas Telford, London; permission conveyed through Copyright Clearance Center, Inc.)

According to Figure 2-10 and Equation (2-10), the stiffness tensor of clinker is

$$\boldsymbol{C_{clin}} = \left\{\sum_{p=C_2S,C_4AF,C_3A} f_p^{clin}\boldsymbol{C_p}:\left[\boldsymbol{I}+\boldsymbol{S_p}:\left(\boldsymbol{C}_{C_3S}^{\boldsymbol{-1}}:\boldsymbol{C_p}-\boldsymbol{I}\right)\right]^{-1}+f_{C_3S}^{clin}\boldsymbol{C}_{C_3S}\right\}$$

$$:\left\{\sum_{p=C_2S,C_4AF,C_3A} f_p^{clin}\left[\boldsymbol{I}+\boldsymbol{S_p}:\left(\boldsymbol{C}_{C_3S}^{\boldsymbol{-1}}:\boldsymbol{C_p}-\boldsymbol{I}\right)\right]^{-1}+f_{C_3S}^{clin}\boldsymbol{I}\right\}^{-1} \tag{2-7}$$

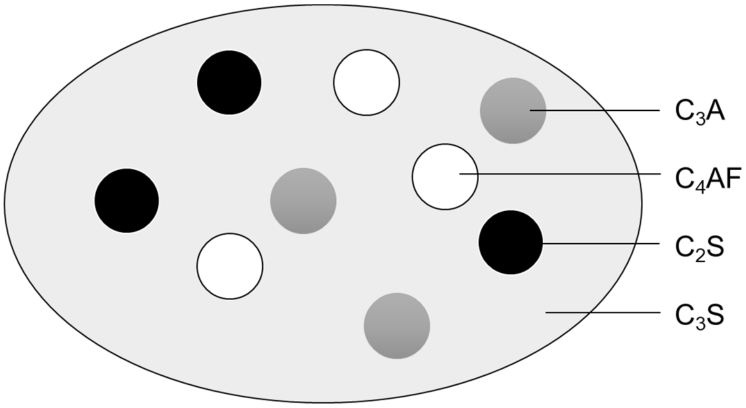

Figure 2-10 Theoretical model for the clinker

Table 2-1 Clinker constituent phases

Constituent phases	Formula	Cement Industry Formula	E (GPa)	μ
Belite	$2CaO+SiO_2$	C_2S	130	0.3
Alite	$3CaO+SiO_2$	C_3S	135	0.3
Tricalcium aluminate	$3CaO+Al_2O_3$	C_3A	145	0.3
Ferrite	$4CaO+Al_2O_3Fe_2O_3$	C_4AF	125	0.3

Sources: Velez et al. 2001; Acker 2004

2.4 Volume Fractions of the Phases in Concrete

As noted, the volume fraction for each constituent phase, especially the hydration products, at each scale level must be obtained in the models. The total volume of the cement paste (V_{cp}) is the volumetric summation of unreacted clinker, hydration products, and capillary pores:

$$V_{cp} = V_{clinker} + V_{CH} + V_{AFm} + V_{AFt} + V_{CSH} + V_{cap} \tag{2-8}$$

where (subscripts):

cp = cement paste,

clinker = unreacted clinker,

CH = CH crystals,

AFm = Hydrated calcium aluminates phases,

AFt = ettringite,

CSH = C-S-H matrix, and
cap = capillary pores.

The volume fractions of each phase can be found in Appendix A.2 .

The degree of hydration of the cement-based material is a time-dependent variable. It should be noted that the service time of nuclear power plants (NPPs) is very long for both biological shielding structures and waste storage facilities (more than 60 years); by that time, the effects of the hydration period of cement are not significant because the hydration reactions are almost completed after 40 years.

At the mortar and concrete levels, the calculation of the volume fractions of the constituent phases is straightforward based on the mix design parameters. At the mortar level, the volume fractions for sand (f_s) and cement paste (f_{cp}) are calculated as

$$f_s = \frac{V_s}{V_s + V_c + V_w} = \frac{W_s/\rho_s}{W_s/\rho_s + W_c/\rho_c + W_w/\rho_w}; f_{cp} = 1 - f_s \tag{2-9}$$

where

V_s, V_c, V_w = volume of sand, cement, and water in concrete, respectively (cm^3),

W_s, W_c, W_w = weight per unit volume of concrete for sand (fine aggregates), cement, and water, respectively (g/cm^3), and

ρ_s = sand density (g/cm^3).

At the concrete level, the volume fractions for gravel (f_g) and mortar (f_m) are calculated as

$$f_g = \frac{V_g}{V_s + V_c + V_w + V_g} = \frac{W_g/\rho_g}{W_s/\rho_s + W_c/\rho_c + W_w/\rho_w + W_g/\rho_g}; f_m = 1 - f_g \tag{2-10}$$

where

V_g = volume of gravel (coarse aggregates) in concrete (cm^3),

W_g = weight per unit volume of concrete for gravel (g/cm^3), and

ρ_g = gravel density (g/cm^3).

2.5 Degradation of Concrete

The effect of neutron irradiation on some types of concrete leads to notable expansion as well as significant degradation of its mechanical properties, such as the compressive strength, the tensile strength, and the modulus of elasticity at neutron fluence levels greater than 1 × 10^{19} n/cm^2. Gamma ray effects are relatively small and are discussed in Chapter 5. The more significant effect of neutron irradiation on concrete is the expansion of the aggregates, which is the primary focus of this section.

2.5.1 Deformation of the Constituent Phases

2.5.1.1 Expansion of Aggregates

Quartz is the dominant crystalline form of SiO_2 which is one of the most abundant minerals in aggregates. Our previous study (Biwer et al. 2020) shows that quartz subjected to fast neutron fluence in excess of 1 × 10^{19} n/cm^2 will significantly expand in volume. Pronounced volume expansion can also be observed for many kinds of aggregates, especially for siliceous aggregates, when fast neutron fluence is greater than 1 × 10^{19} n/cm^2. It has been demonstrated that the crystalline-to-amorphous transition is the main source of irradiation-induced macroscopic expansion of several phases (quartz is one of them) and minerals in aggregates (Weber et al. 1994, 1998). The process is called amorphization or metamictization. Different aggregates expand at different rates under the same level of neutron fluence. Thus, when test data are available for the specific type of aggregate used in a concrete under consideration, the test data can be analyzed by curve fitting, and an equation for the aggregate expansion can be obtained based on the test data and used in the analysis. In the case that no test data are available for the aggregate, one of two options can be considered. One is to obtain test data for a similar aggregate from Biwer et al. (2020) and conduct a curve fitting analysis, and the other option is to use the general equation as shown in the following. Based on a model describing the accumulation of irradiation-induced amorphous fraction of materials (Wang et al. 2000), a general equation for the expansive strain of aggregate ε_a due to neutron irradiation was developed (Jing and Xi 2017).

$$\varepsilon_a = \varepsilon_u \left(1 - \frac{1}{\sqrt{\mathcal{A} + (1-\mathcal{A})\exp(2\mathcal{B}(1-\mathcal{A})N)}}\right) \qquad (2\text{-}11)$$

Where

ε_u = saturation value of dimensional change of aggregate (unitless),

$\mathcal{A}$ = temperature-dependent crystallization efficiency parameter (unitless), varying in the range between 0 and 1,

$\mathcal{B}$ = normalization factor for neutron fluence (cm^2/n), and

N = neutron fluence (n/cm^2).

As shown in this equation, the expansion of aggregates depends mainly on the neutron fluence, N, which is a function of the time and location in an irradiated concrete wall. Basically, the expansion of aggregates at different locations at a fixed time depends on the neutron distribution in the concrete wall, which is discussed and calculated in Chapter 5.

2.5.1.2 Drying Shrinkage of Cement Paste

It was observed that the shrinkage strains of neutron-irradiated cement paste and the control sample subjected to the same thermal cycles are identical (Hilsdorf et al. 1978). Some other test results (Elleuch et al. 1972) of aluminous cement paste up to 280 ºC also supported this observation. To date, there is no strong evidence showing that neutron radiation has a direct impact on the shrinkage of cement paste. As mentioned earlier, neutron irradiation leads to more distortion and damage to the internal structure of aggregates than to the structure of cement paste with a randomly layered internal structure. In general, the shrinkage of cement paste is mainly due to the loss of moisture during the heating process of irradiation and radiolysis. The moisture loss causes volumetric variation in the microstructure of the cement paste, and there is usually no phase transformation involved. As discussed in the literature (Neubauer et al. 1996; Xi and Jennings 1997), the shrinkage of unreacted cement, CH, and other crystals can be considered to be negligible, and the C-S-H shrinkage is responsible for almost all of the drying shrinkage of cement paste.

The effect of drying shrinkage can be taken into account in two different ways. In the case that the shrinkage test data are available, an empirical model can be developed based on the test data, and the empirical model can be used in the analysis. If no shrinkage test data for the concrete are available, a shrinkage model can be used. For example, the present multiphase and multiscale model was originally developed for the shrinkage of concrete (Xi and Jennings 1997), so, the model can be used here for the drying shrinkage of concrete. The control parameter for the shrinkage of concrete is the shrinkage of low density (LD) C-S-H, which can be considered as a function of pore relative humidity.

2.5.1.3 Thermal strains

During the heating process of irradiation, the thermal expansion of concrete (ε_T) can be calculated as

$$\varepsilon_{Ti} = \alpha_i^T \Delta T \tag{2-12}$$

where

α_i^T = coefficient of linear thermal expansion (CTE) for the i^{th} constituent phase in concrete (strain/ ºC), and

ΔT = temperature increment (ºC).

For the calculation of volumetric changes due to temperature variation, the equation for linear thermal strain, Equation 2-19, can be used; that is, the volumetric strain (δ) is the trace of the strain tensor:

$$\delta = \frac{\Delta V}{V} = \varepsilon_{xx} + \varepsilon_{yy} + \varepsilon_{zz} = 3\varepsilon_{eff} \tag{2-20}$$

So, the problem of thermal expansion during neutron irradiation becomes the degradation of the CTE under neutron irradiation. Again, the degradation of the CTE must be considered in conjunction with the two mechanisms: direct neutron irradiation and the heat generated by neutron irradiation.

Consider the direct neutron irradiation first. The results of some experimental studies (Dubrovskii et al. 1966; Hilsdorf et al. 1978) show that the differences between the CTE of neutron-irradiated concrete and that of temperature-exposed concrete are very small, which implies that the direct impact of neutron irradiation is not significant. Another experimental study (Kelly et al. 1969) also demonstrated that neutron radiation has little influence on the CTEs of several types of aggregates. Various aggregates were used in these studies, and the neutron fluence was 2.4×10^{21} n/cm^2 at an average neutron energy of 0.23 MeV. However, the result from another study (Dubrovskii et al. 1967) indicated that the CTE for irradiated concrete started to drop when neutron fluence is higher than 1.2×10^{20} n/cm^2. According to the given energy distribution profile, about 40-50% of the neutrons have an energy higher than 0.1 MeV, so the threshold, in this case, for fast neutron fluence, is in the range of 4.8 to 6.0×10^{19} n/cm^2. The aggregates used were river sand (mainly quartz) and sandstone (80–95% silicon oxide in the form of crystalline quartz). Quartz just begins to expand at this threshold value for this particular case. A similar result can also be found in Kelly et al. (1971): the CTEs of Magnesian Limestone begin to change when their volumes start to increase under fast neutron radiation. These test data imply that the neutron radiation may affect the nature of the thermal expansion of concrete. But available test results are not sufficient to reach a definitive conclusion. In the present model, the coefficient of linear thermal expansion α_i for concrete is assumed to be unaffected by neutron radiation.

Now, consider the effect of temperature rise due to neutron irradiation on the CTE of concrete. Many test results showed that the CTEs of concrete are temperature dependent (Lee et al. 2009). The CTE of cement paste and the CTE of aggregates behave differently under an elevated temperature and must be considered separately.

For cement paste above 120 ºC, phase transformations may be involved, and a stoichiometric model (Lee et al. 2009) may be used to calculate the volume fractions and the CTE as a function of temperature. Since the temperature in the NPP is usually well controlled under 65 ºC, for cement paste and its constituent phases, the values of CTE under 200 ºC may be considered as constants, and they are shown in

Table 2-2.

In conventional concrete material, aggregates normally constitute 65-80% of the total volume of concrete. Therefore, the volumetric behavior of the aggregates is very important for the volume changes of concrete. It has been reported that the CTEs of some types of aggregate increased with temperature above 100 ºC, which is mainly due to their changes in mineralogical composition (Bažant and Kaplan 1996). The CTE of aggregate also depends on whether the minerals are crystalline or amorphous. As mentioned earlier, neutron irradiation causes structural amorphization of crystalline phases, which leads to the macroscopic expansion of the crystalline mineral.

The values and ranges of the CTEs for different groups of aggregates at 20 ºC are available in the literature (Alexander and Mindess 2005). The behavior of the CTEs of aggregates under elevated temperature can be found in available test data (Bažant and Kaplan 1996). It should be noted that there is no consistency among the values and ranges for the CTEs of various types of aggregate. The behavior within a particular rock group can vary considerably, since the chemical compositions of rocks are quite different, even if they share the same name. Compared to the aggregate volumetric expansion caused by neutron radiation, the changes of CTE due to the neutron radiation under nuclear power plant operating conditions is not investigated further in this study.

Table 2-2 Properties of constituent phases in hardened cement paste

	Mechanical			α_i^T (10^{-6} / °C) (Lee 2006)
Parameters	***E*** **(GPa)**	***μ***	**Ref.**	
UHD C-S-H	44.5	0.24	Vandamme and Ulm (2009)	7.222*
HD C-S-H	29.4	0.24	Constandines and Ulm (2004)	7.222*
LD C-S-H	21.7	0.24	Constandines and Ulm (2004)	7.222*
CH	42.0	0.315	Moteiro and Chang (1995)	11.11*
C_3S	135	0.3	Velez et al. (2001); Acker (2004)	2.301
C_2S	130	0.3	Velez et al. (2001); Acker (2004)	2.301
C_3AF	125	0.3	Velez et al. (2001); Acker (2004)	2.301
C_3A	145	0.3	Velez et al. (2001); Acker (2004)	2.301
Ettringite	50	0.34	Zhodi et al. (2002); Speziale et al. (2008)	
Pores	0	0	-	0

* Under 200 ºC.

2.5.2 Degradation of Mechanical Properties

2.5.2.1 Aggregate

There is a significant reduction of the elastic modulus of aggregates by neutron irradiation, as shown in Figure 2-11. The reduction of concrete properties may be mainly due to the reduction of the elastic modulus of the aggregate and damage induced by the volumetric mismatch between the aggregate and cement paste.

2.5.2.2 Hardened Cement Paste

The analysis of the collected test data has shown that neutron and gamma irradiation very likely have a negligible direct effect on the mechanical properties of hardened cement paste compared to their effects on aggregates (Biwer et al. 2020). Based on these test data (Figure 2-12), the modulus of elasticity of hardened cement paste can be assumed to be a constant under neutron irradiation.

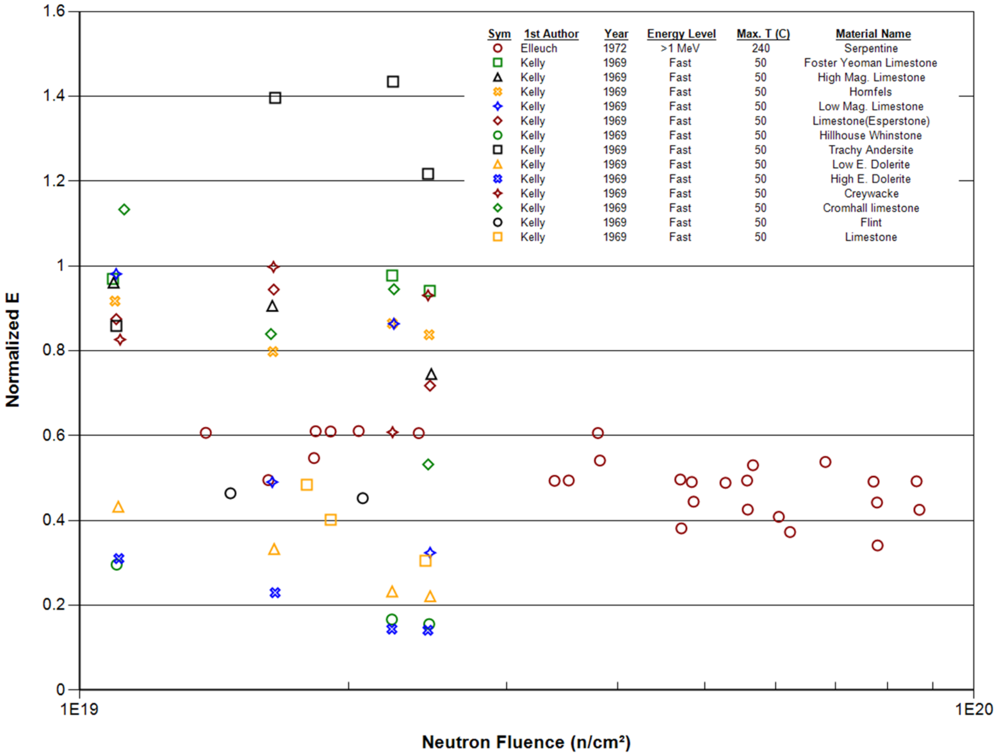

Figure 2-11 Relative elastic modulus of aggregates after neutron irradiation (from Biwer et al. 2020)

It has been confirmed by extensive studies that the elastic modulus of concrete decreases with increasing temperature. Thus, both neutron irradiation and elevated temperature could cause the degradation of the elastic modulus of concrete. The elastic modulus of concrete can be affected in two ways. The first way is that high temperature could cause phase transformations of the constituent phases, which can lead to the deterioration of the concrete because the newly formed phases are usually not as stiff as the original phases. The second way is the incompatibility between the thermal deformation of aggregates and cement paste. Under elevated temperatures, the expansion of aggregates and cement paste do not match with each other, and the volumetric mismatch could cause micro-cracking and debonding at the interface between the aggregate and cement paste. Both of these effects need to be analyzed and taken into account in the model. Similar volumetric mismatch and mismatch of mechanical properties between steel reinforcement and concrete can be observed in reinforced concrete structures, again, under normal operating temperature of nuclear power plants; these mismatches are very small and can be neglected (Willam et al. 2009).

Considering the effect of phase transformation under elevated temperatures first, the degradation of the mechanical properties of concrete has been well studied (Lee et al. 2009), and data on the thermal degradation of concrete up to 800 ºC was obtained. According to the study, there is no phase transformation in cement paste up to 120 ºC. Since the normal operating condition of biological shielding is ≤ 65 ºC, neutron irradiation has little effect on the elastic properties of cement paste. Therefore, the elastic properties of the constituent phases of cement paste, e.g., clinker, C-S-H, and CH, can be considered as constants during normal operating conditions. The values of the elastic properties of the constituent phases are summarized in

Table 2-2.

In addition to the solid phases, the liquid phase, free water, should also be considered. Free water evaporates under radiation heating, the effect of radiolysis and the effect of the liner on internal moisture generation and transfer in concrete are important (test data are not available), which means that the internal pores in cement paste can be considered as unsaturated and drained.

Degradation induced by the volumetric mismatch, including expansion of aggregates, thermal strains, and shrinkage of cement paste at the aggregate-cement paste interface, will be considered in the following section.

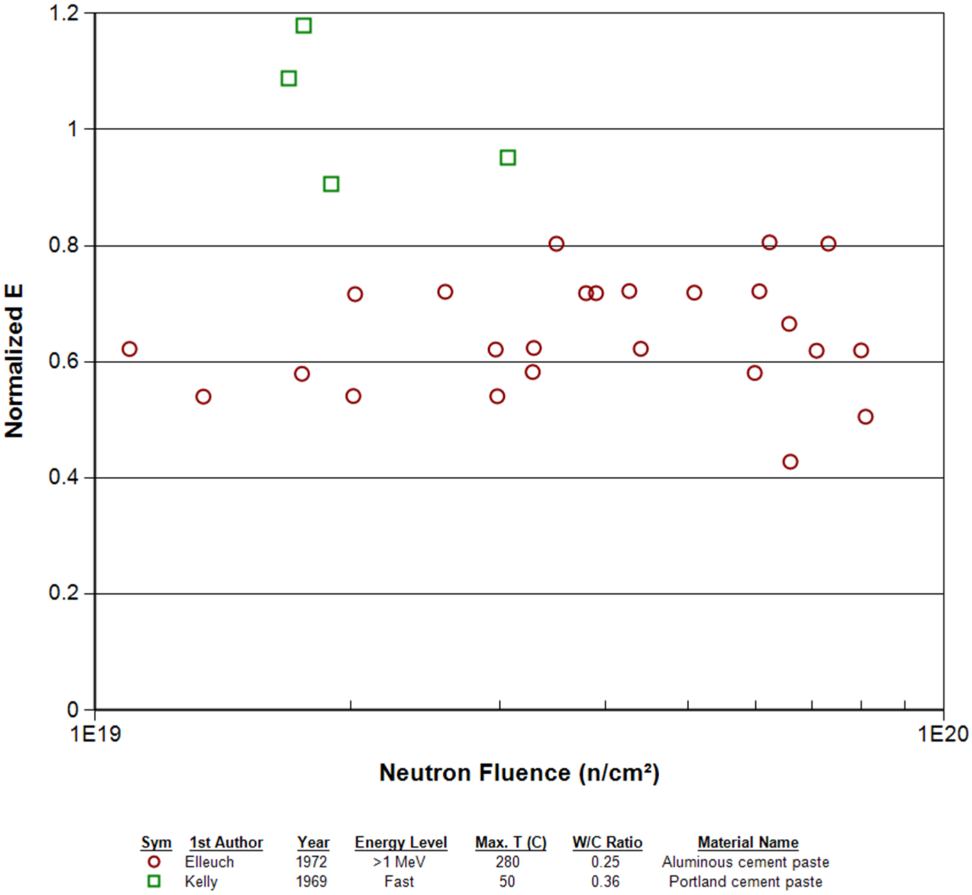

Figure 2-12 Relative elastic modulus of cement paste after neutron irradiation (from Biwer et al. 2020)

2.5.2.3 *Damage Development in Cement Paste*

Due to the expansion of aggregate under neutron irradiation, there is damage in the surrounding cement paste. To evaluate the effect of damage of the cement paste on the overall behavior of concrete, the volume of the damaged part of the hardened cement paste needs to be obtained first. As shown in Equation (2-4), the incompatibility between the deformation of the aggregates and the cement paste will generate an internal pressure *P* at the interface between the two phases. For nuclear irradiated concrete, $\varepsilon_1 - \varepsilon_2$ is a positive value since the aggregate phase expands and the cement paste phase shrinks. As a result, *P* will be a positive pressure applied to the aggregate-cement paste interface. As shown in Figure 2-13 (a), the pressure results in a tensile stress in the cement paste, which may cause damage of the cement paste in the vicinity of the aggregate. In the case of the spherical model for aggregate, the distribution of radial and tangential stresses in the cement paste are

$$\text{Radial stress} \quad \sigma_r = -P\frac{r_s^3}{r^3} \tag{2-21}$$

$$\text{Tangential stress} \quad \sigma_\theta = \sigma_\phi = P\frac{r_s^3}{2r^3} \tag{2-13}$$

where

r_s = aggregate radius (cm).

These two stresses decrease gradually with the cube of *r*.

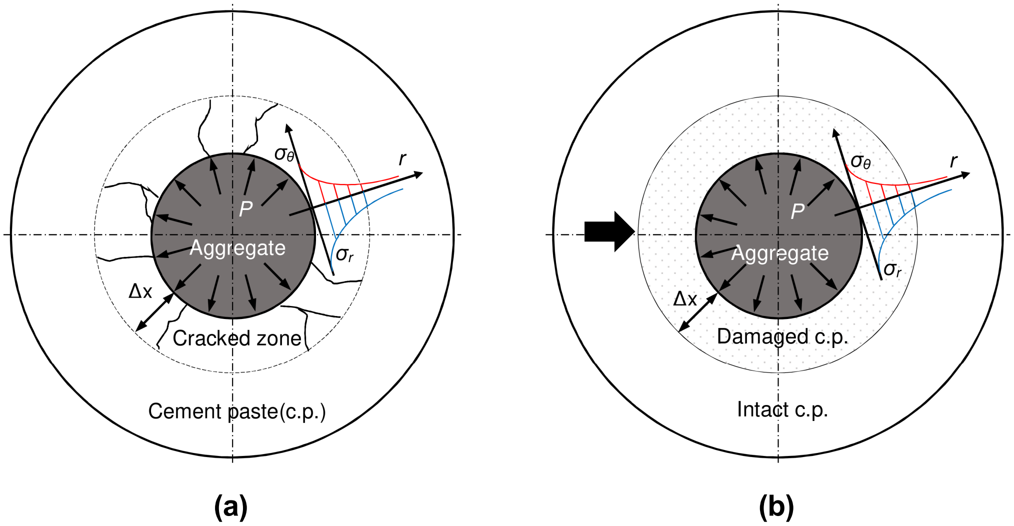

(a) **(b)**

Figure 2-13 (a) The distribution of stresses and potential cracks in cement paste; (b) the cracked zone is replaced by an equivalent medium

In order to take into account the degradation of the cement paste induced by the volumetric mismatch at the aggregate-cement paste interface, the Drucker-Prager plasticity failure criterion is adopted as the criterion for the distressed cement paste. This is a simplified characterization of the damage process at the interface between the aggregate and the surrounding cement paste.

$$\alpha I_1 + \sqrt{J_2} = k \tag{2-14}$$

where

I_1 = first invariant of the stress tensor (MPa),

J_2 = second invariant of the deviatoric stress tensor (MPa^2),

α,k = constants in terms of the tensile strength (f_{ct}) and compressive strength (f_{cc}') of cement paste.

$$\alpha = \left(\frac{1}{\sqrt{3}}\right)(f_{cc}' - f_{ct})/(f_{ct} + f_{cc}')$$

$$k = \left(\frac{2}{\sqrt{3}}\right)(f_{cc}' f_{ct})/(f_{ct} + f_{cc}')$$

When the cement paste in the vicinity of aggregates starts to undergo plastic yielding ($r = r_s$), by substituting Equation (2-21) and Equation (2-13) into Equation (2-14), the critical interface pressure (P_c) for the plastic yielding initiation of cement paste is obtained:

$$P_c = \frac{4 f_{cc}' f_{ct}}{3(f_{ct} + f_{cc}')} \tag{2-15}$$

Once P reaches P_c, the cement paste surrounding the aggregate will undergo plastic yielding, which is considered to be the distressed zone, with a small increase ΔP in P. The damage development process is shown in Figure 2-13 (a) and (b). The thickness of the distressed zone is Δx in the radial direction. In this case, the new interface pressure is $P = P_c + \Delta P$ and the new yield surface of the cement paste is $r = r_s + \Delta x$. Based on Equation (2-14), the ratio between Δx and r_s is

$$\frac{\Delta x}{r_s} = \sqrt[3]{1 + \frac{3\Delta P(f_{ct} + f_{cc}')}{4 f_{cc}' f_{ct}}} - 1 \tag{2-16}$$

Then, a recursive equation describing the radius of yield surface of the cement paste at time t_n can be obtained

$$r_{n+1} = r_n + \Delta x_n = r_n \sqrt[3]{1 + \frac{3\Delta P_n(f_{ct} + f_{cc}')}{4 f_{cc}' f_{ct}}} \tag{2-17}$$

The initial value for r_n is $r_0 = r_s$ when P just reaches P_c. If the pressure is less than P_c at r_{n+1}, there will be no new distressed phase, and the damage initiates as soon as the pressure increases to a level larger than P_c. The details of derivation can be found in Appendix A.4 . The calculation process is explained below.

As shown in Equation (2-4), the interface pressure P is a function of the elastic properties and deformations of the composite phases in the material, which means that $\Delta x/r_s$ is size independent. Therefore, the GSC model can be applied to calculate the stiffness of the distressed materials, providing a proper treatment of damaged cement paste. The theory is called composite damage mechanics (Eskandari-Ghadi et al. 2014; Xi et al. 2006).

In the composite damage theory, we considered a damaged material as a composite material comprised of two different phases. One is the fully damaged phase and the other is the fully intact phase. It should be emphasized that the term composite damage mechanics here refers to the use of composite theory to solve a damage problem, for example, to use the GSC model to deal with damage development in a material, while the material itself could be initially a composite material like concrete. During the damage development process such as due to nuclear irradiation, all phases can be assumed to be linearly elastic and isotropic.

In this case, as shown in Figure 2-13, the damaged zone in cement paste is replaced by a distressed (or damaged) phase with a reduced stiffness. The damaged phase in cement paste has a lower stiffness (E_d) than that of the intact cement paste (E_0) when the damage occurs. Thus, $0 < E_d/E_0 \leq 1$. E_d/E_0 is an important parameter in this theory, and a constant value is usually used for it. This is the ratio of elastic modulus of the fully distressed material and the intact material. The ratio is an input parameter for the analysis. The determination of this parameter is discussed in Section 2.5.3. The overall damage is quantified using the volume fraction of the fully distressed phase.

In the composite damage mechanics, all of the phases can carry loads and have their own non-zero elastic modulus, which is different from conventional scalar damage mechanics where the damaged phase has a zero modulus.

After these treatments, the distressed concrete can be modeled as a multiphase composite material. As one can see in Figure 2-14, the inclusion (black) is the aggregate phase, the first layer (red) is the damaged cement paste, and the second layer (blue) is the intact cement paste. The volume fraction of the damaged phase is the variable which describes the development of internal damage in the material and can be obtained based on Equation (2-17).

During the calculation process, small time steps should be used, which means that the incremental deformation of aggregate should be small enough to ensure the slow variation of the P with respect to time. If the damage criteria are not met, go to the next time step with an increased aggregate expansion until damage is initiated. After that, from previous time t_n to current time t_{n+1}, the inclusion phase in the model should be the combination of the original inclusion and damaged cement paste formed in all of the previous time steps. This new inclusion will have new mechanical properties and strains that can be calculated using the previously developed equations; see Equations (2-5) and (2-6). There will be a new interface with radius r_{n+1}, as shown in Figure 2-15. In the next time step, the calculation of the interface pressure and damage criterion should be performed at the new interface. The calculation flow of the model is shown in Figure 2-1.

2.5.3 Determination of E_d/E_0

It has been observed in a distressed cement paste, the stiffness of a fully distressed cement paste sample is not zero but a reduced value E_d, reduced from its initial value E_0. For example, it can be 20% of E_0 depending on the composition of the cement paste under consideration. The 20% means that the ultimate modulus of elasticity of cement paste at a set or defined state of degradation is 20% of its initial value for intact cement paste, and the corresponding ratio of E_d/E_0 will be 1/5.

To determine the ratio E_d/E_0, first of all, the final state of degradation must be identified. In our case, it is the time when the entire cement paste phase is fully distressed. As shown in the Phase 1 study (Biwer et al. 2020), almost all properties of nuclear irradiated concrete, including strength and modulus of elasticity, reach the lowest values at a fast neutron fluence of 1×10^{20} n/cm^2; the maximum aggregate expansion is also expected to be reached at this neutron fluence value. So, the time for the end state of degradation can be considered to be the time when the internal neutron fluence level reaches 1×10^{20} n/cm^2. It should be pointed out that other fast neutron fluence levels can also be used if test results are available. Then, the modulus of elasticity of fully distressed cement paste can be determined from the present model inversely based on the original properties of cement paste, aggregate, and concrete as well as the results of the modulus of elasticity of nuclear irradiated concrete and aggregate at this radiation level (1 × 10^{20} n/cm^2).

A numerical example on how to determine the modulus ratio E_d/E_0 of cement paste is provided here. The mix proportion by weight of ordinary concrete samples is water/cement/aggregate = 0.5/1/4.9. The original elastic modulus and Poisson's ratio of the aggregate were assumed to be 49.6 GPa and 0.28, respectively. The elastic properties of the original hardened cement paste were assumed as (Young's modulus and Poisson's ratio): E_0 = 19.2 GPa and ν_0=0.27.

In this example, we consider the neutron level at the end state of degradation to be 1 × 10^{20} n/cm^2, as shown in the Phase 1 study (Biwer et al. 2020). When 1 × 10^{20} n/cm^2 of fast neutron fluence is reached, the elastic modulus of aggregate is assumed to be 40% of the original value, and the elastic modulus of concrete is assumed to be 29% of the original value. If we assume the Poisson's ratios do not change, the elastic modulus of distressed cement paste can be obtained by using the present model inversely: E_d = 3.648 GPa, which is about 19% of the original value. Therefore, $E_d/E_0 = 0.19$.

This parameter depends on the composition of the cement paste, which is determined by the cement type and concrete mix design parameters. It allows the user to control the acceptable level of damage at the set end state of degradation of the concrete and can be determined based on available test data of concrete using the inverse method shown in the example. In this example, a neutron fluence level of 1 × 10^{20} n/cm^2, and the corresponding values for concrete, are assumed. Other neutron fluence levels and concrete properties can also be used in the inverse calculations if test data are available.

2.6 Input Parameters

All input parameters needed for the composite mechanics model of concrete developed in this chapter are listed in

Table 2-3.

2.7 Model Validation

In order to validate the multiscale and multiphase model, the post-irradiation residual properties of one specific concrete called Con-A, Test ID PPT-D tested by the Japanese team at the Kjeller JEEP-II reactor (Maruyama et al. 2017) under a fast neutron fluence from 7.09×10^{18} to 4.78×10^{19} n/cm^2 (E > 0.1 MeV), was analyzed.

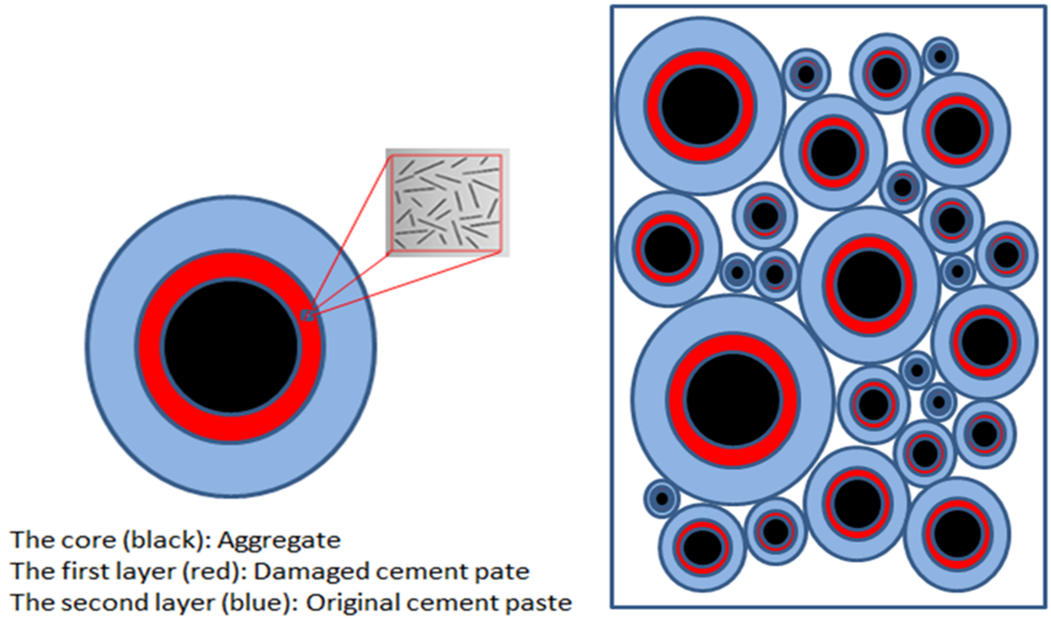

Figure 2-14 Composite damage mechanics

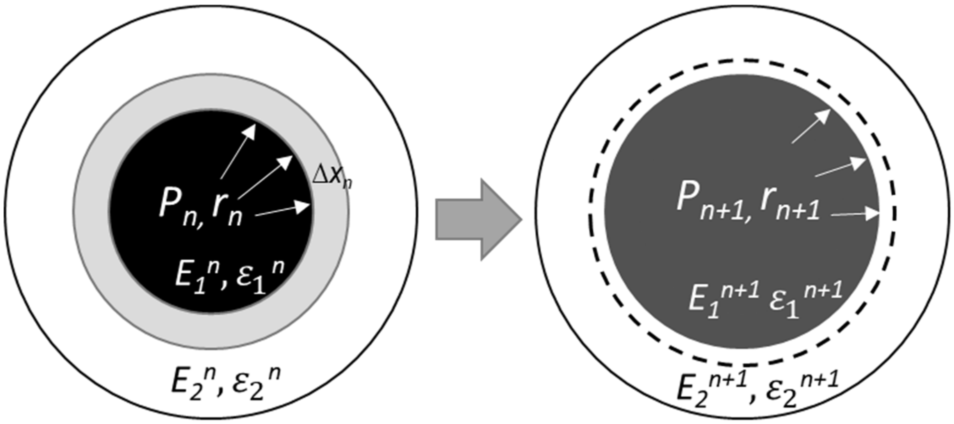

Figure 2-15 Calculation process from t_n to t_{n+1}

Table 2-3 Input parameters for the composite mechanics model of irradiated concrete

Environment information	Concrete material	
	Cement	Aggregate (fine and coarse aggregate)
• Neutron flux (*N*) • Temperature (*T*) • Relative Humidity (R.H.)	• Cement type (chemical composition) • Water-cement ratio (w/c) • Density (ρ) • Compressive strength of hardened cement paste (f_{cc}') • Tensile strength of hardened cement paste (f_{ct}) • E_d/E_0 • Curing time, *t* • Others (see Table 2-1 and • Table 2-2)	• Aggregate fractions in the concrete (s, g) • Aggregate type • Density (ρ) • Elastic modulus (E) • Poisson's ratio (ν) • CTE (α^T) • Expansion of aggregate under neutron radiation • Degradation of elastic modulus under neutron radiation

Aggregate expansion profiles are shown in Figure 2-16. GA is for coarse aggregate and GB is for fine aggregate. Other symbols (GC, GD, GE, and GF) refer to other types of aggregates and will not be used here. The properties used are listed in

Table 2-2 and Table 2-4. The chemical compositions of the cement are shown in Table 2-5. The water-cement ratio is 0.5 and the mix design is shown in Table 2-6. The curing time is 1 year before the test. The temperatures during the test are in the range of 62.0-71.9 °C; and the highest temperature experienced by concrete (71.9°C) is used in the analysis. The strengths of cement paste are f_{cc}' = 65 MPa and f_{ct} = 3.5 MPa. It was assumed that the degradation of the Young's modulus of the aggregate is the same as the linear regression of the serpentine data collected by Elleuch et al. (1972), as shown in Figure 2-17. E_d/E_0 = 0.19 is used.

Table 2-4 Material properties

Material	*P* (g/cm^3)	*E* (GPa)	*μ*	α_i^T (10^{-6} / ºC)
Aggregate GA crushed altered tuff	2.66	65	0.28	9
High early-strength ordinary Portland cement	3.14	-	-	-
Sand (land sand)	2.61	35*	0.25*	9*
Concrete		36.352		-

* Assumed typical values.

Table 2-5 Cement chemical composition

Density	Chemical composition(mass%)												Total
(g/cm^3)	Ig. loss	SiO_2	Al_2O_3	Fe_2O_3	CaO	MgO	SiO_3	Na_2O	K_2O	TiO_2	P_2O_5	MnO	
3.14	1.04	20.78	4.98	2.46	65.4	1.24	3.04	0.21	0.28	0.29	0.32	0.09	100.11

Table 2-6 Mix design (kg/m^3)

Cement	Water	Sand	Aggregate
366	183	799	995

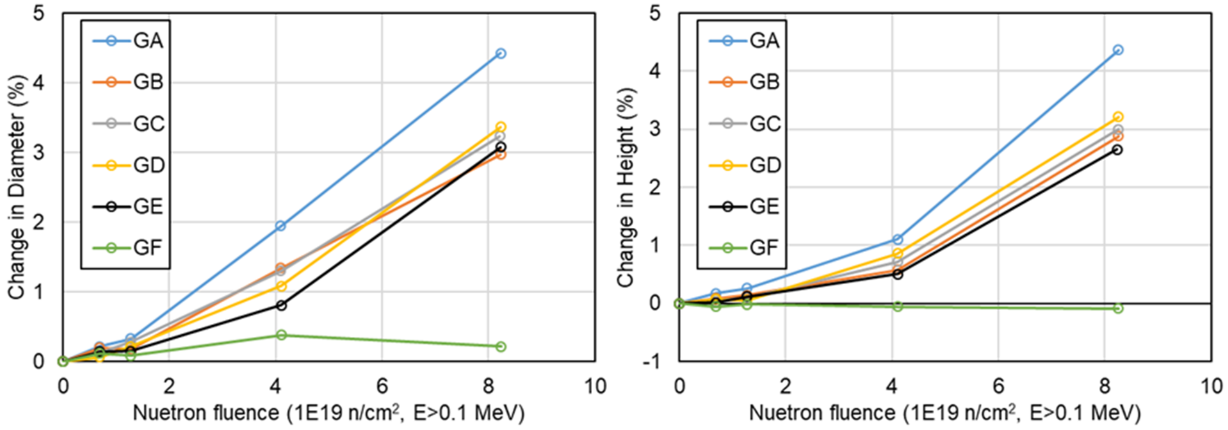

(a) (b)

Figure 2-16 Dimensional changes of aggregates: (a) diameter change; (b) height change (data from Maruyama et al. 2017)

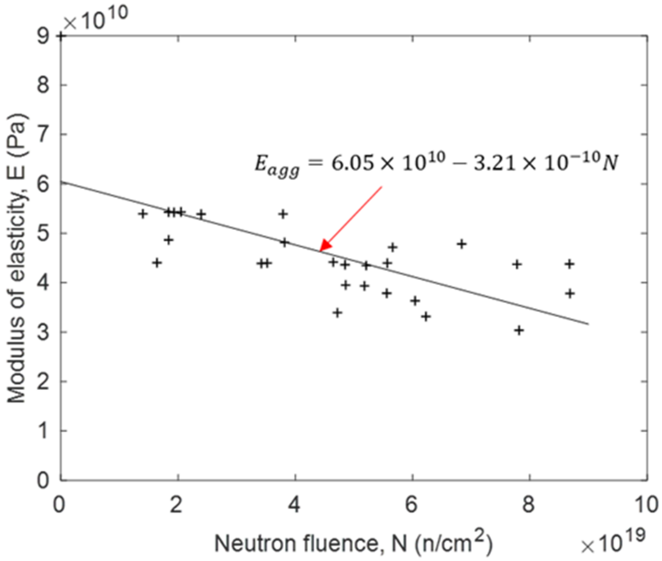

Figure 2-17 The serpentine data collected by Elleuch et al. (1972)

Predictions of the dimensional change and the variation of Young's modulus by the present multiscale and multiphase model agree well with the experimental data (Maruyama et al. 2017), as shown in Figure 2-18 and Figure 2-19. In the calculation, the time step increment should be small enough to achieve a slow damage development with time. For this particular problem, 10000 time steps were used. Since the total irradiation time for this accelerated test is 299.36 days, the time step increment is 0.03 day.

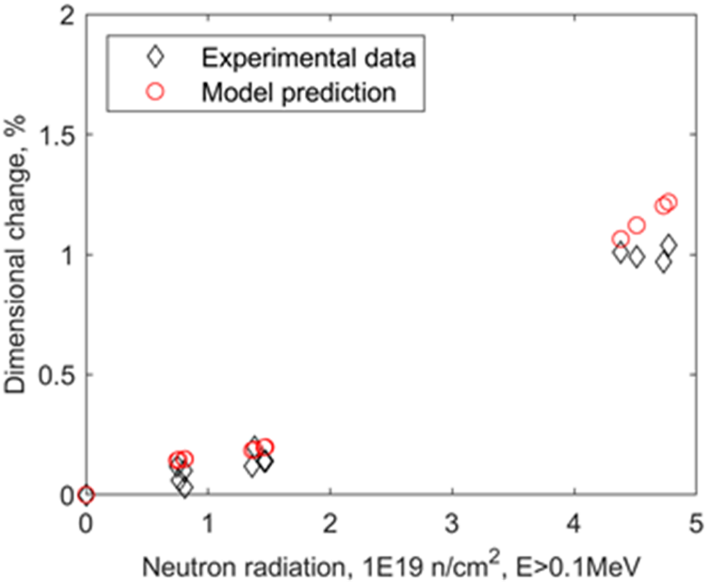

Figure 2-18 Dimensional change of concrete as a function of the neutron fluence for validation

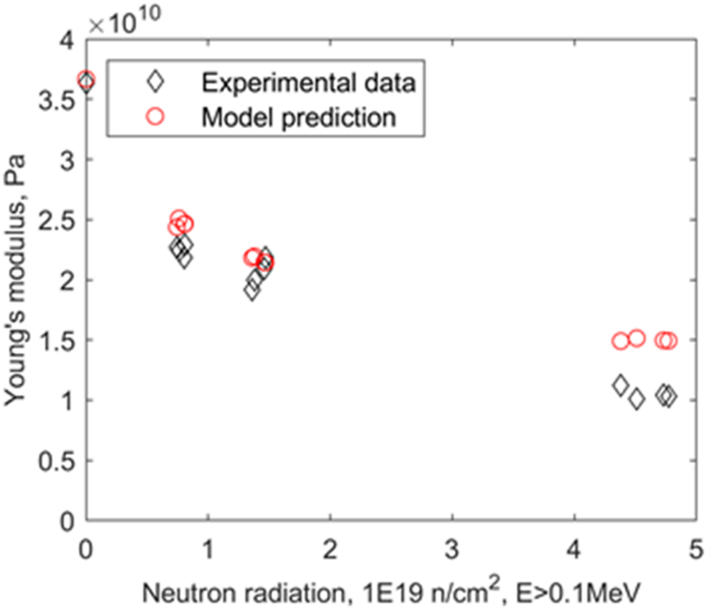

Figure 2-19 Elastic modulus of concrete as a function of the neutron fluence for validation

2.8 Parametric Analyses of the Model

A case study was developed to show the capability of the model and to analyze the effects of the model input parameters on the damage development of the cement paste, the dimensional change, and the elastic modulus of nuclear irradiated concrete. The cement paste damage is quantified using the volume fraction of the fully distressed cement paste in the whole cement paste (V_{cp}^{dis}/V_{cp}).

Concrete samples assumed to be made of ordinary Portland cement concrete and crushed gravel without rebar embedment exposed to a fast neutron fluence of up to 1×10^{20} n/cm^2 ($E > 0.1$ MeV) were analyzed. Different material parameters were used, including three different water-cement ratios: 0.3, 0.4, 0.55; three different aggregate volume fractions: 0.6, 0.7, 0.8; and two different aggregate expansion profiles, as shown in Figure 2-20. Profiles 1 and Profile 2 are nonlinear relationships between the volume change of the aggregate as a function of neutron intensity as described by Equation (2-11). For isotropic expansion of concrete under neutron irradiation, the volumetric expansive strain will be three times the linear strain. The two profiles are based on the test data of aggregate GA and GE in Figure 2-16. These two profiles are the upper bound and lower bound of the data shown in Figure 2-16 (aggregate GF is excluded since it shows no expansion at all). They are used here for the parametric analysis of the model. For actual analysis, the value should be selected based on the aggregate used in the concrete. A linear regression of the serpentine data shown in Figure 2-17 was used as the degradation trend of the Young's modulus for the aggregate under neutron radiation. The strengths of the hardened cement paste were $f_{cc}{}' = 65$ MPa and $f_{ct} = 4$ MPa. The temperature was 65 ºC. The drying shrinkage of cement paste was assumed to be -0.05%. The curing time was one year. All parameters are listed in

Table 2-7. The selection of the input parameters was to cover the potential variation in the parameter values.

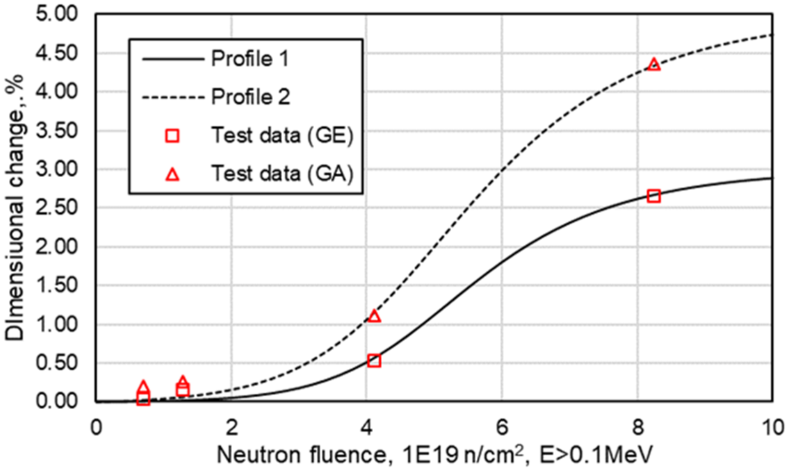

Figure 2-20 Dimensional change of aggregates used in the case study. Profile 1: test data of aggregate GE in Figure 2-16 which can be described by Equation (2-11) with $\varepsilon_u = 3\%$, $\mathcal{A} = 0.9966$, $\mathcal{B} = 1.8 \times 10^{-17}$. Profile 2: test data of aggregate GA in Figure 2-16 which can be described by Equation (2-11) with $\varepsilon_u = 5\%$, $\mathcal{A} = 0.9911$, $\mathcal{B} = 5.96 \times 10^{-18}$.

Table 2-7 Input parameters

Parameters	Values
Fast neutron fluence, N	0~1E20 n/cm^2 (E > 0.1MeV)
Water cement ratio, w/c	0.3, 0.4, 0.55
Aggregate volume fraction, f_g	0.6, 0.7, 0.8
Aggregate expansion profile	Figure 2-20
Cement chemical composition	C=0.654, S=0.2078, A=0.0498,F=0.0246 (mass%)
Cement density, ρ_c	3.14 g/cm^3
Elastic modulus of aggregate, E_{agg}	50 GPa
Poisson's ratio of aggregate, υ_{agg}	0.28
CTE of aggregate, α_{agg}^T	9E-6 / ºC
Aggregate density, ρ_{agg}	2.66 g/cm^3
E_d/E_0	1/3
Strength of cement paste	f_{cc}' = 65 Mpa, f_{ct} = 4 Mpa
The temperature, T	65 ºC
Drying shrinkage	-0.05%
Curing time, t	1 year
Cement paste	Table 2-1 and Table 2-2

Note: For cement chemical composition, C=CaO, S=SiO_2, A=Al_2O_3, F=Fe_2O_3. The mass% are listed in Table 2-5.

2.8.1 Water-Cement Ratio

For this portion of the analysis, only the water-cement ratio was changed among the three specimens considered; all of the other input parameters were kept constant (aggregate fraction = 0.7, E_d/E_0 = 1/3, and aggregate expansion follows Profile 1 in Figure 2-20). As one can see in Figure 2-21, a higher water-cement ratio (w/c) results in less damage induced by nuclear radiation in the cement paste. A higher w/c ratio results in a less densified concrete framework which can accommodate more volume expansion at the aggregate-cement paste interface. This result also explains why the expansion of concrete decreases with the increase of the w/c, as shown in Figure 2-23. As shown in Figure 2-22, the w/c has different effects on the elastic modulus of concrete at different ranges. When the neutron fluence is small, the damage in the cement paste is not severe, as shown in Figure 2-21, and a higher w/c ratio will reduce the damage in the cement paste. Thus, the reduction of elastic modulus of concrete due to nuclear irradiation will be smaller for the concrete specimen with a higher w/c. When the neutron fluence is large, the damage to the cement paste is already significant, and the differences among the three cases became small compared to the absolute value, as shown in Figure 2-21. On the other hand, a higher w/c ratio will reduce the stiffness of the cement paste, and thus, the reduction of the elastic modulus of concrete due to large neutron fluence will be larger for the concrete specimen with a higher w/c, as shown in Figure 2-21.

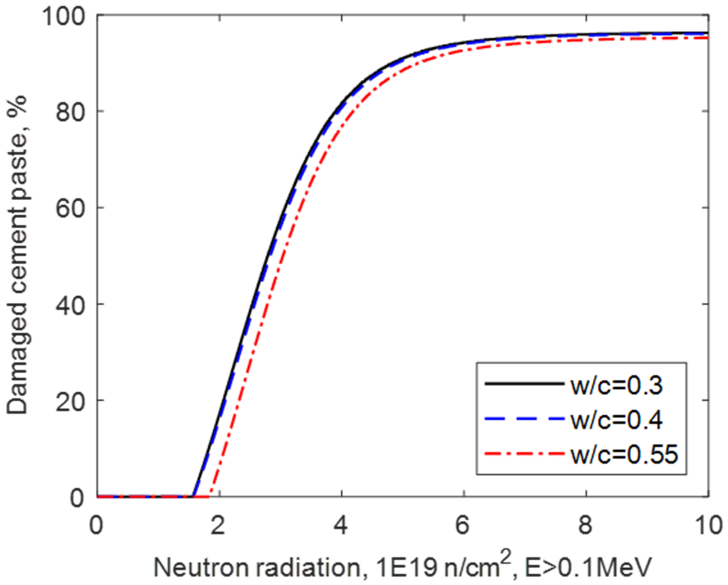

Figure 2-21 **Effect of the w/c on the damage in the cement paste as a function of neutron fluence**

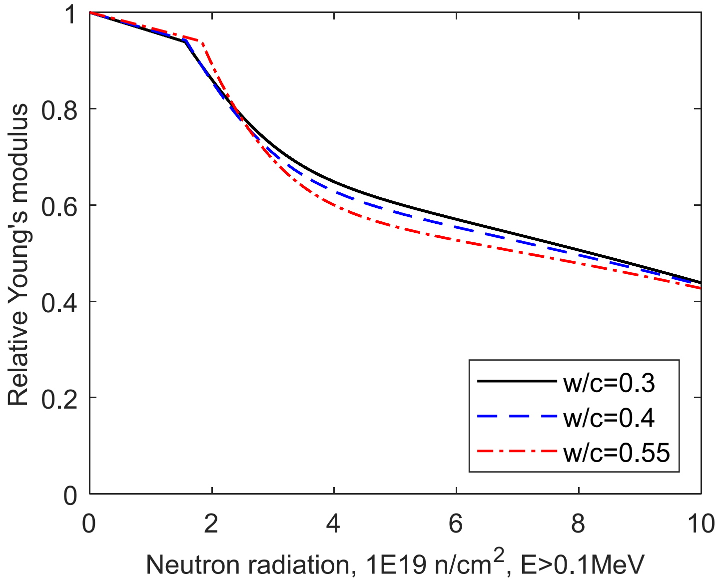

Figure 2-22 **Effect of the w/c on the elastic modulus of concrete as a function of the neutron fluence**

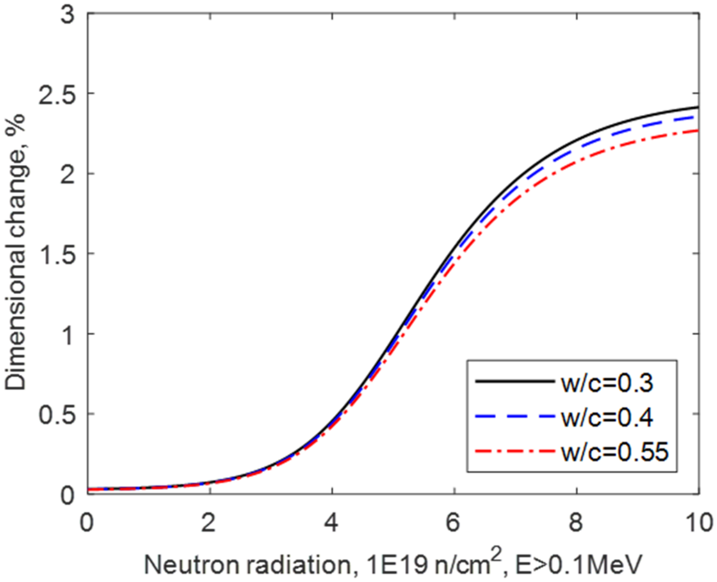

Figure 2-23 Effect of the w/c on the dimensional change of concrete as a function of the neutron fluence

2.8.2 Aggregate Fraction

In this series of calculations, only the aggregate fraction was changed among the three specimens considered; all of the other input parameters were kept constant (water-cement ratio = 0.4, E_d/E_0 = 1/3, and aggregate expansion follows Profile 1 in Figure 2-20). As one can see in Figure 2-24, a higher aggregate fraction slightly reduces the percent of damaged cement paste. This result is because the interface pressure decreases with increasing aggregate fraction (see Equation (2-4)). With a higher volume fraction of aggregate, the confinement of surrounding cement paste is reduced, and thus, the interface pressure is lower. The elastic modulus of concrete under neutron radiation shows a smaller reduction with the increase in the aggregate fraction, as shown in Figure 2-25. This difference is due to the fact that the modulus of elasticity of aggregate is higher than that of cement paste – see the input value in Table 2-7 – so with more aggregate, the relative modulus of concrete is higher. Of course, with an increasing neutron fluence level, the relative values of effective modulus decrease for all three cases. Since the expansion of concrete is mainly due to the expansion of aggregates, the overall expansion of concrete increases with the increase of aggregate fraction, as shown in Figure 2-26.

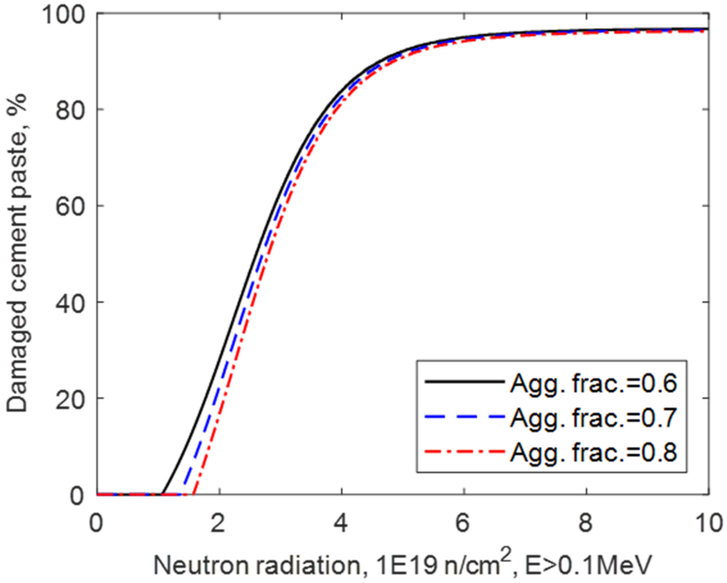

Figure 2-24 **Influence of aggregate fraction on cement paste damage as a function of the neutron fluence**

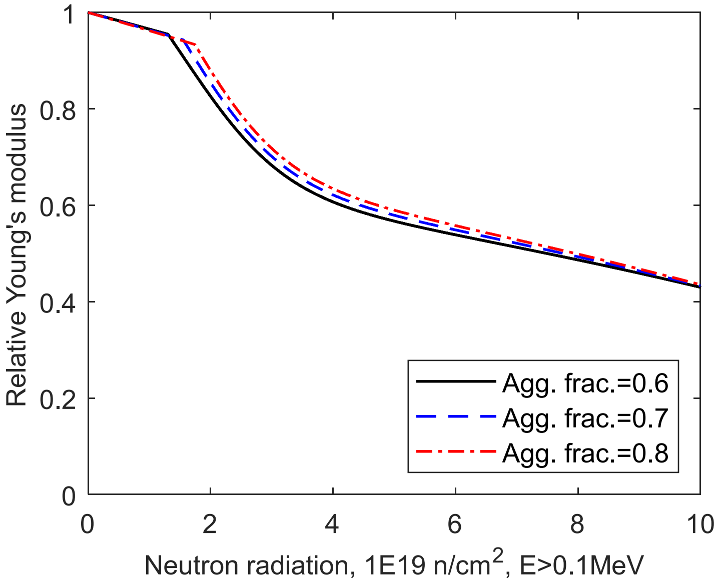

Figure 2-25 **Influence of aggregate fraction on the elastic modulus of concrete as a function of the neutron fluence**

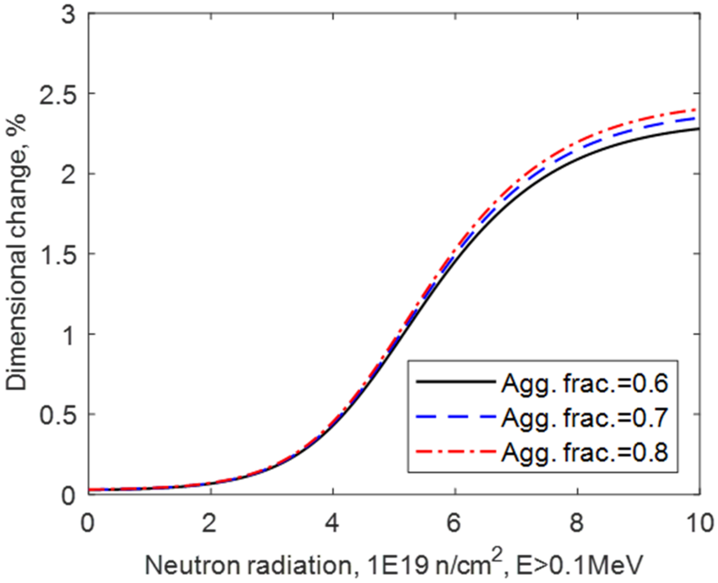

Figure 2-26 Influence of the aggregate fraction on the dimensional change of concrete as a function of the neutron fluence

2.8.3 The Effects of Aggregate Expansion

In this series of calculations, only the aggregate expansion was changed among the three specimens considered; all of the other input parameters were kept constant (water-cement ratio = 0.4, aggregate fraction = 0.7, and $E_d/E_0 = 1/3$). As shown in Figure 2-27, the aggregate expansion profile has a significant impact on the damage development in the hardened cement paste. When the aggregate expansion is slower and smaller (Profile 1), the damage development in the cement paste is also slower and smaller. The final damage factor is affected by the ultimate value of the aggregate dimensional change (the expansion due to nuclear irradiation). When the ultimate dimensional change is smaller, the final damage factor is smaller as well. Reduction of the elastic modulus of concrete is also affected by the aggregate expansion profile. When the aggregate expansion is slower, the degradation of the elastic modulus of concrete is also slower. Figure 2-28 shows that the overall expansion of concrete mainly results from the expansion of aggregates. The results further confirm that the degradation of concrete is mainly due to the aggregate expansion, as one can see in Figure 2-29.

2.8.4 Combined Effects

It should be pointed out that the effects of all influential parameters are mingled together and difficult to distinguish in practice. Section 2.8 is aimed at examining the effect of each one of the influential parameters using the multiscale and multiphase model. It is shown that aggregate expansion is important for degradation of concrete under nuclear irradiation as are the other parameters analyzed in this section. For example, with an aggregate that exhibits large expansion under neutron irradiation, the overall damage to the concrete is expected to be high, if we only consider the expansion of the aggregate. However, the overall damage might not be very high, if the stiffness of the surrounding cement paste is not high. Using an extreme case as an explanation, when the aggregate is surrounded by a “soft” cement paste (like sponge), even a very large aggregate expansion cannot generate significant damage in the cement paste. The stiffness of the cement paste (i.e., the modulus of elasticity of cement paste) depends on the water-cement ratio, so the water-cement ratio is an important parameter. Moreover, with the same expansive aggregate, when there are only a few pieces of them in the concrete, the expansion of the aggregate can be absorbed by the surrounding cement paste without significant damage. That is why the volume fraction of aggregate is an important parameter.

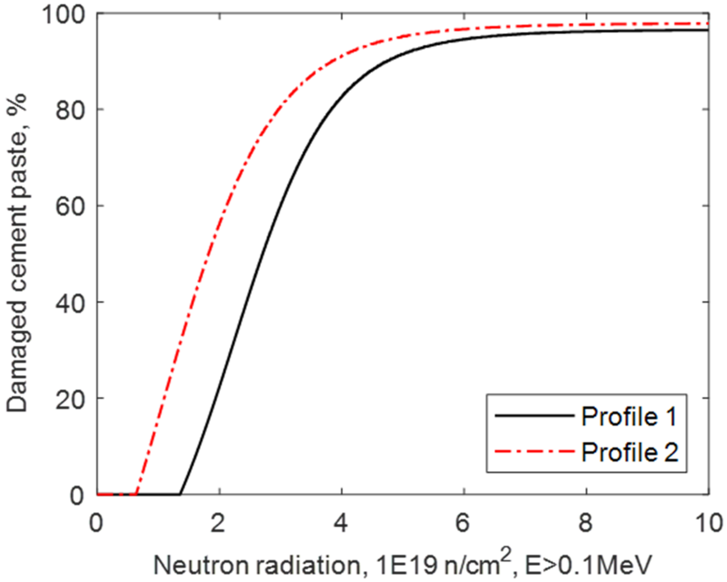

Figure 2-27 **Influence of aggregate expansion on the damage in the cement paste as a function of the neutron fluence**

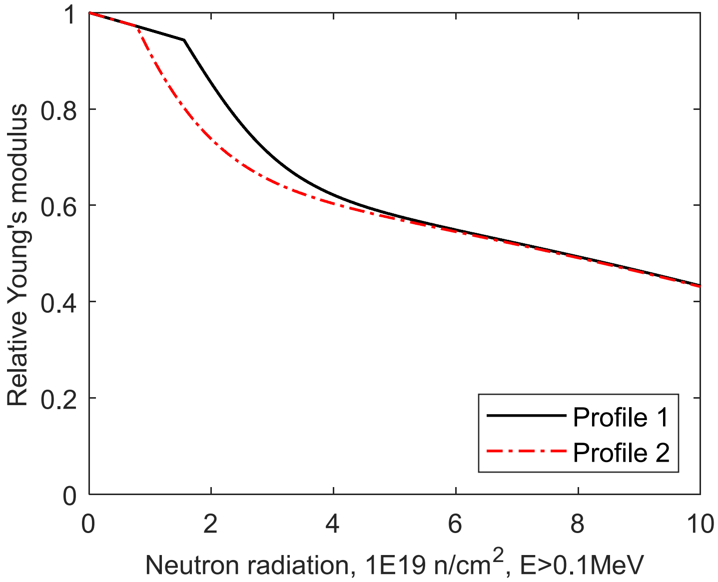

Figure 2-28 **Influence of aggregate expansion on the elastic modulus of concrete as a function of the neutron fluence**

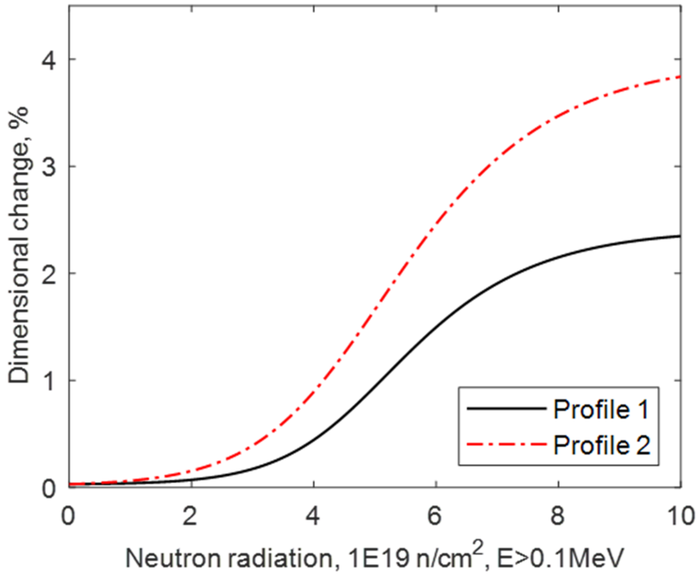

Figure 2-29 **Influence of aggregate expansion on the dimensional change of concrete as a function of the neutron fluence**

2.9 Summary

A multiscale and multiphase material model was developed based on two composite material models: the Mori-Tanaka model and the GSC model. The theories and equations of these two models were introduced first with the equations that are used to calculate the overall stiffness/elastic modulus and strain of a composite material based on the properties and behavior of the constituent phases. The heterogeneous internal structure of concrete was considered at four different scale levels with different constituent phases using either the Mori-Tanaka model or the GSC model. The developed multiscale and multiphase model can be applied to various concrete materials with different mix designs used in different nuclear power plants to estimate the reduction of the modulus of elasticity, deformation, and damage of the concrete. The damage of concrete due to nuclear irradiation was estimated using a composite damage mechanics approach based on a certain failure criterion (the Drucker-Prager plasticity is used in the present study as an example). The established multiscale and multiphase model was validated using a set of experimental data under fast neutron radiation on concrete. Parametric analyses of the model input parameters, including the water-cement ratio, aggregate fraction, and aggregate expansion, were performed to analyze the effects of the parameters on the degradation and deformation of concrete under nuclear irradiation.

3 CREEP OF NUCLEAR IRRADIATED CONCRETE

For concrete material under long-term nuclear irradiation, damage and creep occur concurrently. As discussed in Biwer et al. (2020), the effect of nuclear irradiation on the creep of concrete has not yet been studied sufficiently. Since a numerical model for coupled damage-creep of concrete under nuclear irradiation is not available, a coupled damage-creep model of nuclear irradiated concrete is developed here based on the generalized Maxwell model and Mazars' damage model, and implemented in ABAQUS CAE via a subroutine UMAT. The overall scheme is shown in Figure 3-1. The purpose of using ABAQUS/standard here is to consider the effect of mechanical loading on bioshield walls. The effect of neutron irradiation is considered by the multiphase and multiscale model from Chapter 2, which will be used here as input. In each time step, the results of nuclear irradiation obtained by the multiphase and multiscale model will feed the coupled damage and creep analysis in ABAQUS as inputs (UMAT Maxwell for Creep and Mazar's damage model). This implementation results in the coupling analysis as a one-way process – the effect of nuclear irradiation has an impact on the creep analysis, but the creep has no effect on nuclear irradiation. It also should be pointed out that the damage due to mechanical loading calculated in ABAQUS will not be considered in the neutron transport analysis in Chapter 4 (in which the damage due to neutron irradiation is considered). The neutron transport analysis shown in Chapter 4 will only consider the effects of damage obtained from the multiphase and multiscale model (in Chapter 2) on the transport properties.

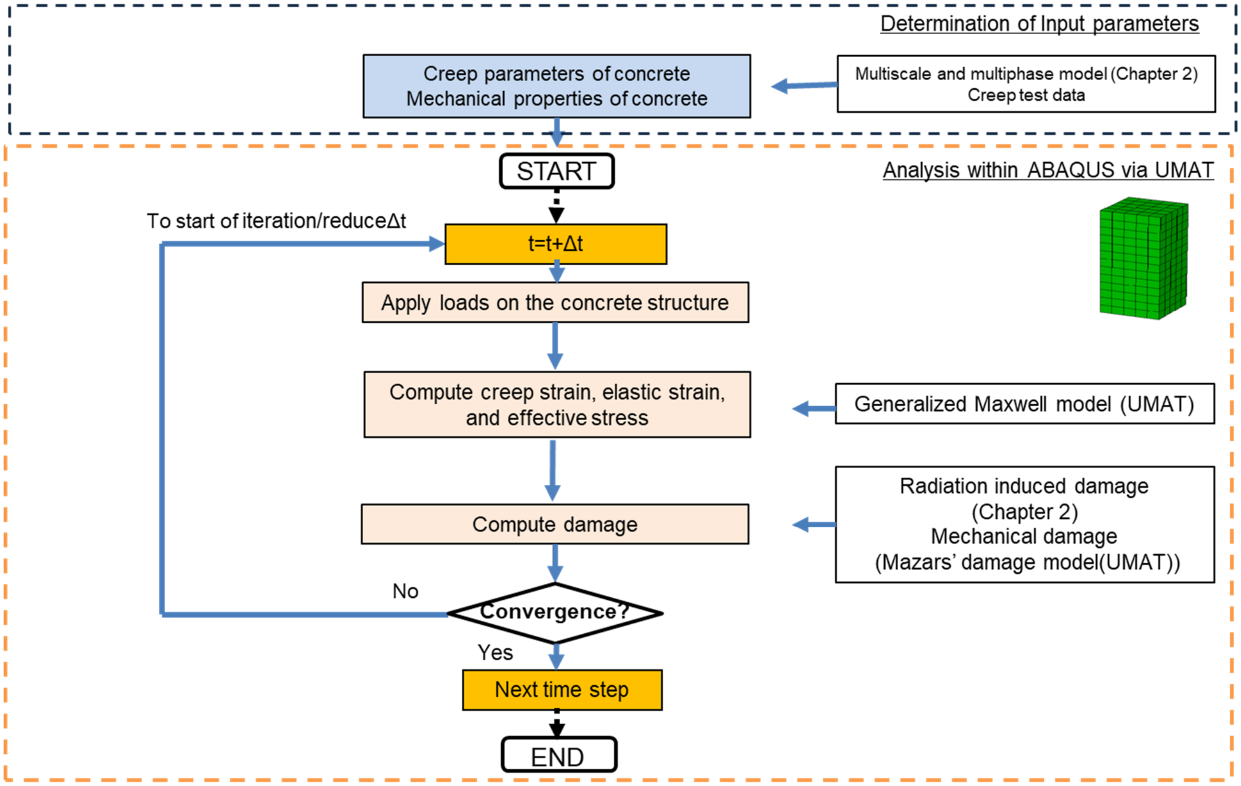

Figure 3-1 Calculation flow chart for coupled damage-creep modeling

3.1 Generalized Maxwell Model

The elastic creep of concrete is defined as the long-term strain of concrete under a constant stress in the elastic range. Specifically, the elastic creep considered in this study is the basic creep, which is the long-term strain of concrete under a constant stress in the elastic range without temperature variation and moisture fluctuation.

The creep of concrete is a function of time *t*. Using Hooke's law, strain $\varepsilon = \sigma/E$, where σ is the applied stress and *E* is the modulus of elasticity. Because σ is a constant and ε is a time-dependent variable, *E* must be a function of time, which is different from the regular elastic stress-strain analysis in which *E* is a constant in the elastic range. For concrete, an important feature of its creep is that the creep depends not only on time but also on the age of concrete when a load is applied at *t′*. In general, the creep is larger when *t′* is smaller, which means that the creep is larger when the load is applied at a younger age of concrete. Therefore, the modulus of elasticity of concrete considering creep is a function of both *t* and *t′*, and it is called the relaxation modulus of elasticity, $Y(t, t')$.

The relaxation modulus of concrete can be characterized by various models. One of them is the generalized Maxwell model, which can be used in general for the creep of various viscoelastic materials. The generalized Maxwell model can be represented by *n* parallel elements of serially coupled springs and dashpots plus a spring as shown in Figure 3-2.

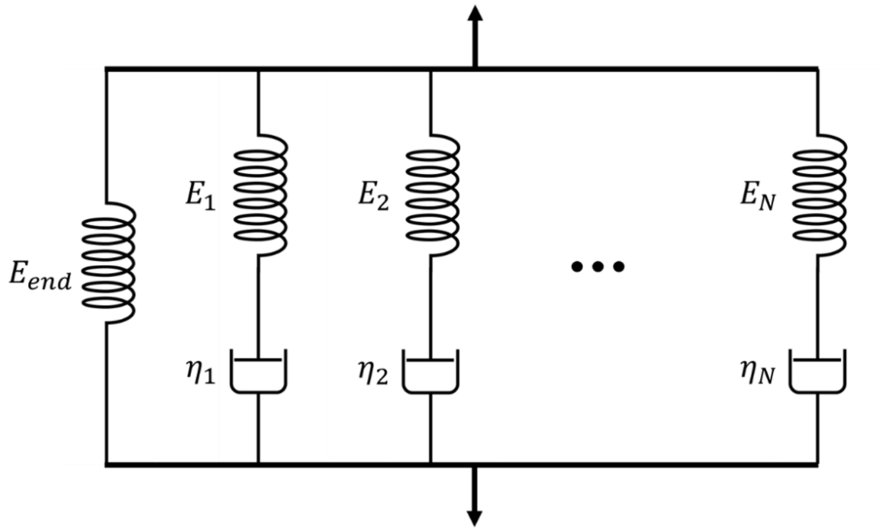

Figure 3-2 Generalized Maxwell model of a viscoelastic material

Y(t, t') can be represented by a Prony series expansion of the relaxation modulus of elasticity

$$Y\left(t,t'\right)=E_{end}+\sum_{m=1}^{N}E_{m}exp\left(-\frac{t-t'}{\tau_{m}}\right) \tag{3-1}$$

In our case (concrete structures in NPPs), a load is usually applied after 1 year of construction (*t′* = 1 year), Let' take *t*=(*t–1*) year, then

$$Y(t) = E_{end} + \sum_{m=1}^{N} E_m exp\left(-\frac{t}{\tau_m}\right) \tag{3-2}$$

$$Y(0) = E_{end} + \sum_{m=1}^{N} E_m = E_0 \tag{3-3}$$

Thus, an alternative form of Equation (3-1) can be obtained, where E_0 is the instantaneous stiffness of concrete

$$Y(t) = E_0 - \sum_{m=1}^{N} E_m \left(1 - exp\left(-\frac{t}{\tau_m}\right)\right) \tag{3-4}$$

In the above equations, the material parameters are defined as follows: E_m is the stiffness of the spring in the element *m*, τ_m is the relaxation time of the element *m*, E_{end} is the steady-state stiffness, and *t* is the time in days.

Usually, the number of elements in the generalized Maxwell model to be used in a creep analysis depends on the time span of the analysis and the characteristics of creep deformation of the material. The time ranges of τ_m should be large enough to cover the time span for the entire creep deformation under consideration. For example, the entire creep deformation of a certain polymer can occur within a year, so the relaxation times of the elements should cover up to one year, while a certain type of rock may have creep deformation occurring in several decades after the loading is applied, and thus the relaxation times should span to 100 years.

In order to use the model to calculate the creep of a concrete, the material parameters in the model must be determined first. To this end, the basic creep parameters will be introduced first, the method to determine the model parameters will be described, the method to include the nuclear irradiation effect will be discussed, the numerical model will be verified and validated, and then a sample analysis will be given. The integration of this creep model with the multiscale and multiphase model described in Chapter 2 is shown in the overall flowchart in Figure 1-2.

3.2 Creep Coefficient and Prony Parameters

The creep coefficient of concrete, ψ is defined as the ratio of creep strain to instantaneous elastic strain, and it can usually be obtained by an accelerated creep test. The creep coefficient can be represented by the ACI equation (ACI 209R-92, Reapproved 2008)

$$\psi(t, t') = \frac{(t - t')^{0.6}}{10 + (t - t')^{0.6}} \psi_u \tag{3-5}$$

in which ψ_u is the ultimate creep coefficient, which is defined as the ratio of the maximum creep strain to the instantaneous elastic strain. Then the relaxation modulus can be expressed as a function of the creep coefficient

$$Y\left(t,t'\right)=\frac{E_0}{1+\psi\left(t,t'\right)} \tag{3-6}$$

In Equation (3-5), ψ_u must be determined before the relaxation modulus can be evaluated. ψ_u can be determined using the creep test data of concrete from a nuclear power plant, if available, which will be shown later using a numerical example. Usually, a creep test was done when a nuclear power plant was built. The data from the test, which may be called the old creep test, can be used to determine $\psi_{u,OLD}$. If another creep test is done at a later stage during the service life of a concrete structure, for example, during a rehabilitation of the structure, which may be called new creep test, then $\psi_{u,NEW}$ can be determined. In this case, a linear interpolation of the old and new creep test data can be used to determine ψ_u. The short-term creep behavior of the concrete which is described by the old creep test data and the long-term creep behavior which is characterized by the new creep test data can be used together. Similarly, an extrapolation based on the two sets of creep test data can also be used to predict future creep. The change of creep behavior of the concrete over time can be considered

$$\psi_u=\psi_{u,OLD}+\frac{\psi_{u,NEW}-\psi_{u,OLD}}{t_{NEW}-t_{OLD}}\left(t-t'\right) \tag{3-7}$$

If there is only one set of creep test data, either old or new, the above equation can be used by assuming that the old and new creep coefficients are exactly the same. Substitute Equation (3-7) and Equation (3-5) into Equation (3-6), then combined with Equation (3-4), the following equation is obtained

$$Y\left(t\right)=E_0-\sum_{m=1}^{N}E_m\left(1-exp\left(-\frac{t}{\tau_m}\right)\right)=\frac{E_0}{1+\frac{t^{0.6}}{10+t^{0.6}}\left(\psi_{u,OLD}+\frac{\psi_{u,NEW}-\psi_{u,OLD}}{t_{NEW}-t_{OLD}}t\right)} \tag{3-8}$$

Equation (3-8) can be used to determine the Prony parameters E_m in a creep analysis. For the creep of concrete, seven elements are usually used for the generalized Maxwell model with seven relaxation times τ_m(m = 1, 2, …, 7). Each element has a specific relaxation time characterizing the creep of concrete in a certain period. For example, the following seven relaxation times τ_m may be used

$\tau_1 = 0.01$ days
$\tau_2 = 0.1$ days
$\tau_3 = 1$ days
$\tau_4 = 10$ days
$\tau_5 = 100$ days
$\tau_6 = 1000$ days
$\tau_7 = 10000$ days

where, for example, τ_1 is for the short-term creep and τ_7 is for the long-term creep. As one can see, each relaxation time represents a decade; for example, τ_7 represents the time range of 10^4 days. It is important to make sure that τ_7 can cover the longest time span used in the analysis. If not, a larger τ_7 should be used. When the seven relaxation times are used one by one in Eq. (3-8), we will obtain seven equations with seven unknown E_m. Thus, E_m can be solved. This method is called the collocation method. The seven collocation points (with the seven relaxation times) can be chosen somewhat arbitrarily. A proper selection of collocation points can produce a set of equations which are easy to solve.

3.3 Generalized Maxwell Model Implementation in ABAQUS CAE

For structural analysis, commercial finite element programs can be used such as ABAQUS. So, the present model was developed with an intention that users can combine the model with ABAQUS. ABAQUS does not allow the assignment of two material models (UMAT and built-in) to one material, which means that the creep model and the damage model cannot be used together to analyze the coupling effect. In order to apply the damage model along with the viscoelastic model later on in ABAQUS, the generalized Maxwell model first needs to be defined using a subroutine (UMAT) in ABAQUS and then combined with the damage model. Formulations for the linear viscoelasticity are developed as follows.

Based on the Boltzmann superposition principle, the Cauchy stress can be obtained by applying the hereditary integral

$$\sigma\left(t\right)=\int_0^t Y(t-s)\frac{\partial\varepsilon}{\partial s}ds \tag{3-9}$$

It should be noted that the stress and strain are zero for $t < 0$ in the above formulation, i.e., the material is undisturbed before time zero. Substitute Equation (3-4) into the above equation and expand

$$\sigma\left(t\right)=\int_0^t E_0\frac{\partial\varepsilon}{\partial s}ds-\sum_{m=1}^{N}\int_0^t E_m\left(1-exp\left(-\frac{t-s}{\tau_m}\right)\right)\frac{\partial\varepsilon}{\partial s}ds \tag{3-10}$$

$$\sigma\left(t\right)=E_0\varepsilon(t)-\sum_{m=1}^{N}E_m\varepsilon(t)+\sum_{m=1}^{N}\int_0^t E_m exp\left(-\frac{t-s}{\tau_m}\right)\frac{\partial\varepsilon}{\partial s}ds \tag{3-11}$$

A normalized form is given below as

$$\sigma\left(t\right)=E_0\left(\varepsilon(t)-\left(\sum_{m=1}^{N}p_m\varepsilon(t)-\sum_{m=1}^{N}p_m\int_0^t exp\left(-\frac{t-s}{\tau_m}\right)\frac{\partial\varepsilon}{\partial s}ds\right)\right) \tag{3-12}$$

where $p_m=E_m/E_0$. The above equation can be rewritten as

$$\sigma\left(t\right)=E_0\left(\varepsilon(t)-\left(\sum_{m=1}^{N}p_m\varepsilon(t)-\sum_{m=1}^{N}p_m\gamma_m\left(t\right)\right)\right) \tag{3-13}$$

where, internal variables for each element are defined as

$$\gamma_m\left(t\right)=\int_0^t exp\left(-\frac{t-s}{\tau_m}\right)\frac{\partial\varepsilon}{\partial s}ds \tag{3-14}$$

For a relaxation test, the internal variable $\gamma_m(t)$ will be zero once the time t approaches infinity. Under a constant deformation, the stress on the material will eventually relax to the stress of the spring element, as shown in Figure 3-2. In order to determine the values of $\gamma_m(t)$, a time interval $[t_n,t_{n+1}]$ is considered.

$$\gamma_m\left(t_{n+1}\right)=\int_0^{t_{n+1}} exp\left(-\frac{t_{n+1}-s}{\tau_m}\right)\frac{\partial\varepsilon}{\partial s}ds \tag{3-15}$$

The loading history can be separated into two parts based on time, i.e., from 0 to t_n, and from t_n to t_{n+1}, then the following formulation is obtained

$$\gamma_m\left(t_{n+1}\right)=\int_0^{t_n} exp\left(-\frac{t_{n+1}-s}{\tau_m}\right)\frac{\partial\varepsilon}{\partial s}ds+\int_{t_n}^{t_{n+1}} exp\left(-\frac{t_{n+1}-s}{\tau_m}\right)\frac{\partial\varepsilon}{\partial s}ds \tag{3-16}$$

The time increment $\Delta t = t_{n+1} - t_n$,

$$\gamma_m\left(t_{n+1}\right)=exp\left(-\frac{\Delta t}{\tau_m}\right)\int_0^{t_n} exp\left(-\frac{t_n-s}{\tau_m}\right)\frac{\partial\varepsilon}{\partial s}ds+\int_{t_n}^{t_{n+1}} exp\left(-\frac{t_{n+1}-s}{\tau_m}\right)\frac{\partial\varepsilon}{\partial s}ds \tag{3-17}$$

Based on Equation (3-14), the above equation can be further written as

$$\gamma_m\left(t_{n+1}\right)=exp\left(-\frac{\Delta t}{\tau_m}\right)\gamma_m\left(t_n\right)+\int_{t_n}^{t_{n+1}} exp\left(-\frac{t_{n+1}-s}{\tau_m}\right)\frac{\partial\varepsilon}{\partial s}ds \tag{3-18}$$

The integration term in the above equation can be further simplified based on the assumption of constant strain rate which is

$$\frac{\partial\varepsilon}{\partial s}=\lim_{\Delta t\to 0}\frac{t_{n+1}-t_n}{\Delta t}=\frac{\Delta\varepsilon}{\Delta t} \tag{3-19}$$

The solution of internal variables is obtained as

$$\gamma_m\left(t_{n+1}\right)=exp\left(-\frac{\Delta t}{\tau_m}\right)\gamma_m\left(t_n\right)+\frac{\tau_m}{\Delta t}\left(1-exp\left(-\frac{\Delta t}{\tau_m}\right)\right)\Delta\varepsilon \tag{3-20}$$

This equation indicates that $\gamma_m(t)$ is dependent on its own preceding values. In order to determine the current value of $\gamma_m(t)$, all the previous values must be obtained first and stored at each given time step. For $t = t_{n+1}$, Equation (3-13) becomes

$$\sigma\left(t_{n+1}\right)=E_0\left(\varepsilon(t_{n+1})-\left(\sum_{m=1}^{N}p_m\varepsilon(t_{n+1})-\sum_{m=1}^{N}p_m\gamma_m\left(t_{n+1}\right)\right)\right) \tag{3-21}$$

The creep strain is defined as

$$\epsilon^c(t_{n+1})=\sum_{m=1}^{N}p_m\varepsilon(t_{n+1})-\sum_{m=1}^{N}p_m\gamma_m\left(t_{n+1}\right) \tag{3-22}$$

Therefore, the one-dimensional solution of linear viscoelasticity is obtained by

$$\sigma\left(t_{n+1}\right)=E_0\varepsilon^e(t_{n+1})=E_0(t_{n+1})\left(\varepsilon(t_{n+1})-\varepsilon^c(t_{n+1})\right) \tag{3-23}$$

For three-dimensional problems, an index tensor notation can be used. The stress tensor of a viscoelastic material at time $t = t_{n+1}$ can be calculated using the following equations

$$\sigma_{ij}^{n+1} = C_{ijkl}^{e}\varepsilon_{ij}^{e,n+1} = C_{ijkl}^{e}\left(\varepsilon_{ij}^{n+1} - \varepsilon_{ij}^{c,n+1}\right) \tag{3-24}$$

$$\varepsilon_{ij}^{c,n+1} = \sum_{m=1}^{N} p_m \varepsilon_{ij}^{n+1} - \sum_{m=1}^{N} p_m \gamma_{mij}^{n+1} \tag{3-25}$$

$$\gamma_{mij}^{n+1} = exp\left(-\frac{\Delta t}{\tau_m}\right)\gamma_{mij}^{n} + \frac{\tau_m}{\Delta t}\left(1 - exp\left(-\frac{\Delta t}{\tau_m}\right)\right)\Delta\varepsilon_{ij} \tag{3-26}$$

where C_{ijkl}^{e} is the stiffness tensor. For each stress component, there are seven associated internal variables, and the total number of internal variables at each time step is forty-two. Based on the constitutive relationship defined above, a subroutine UMAT in ABAQUS was developed to solve creep problems of concrete using the finite element method (FEM).

3.4 Mazars' Damage Model

In the continuum damage mechanics, the damage is considered to be isotropic, with no preferred orientation. The mechanical damage in an isotropic material is described by a scalar damage variable *D*. This parameter characterizes the variation of the stiffness of the material. The behavior for a stress state is governed by the following general equation

$$\sigma = (1 - D)\,\mathbf{C}^{e} : \varepsilon^{e} \tag{3-27}$$

where ε^{e} is the elastic strain which is equal to the total strain subtracted other strains, i.e., the creep strain as shown in Equation (3-25). *D* is a scalar value ranging from 0 for the intact condition to 1, which represents the completely damaged material. When *D* = 0, the material is linear elastic; and when *D* = 1, the stress is zero, which means the material cannot hold any load. Various models were developed for the parameter *D*. In this study, Mazars' damage model (Mazars 1986; Mazars and Pijaudier-Cabot 1989) was adopted due to its simplicity and robustness in calculating this parameter. In our case, the creep analysis is considered for a sustained load with a low stress level (short-term high stress level loadings such as earthquakes and stress concentration at the tip of discrete cracks are not considered), so the nonlocal treatment is not used.

Mazars' damage model is a continuum damage model developed for concrete material. It can be used to describe the damage due to the creation of microscopic cracks in the concrete. Damage development in concrete depends on the loading process. The equivalent tensile strain is defined as

$$\tilde{\epsilon} = \sqrt{\sum_{i=1}^{3}\left(\langle \epsilon_i \rangle_{+}\right)^{2}} \tag{3-28}$$

where ϵ_i are the principal strains and $\langle . \rangle_{+}$ is the Macauley bracket, which defined as

$$\langle x \rangle_{+} = x \text{ if } x \geq 0 \text{ , otherwise } \langle x \rangle_{+} = 0$$

It needs to be noted that only elastic strain contributes to mechanical damage development. The loading function of damage is

$$f\left(\tilde{\epsilon}, \kappa\right) = \tilde{\epsilon} - \kappa \tag{3-29}$$

where κ is the threshold of damage. Its initial value κ_0 can be obtained from the maximum tensile strength f_t and the initial elastic modulus E_0 of the material in uniaxial tension test: $\kappa_0 = f_t/E_0$. κ is constantly updated by the largest value of the equivalent strain ever reached by the material in the loading history at the current time. The damage evolution algorithm is described as

If $f\left(\tilde{\epsilon}, \kappa\right) = 0$ and $\dot{f}\left(\tilde{\epsilon}, \kappa\right) = 0$, then

$$\begin{cases} D_M = g(\tilde{\epsilon}) \\ \kappa = \tilde{\epsilon} \end{cases} \text{with } \dot{D_M} \geq 0, \text{ else } \begin{cases} \dot{D_M} = 0 \\ \dot{\kappa} = 0 \end{cases} \tag{3-30}$$

where D_M stands for the damage variable for the mechanical damage (there will be another variable for the irradiation damage). The total mechanical damage is a combination of mechanical damage in tension and mechanical damage in compression, which is

$$g(\tilde{\epsilon}) = \alpha_t d_t + \alpha_c d_c \tag{3-31}$$

where d_t and d_c are the damage variables corresponding to tension and compression, respectively. They are combined with the weighting coefficients α_t and α_c calculated from tensile and compressive strains:

$$\alpha_t = \sum_{i=1}^{3} \frac{\langle \epsilon_i^t \rangle \langle \epsilon_i \rangle_+}{\tilde{\epsilon}^2} \qquad \alpha_c = \sum_{i=1}^{3} \frac{\langle \epsilon_i^c \rangle \langle \epsilon_i \rangle_+}{\tilde{\epsilon}^2} \tag{3-32}$$

where the superscripts *t* and *c* also represent tension and compression, respectively, and strains labeled with a single indicium are principal strains. Tensile and compressive principal strains are calculated from the tensile and compressive strain tensor defined as

$$\epsilon^t = \mathbf{C}^{-1} : \sigma^t \tag{3-33}$$

$$\epsilon^c = \varepsilon - \epsilon^t \tag{3-34}$$

The damage evolutions laws for d_t and d_c are provided as a function of equivalent tensile strain:

$$d_t = 1 - \frac{\kappa_0\left(1 - A_t\right)}{\tilde{\epsilon}} - \frac{A_t}{\exp\left(B_t\left(\tilde{\epsilon} - \kappa_0\right)\right)} \tag{3-35}$$

$$d_c = 1 - \frac{\kappa_0\left(1 - A_c\right)}{\tilde{\epsilon}} - \frac{A_c}{\exp\left(B_c\left(\tilde{\epsilon} - \kappa_0\right)\right)} \tag{3-36}$$

where A_t, B_t, A_c, and B_c are characteristic parameters of the material which define the post-peak material behavior under compression and tension. A governs the residual strength beyond the peak value, and B controls the peak strength itself and the slope of the softening branch.

For uniaxial tension, $\alpha_t = 1$, $\alpha_c = 0$, $D_M = d_t$, and vice versa for uniaxial compression. Therefore, A_t and B_t can be obtained from bending tests of concrete beams, and A_c and B_c can be measured in compression tests of concrete cylinders.

3.5 Coupled Damage-Creep Modeling of Nuclear Irradiated Concrete

Since ABAQUS cannot handle coupled damage-creep analysis through built-in viscoelastic models and damage models, the constitutive model needs to be defined using subroutine UMAT by combining the Mazars' damage model and generalized Maxwell model. This step is shown by the box in the lower right corner in Figure 3-1.

It is assumed that the mechanical and nuclear irradiation damages act as two independent damage processes at the same time. Thus, their total effect can be considered in the multiplicative way, and the isotropic scalar damage variable *D* can be expressed as

$$D = 1 - (1 - D_{Mech})\,(1 - D_{Rad}) \tag{3-37}$$

where D_{Mech} is the parameter for mechanical damage and D_{Rad} is the parameter for the damage induced by nuclear irradiation and thermal effect. D_{Rad} is a constant value within each time step, and it could be different in different time steps. It is the volume fraction of the distressed concrete phase under nuclear irradiation obtained by the multiphase and multiscale model developed in Chapter 2 and Equation **Error! Reference source not found.** in Chapter 4.

The nuclear irradiation-induced degradation and creep of concrete are both long-term behaviors of concrete, and they are considered to occur simultaneously. Since the strength and stiffness of the concrete are expected to be reduced due to the nuclear irradiation, the creep of the irradiated concrete is expected to be higher. The damage factor (*1 - D*) can be considered as a stress multiplier. The degradation of concrete induced by nuclear irradiation and mechanical loading can be included in the viscoelastic analysis of the concrete. The constitutive equations are shown as follows

$$\sigma_{ij}^{n+1} = \left(1 - D^{n+1}\right) C_{ijkl}^{e} \varepsilon_{ij}^{e,n+1} = \left(1 - D^{n+1}\right) C_{ijkl}^{e} \left(\varepsilon_{ij}^{n+1} - \varepsilon_{ij}^{c,n+1}\right) \tag{3-38}$$

$$D^{n+1} = 1 - \left(1 - D_{Mech}\left(\tilde{\epsilon}^{n+1}\right)\right)\left(1 - D_{Rad}\right) \tag{3-39}$$

$$\varepsilon_{ij}^{c,n+1} = \sum_{m=1}^{N} p_m \varepsilon_{ij}^{n+1} - \sum_{m=1}^{N} p_m \gamma_{mij}^{n+1} \tag{3-40}$$

$$\gamma_{mij}^{n+1} = exp\left(-\frac{\Delta t}{\tau_m}\right)\gamma_{mij}^{n} + \frac{\tau_m}{\Delta t}\left(1 - exp\left(-\frac{\Delta t}{\tau_m}\right)\right)\Delta\varepsilon_{ij} \tag{3-41}$$

3.6 Model Verifications and Examples

Comparisons between the simulation results from UMAT and the experimental data/available results from the open literature are given in this section.

3.6.1 Verification of Mazars' Damage Model

The uniaxial tension and compression test are performed on a cubic specimen (10 cm × 10 cm × 10 cm) in ABAQUS using the following parameters: E_0 = 30 GPa, ν = 0.2, κ_0 = 0.0001, A_t = 1, B_t = 15000, A_c = 1.2, B_c = 1500. As shown in Figure 3-3, eight elements were used and each element size is 5 cm × 5 cm × 5 cm. Constant strain rates of tension and compression boundary conditions (displacement controlled) are applied at the top surface until the complete failure of the specimen occurs. The bottom surface is fixed in the *Y* direction, and all other boundaries are stress-free. The stress-strain relationship is obtained from Mazars' damage model (implemented via ABAQUS UMAT) and compared with the result given by Pijaudier-Cabot and Mazars (2001) in Figure 3-4. The comparison shows that the ABAQUS simulations agree with the available results in tension and in compression, and the accuracy of the developed UMAT of the Mazars' damage model is good.

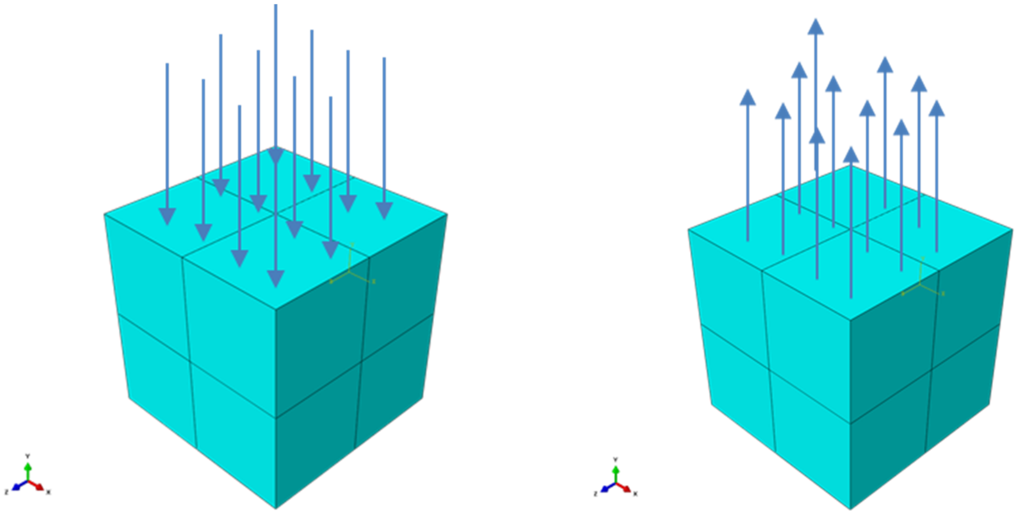

Figure 3-3 FEM model for uniaxial compression and tension test simulation

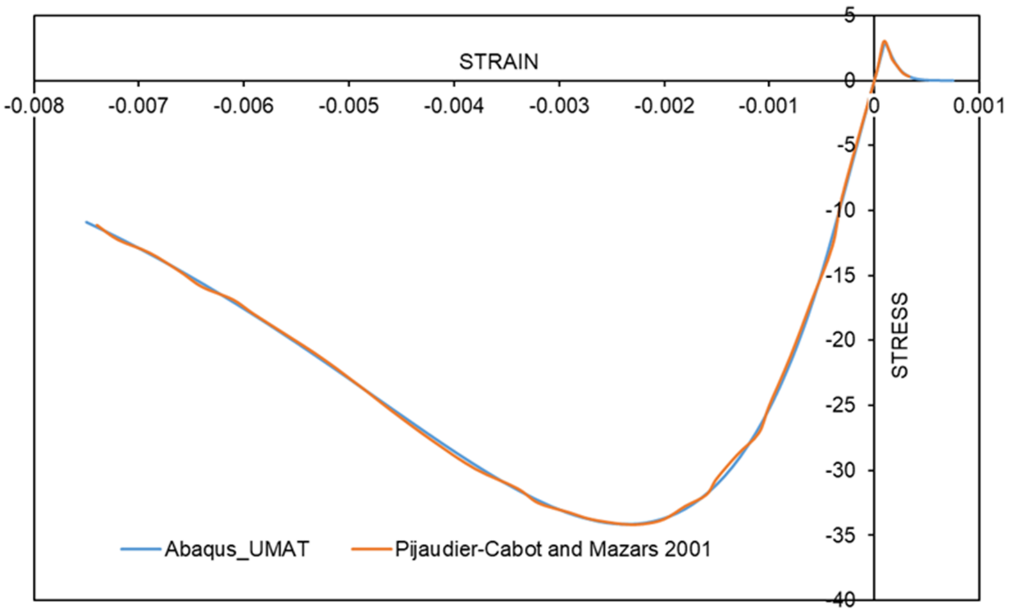

Figure 3-4 Comparison of stress-strain relationship for Mazars' damage model (implemented via ABAQUS UMAT) and results from Pijaudier-Cabot and Mazars (2001)

3.6.2 Verification and Validation of the Creep Model

Both the relaxation test and creep test for concrete under tension using ABAQUS UMAT with the generalized Maxwell model and ABAQUS built-in generalized Maxwell model were performed up to 5000 seconds. The finite element model is the same as shown in Figure 3-3. The input parameters are E_0 = 39.6 GPa, ν = 0.2, and the Prony series parameters are listed in Table 3-1. As shown in Figure 3-5 and Figure 3-6, both methods have exactly the same results, indicating that the UMAT results of the generalized Maxwell model developed in this project are correct. As discussed earlier, the advantage of the present UMAT creep model is that it can be combined with the Mazars' damage model to consider the effect of damage on creep development. It should be pointed out that other damage models also can be used in combination with the creep model.

Table 3-1 Prony series parameters for verification of the generalized Maxwell model

τ_m(s)	0.02	0.2	2	20	200	2000	20000
p_m	0.0221	0.0524	0.2068	0.2739	0.0946	0.0372	0.0758

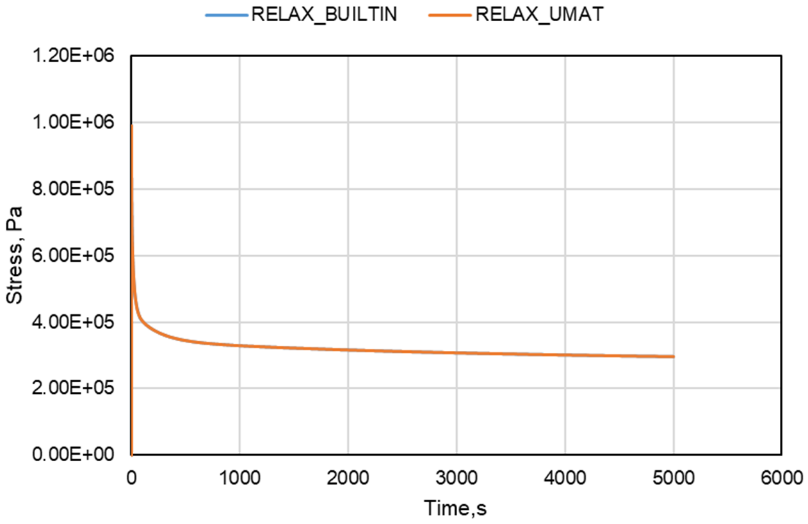

Figure 3-5 Relaxation test with constant tensile strain 0.000025

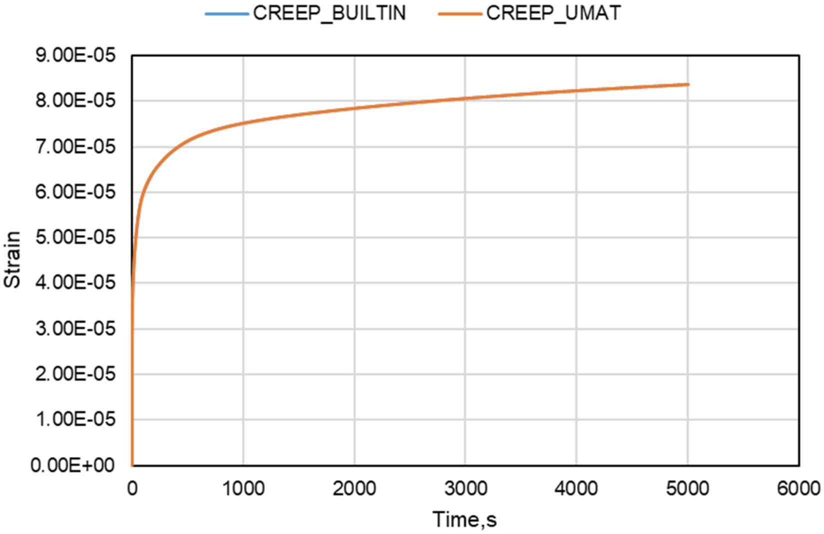

Figure 3-6 Creep test with constant tension 1 MPa

The set of compression creep test data (Townsend 2003) shown in Table 3-2 is used for the validation of the creep modeling. The first column in the table is time. The second column is the total strain measured during the test, and the creep strains are shown in column 3. After 28 days, the compressive strength is 86.9 MPa, and the modulus of elasticity is 43.7 GPa. The applied stress is 30% of the compressive strength, which is 26.07 MPa. The creep strain at t = 0 was considered as zero, and the other creep strains are listed in Table 3 2 starting from the duration of one day.

Figure 3-7 shows the creep test data of the creep coefficient and the ACI curve for the creep coefficient $\psi(t, t')$ in Equation (3-5). The ultimate creep coefficient ψ_u is determined by curve fitting the creep test data with Equation (3-5), and the result is an ultimate creep coefficient of 1.8, as shown in the figure.

It is assumed that the testing conditions are the same as the operating conditions of the structure, and thus, the ACI correction factors are not needed for the ultimate creep coefficient (for a real creep analysis, ACI correction factors may need to be added). The Prony parameters can be obtained through Equation (3-8) as shown in Table 3-3. Here, we assumed that the old and new test results are exactly the same. Prony series parameters were then used as inputs in ABAQUS for creep analysis. The creep strain obtained is compared with the test data and the ACI equation, as shown in Figure 3-8. They agree well with each other.

Table 3-2 Creep test data

t (days)	Total strain ($\times 10^{-6}$)	Creep strain ($\times 10^{-6}$)	Creep coefficient (Creep strain/ instantaneous elastic strain)*
1	727	116	0.1943
2	790	139	0.23283
3	841	173	0.28978
4	857	184	0.30821
5	919	223	0.37353
6	947	265	0.44389
13	1080	320	0.53601
20	1151	379	0.63484
27	1194	435	0.72864
34	1263	489	0.8191
41	1243	484	0.81072
48	1306	516	0.86432
55	1321	516	0.86432
62	1355	553	0.9263
69	1357	547	0.91625
76	1370	543	0.90955
83	1353	533	0.8928
90	1357	547	0.91625
97	1374	545	0.9129
104	1386	557	0.933

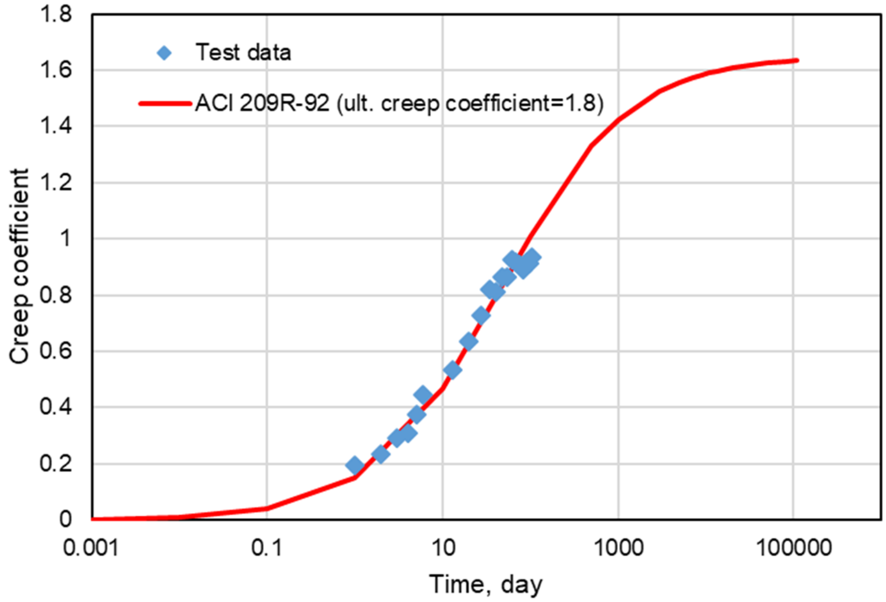

Figure 3-7 The creep test data and the ACI curve for the creep coefficient

Table 3-3 Prony series parameters obtained

τ_m (day)	0.01	0.1	1	10	100	1000	10000
p_m	0.0104	0.024	0.1118	0.2491	0.1636	0.0425	0.0192

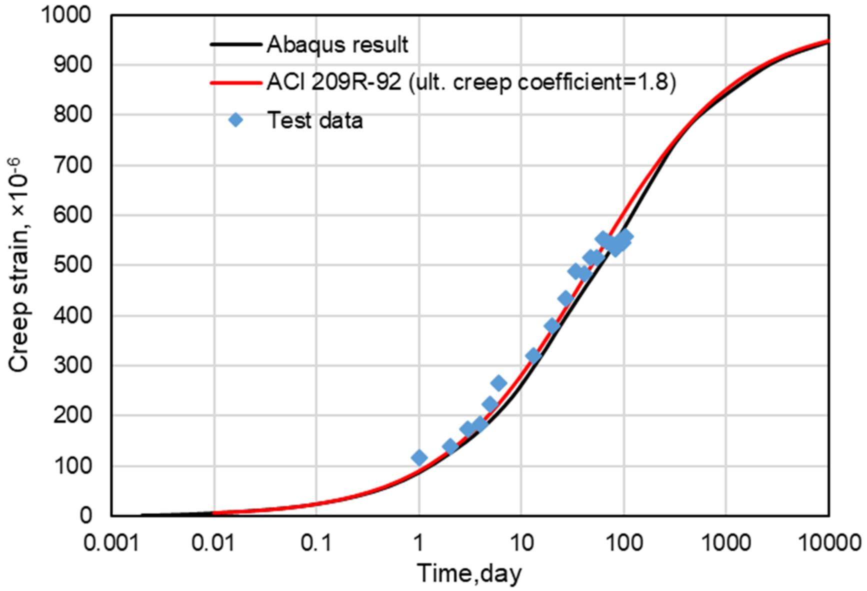

Figure 3-8 Comparison between test data, ACI equation, and ABAQUS results

3.6.3 Analysis of an Example

A numerical example for a concrete cube under uniaxial tension and neutron irradiation is used as a sample analysis to examine the performance of the coupled creep-damage model. The finite element model is shown in Figure 3-3 under tension. Some inputs used in the sample analysis: w/c = 0.4, aggregate dimensional change is Profile 1 with 4E19 n/cm^2 (E > 0.1 MeV) neutron fluence over 60 years as shown in Figure 2-20, $E_0 = 3.96 \times 10^{10}$ Pa, $\upsilon = 0.273$. Prony series parameters are listed in Table 2-13-1. Parameters for Mazars' damage model used in Section 3.6.1 are still used for this example which are f_{t0} = 4 MPa, A_t = 1, B_t = 15000, A_c =1.2, B_c =1500. As stated in Section 3.4, these parameters define the post-peak material behavior under compression and tension and can be measured through compression and tension tests of concrete specimens. The scalar damage parameter for radiation damage D_{Rad} shown in Figure 3-9 is the volume fraction of the distressed concrete phase under neutron irradiation which was obtained based on Profile 1 in Figure 2-20 in Chapter 2 and Equation (4-9) in Chapter 4. The damage evolution and response of the material with and without considering creep are shown in Figure 3-10 and Figure 3-11. Creep affects the damage development significantly. From Figure 3-10 one can see that, for example, at 5000 days, the damage without considering creep is more than 90%, and it is less than 60% by considering the effect of creep. So, the creep of concrete can relax the stresses and reduce the damage in concrete significantly.

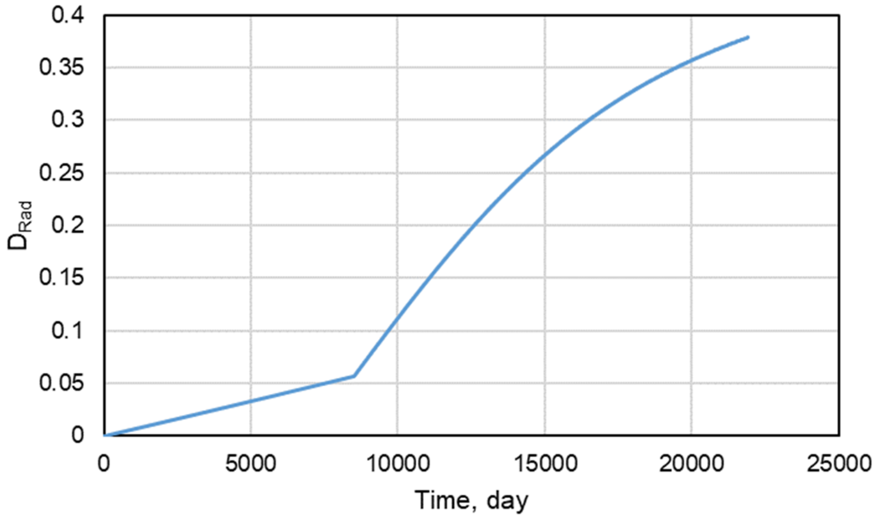

Figure 3-9 The scalar damage parameter for radiation damage D_{Rad}

Figure 3-10 Total scalar damage parameter *D* with and without considering creep

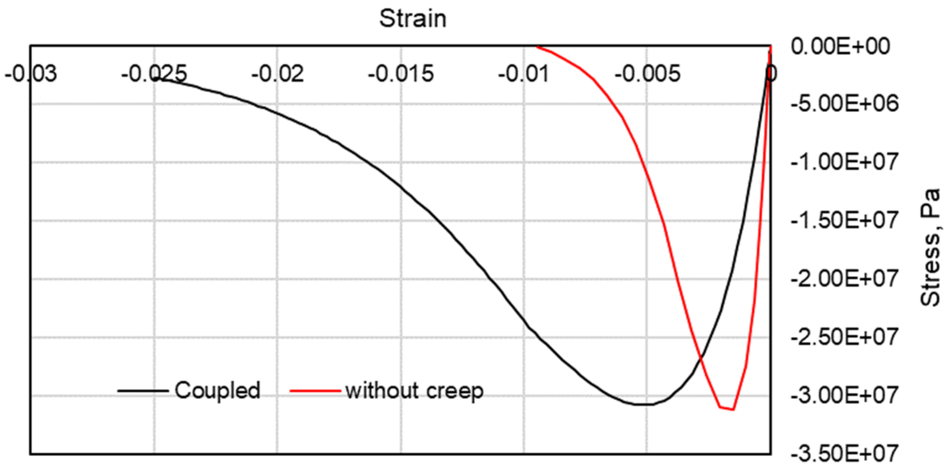

Figure 3-11 Stress-strain relationships with and without considering creep

This is just one example. In Chapter 6, the robustness of the developed UMAT code will be tested by simulating a part of a model concrete structure in an NPP.

3.7 Summary

For concrete material under long-term nuclear irradiation, damage and creep occur concurrently, and ABAQUS cannot handle coupled damage-creep analysis through built-in viscoelastic models and damage models. A coupled damage-creep model of nuclear irradiated concrete was developed based on the generalized Maxwell model and Mazars' damage model, and was implemented in ABAQUS through subroutine UMAT. The theory of the generalized Maxwell model was first introduced. Based on the ACI equation and creep test data, the Prony parameters used in the generalized Maxwell model can be determined. Then, formulations for the linear viscoelasticity based on the generalized Maxwell model were derived. The coupled damage-creep constitutive model was defined by combining the isotropic scalar damage model and the generalized Maxwell model. The damage factor (1 - *D*), which characterizes the stiffness reduction of the material, includes two independent damage processes: the mechanical damage obtained through Mazars' damage model and the nuclear irradiation damage estimated based on the multiphase and multiscale model from Chapter 2. To ensure the accuracy of the developed models using the ABAQUS subroutine UMAT, comparisons between the results of the present models and the experimental data/available results from the open literature were shown. The performance of the coupled creep-damage model was examined through a numerical example for a concrete specimen under uniaxial tension and neutron irradiation.

4 LONG-TERM NEUTRON RADIATION LEVELS IN DISTRESSED CONCRETE

Neutron radiation can cause damage to concrete materials, which was characterized in Chapter 2. The effect of damage will have an impact on mechanical properties as described in Chapter 2, and it will also have an impact to a certain extent on the neutron shielding capacity of the concrete, which is the focus of this chapter. Since the mechanical properties of concrete can be degraded under nuclear radiation and elevated temperatures, the neutron transport properties of concrete can be degraded, too. With degraded neutron transport properties, the neutron flux profile in a biological shielding wall will be different from the wall with intact concrete. In the literature, the neutron flux profile in a biological shielding wall has been considered to be unchanged with time (Field et al. 2015; Maruyama et al. 2016; Pomaro et al. 2011a, b). In this chapter, the neutron radiation distributions in a concrete biological shielding wall will be predicted by taking into account the possible degradation of neutron transport properties induced by neutron radiation and elevated temperatures. The prediction model was developed by considering a multigroup neutron diffusion equation, heat conduction analysis, cross-property correlation theories (see Section 4.2.1), and the theoretical models developed in previous chapters, as shown in Figure 4-1.

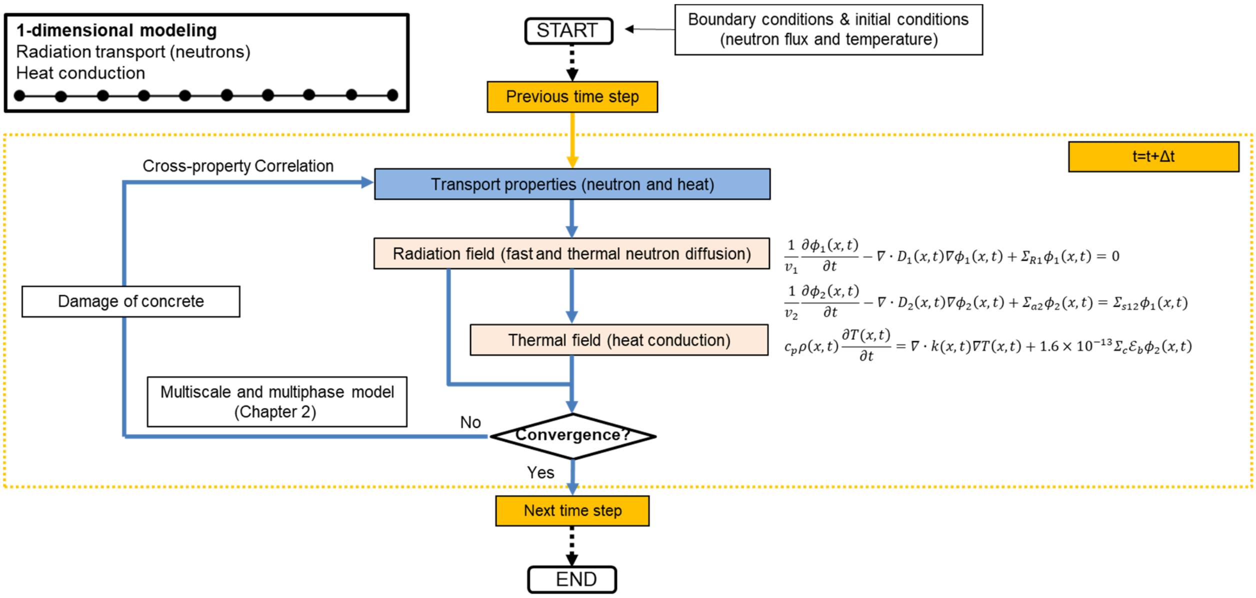

Figure 4-1 Calculation flow chart for neutron diffusion and heat conduction

4.1 Neutron Transport and Heat Conduction

4.1.1 Neutron Transport

There are two methods used for neutron transport calculations: Monte Carlo simulation and a deterministic method (Shultis and Faw 1996). The Monte Carlo simulation method is based on probability and statistical theories to simulate the migration of neutron particles in a medium. It can accurately model the exact geometry and simulate physical experiments. Although there are no truncation errors, this method suffers from the stochastic uncertainties and slow convergence rate. Compared with the Monte Carlo simulation, the deterministic method is difficult to apply to problems with complex geometries, and some simplifications are needed. However, the deterministic method usually can obtain results more quickly through discretization of the transport equation and the utilization of the proper numerical methods. Besides, this approach describes the radiation field and gives the solution for the expected fluence or flux density of the radiation particles throughout the shielding medium, which makes it easy to combine the approach with the material models developed in this study. Thus, the deterministic method is the approach adopted for this study. The governing equation is known as the neutron transport equation (Duderstadt and Hamilton 1976).

$$\begin{aligned}\frac{\partial n}{\partial t} + v\hat{\boldsymbol{\Omega}} \cdot \boldsymbol{\nabla} n + v\Sigma_t n(\boldsymbol{r}, \mathcal{E}, \hat{\boldsymbol{\Omega}}, t) \\ = \int_{4\pi} d\hat{\boldsymbol{\Omega}}' \int_{\boldsymbol{0}}^{\infty} \boldsymbol{d}\mathcal{E}' v' \, \Sigma_s(\mathcal{E}' \to \mathcal{E}, \hat{\boldsymbol{\Omega}}' \to \hat{\boldsymbol{\Omega}}) n(\boldsymbol{r}, \mathcal{E}', \hat{\boldsymbol{\Omega}}', t) + \boldsymbol{S}(\boldsymbol{r}, \mathcal{E}, \hat{\boldsymbol{\Omega}}, t)\end{aligned} \tag{4-1}$$

where n is the angular neutron density; v is neutron speed; Σ_t is the total macroscopic cross section; Σ_s is the macroscopic scattering cross section; $\boldsymbol{S}$ is the internal neutron source term; $\boldsymbol{r}$ is a position vector; $\mathcal{E}$ is the neutron energy; $\hat{\boldsymbol{\Omega}}$ is **a** unit vector describing the direction of neutron motion; and t is time. This equation contains seven independent variables ($\boldsymbol{r} = x, y, z$; $\mathcal{E}$; $\hat{\boldsymbol{\Omega}} = \beta, \gamma$; t) and is very complex and difficult to solve. Therefore, several approaches have been developed to simplify the equation, such as exponential attenuation, diffusion approximation, and the method of moments (Shultis and Faw 1996). Exponential attenuation is the simplest method among them and is rigorously true only for un-collided radiation. The applicable situations are therefore very limited. The method of moment can obtain the spatial and energy distribution of particles by directly solving the transport equation. However, this method is practically restricted to problems with infinite medium and simple sources. The diffusion approximation neglects the angular distribution of the flux density, which is not needed for most shielding applications, including this study. This method makes the transport equation much simpler to solve numerically or analytically. Therefore, the diffusion approximation will be used in this study.

4.1.1.1 One-speed neutron diffusion

For the diffusion approximation, neutron energy dependence could be eliminated and the so-called “one-speed” diffusion could be assumed. “One-speed” means one neutron energy level is considered in the analysis, and it does not change during a scattering collision. Of course, such an assumption is an oversimplification of the actual neutron transport process, since the neutron energy in a nuclear reactor usually has a wide range and neutron cross sections are sensitive to the energy. However, it was found that the one-speed neutron diffusion equation gives reasonable estimates, if the cross sections involved are appropriately chosen (e.g., cross sections are properly averaged over the energy distribution) (Duderstadt and Hamilton 1976; Shultis and Faw 1996). Moreover, the one-speed neutron diffusion can serve as the basis of the more sophisticated models, such as multigroup diffusion theory in which more than one energy level can be considered. As shown in the next section, the multigroup diffusion theory can be developed based on a sequence of one-speed diffusion equations for each successive energy group. The governing equation for one-speed diffusion is shown below.

$$\frac{1}{v}\frac{\partial \phi(x,t)}{\partial t} - \boldsymbol{\nabla} \cdot \mathcal{D}(x) \boldsymbol{\nabla} \phi(x,t) + \Sigma_a(x)\phi(x,t) = \boldsymbol{S}(x,t) \tag{4-2}$$

where ϕ is the scalar neutron flux in n/(cm^2·sec); v is the neutron speed in cm/sec; $\mathcal{D}$ is the neutron diffusion coefficient in cm; Σ_a is the macroscopic absorption cross section in cm^{-1}; $\boldsymbol{S}$ is the internal neutron source term in n/(cm^3·sec); and x and t are position and time in cm and sec, respectively. Initial conditions and boundary conditions need to be used along with the above equation to obtain the solution of neutron flux.

In many cases, the neutron diffusion medium, such as water, is a homogeneous material, and its properties do not change over time so that $\mathcal{D}$ and Σ_a are constants. For a shielding wall with thickness *L* suffering neutron radiation from an external source with the initial condition: $\phi(x,0) = 0$ (no neutrons at the beginning) and boundary conditions: $\phi(0,t) = A$ (a constant value), $\phi(L,t) = 0$ (constant flux source at the inner surface of the wall and no flux on the outer side of the wall), the linear one-dimensional solution for the neutron flux profile is obtained by using separation of variables,

$$\phi(x,t) = -\frac{R}{L}(x-L) + \sum_{n=1}^{\infty} T_n(t)\sin\frac{n\pi x}{L}\ , n = 1,2,\dots \qquad (4\text{-}3)$$

where

$$T_n(t) = e^{-(\beta_n^2+b)t}T_n(0) + \frac{w_n}{\beta_n^2+b}\left(1-e^{-(\beta_n^2+b)t}\right)$$

$$T_n(0) = -\frac{2R}{n\pi},\ w_n = -\frac{2bR}{n\pi},\ \beta_n = \frac{na\pi}{L},\ a = \sqrt{\mathcal{D}v}, b = \Sigma_a v$$

The detailed derivation for the solution is shown in Appendix A.5 .

4.1.1.2 Multigroup neutron diffusion

As stated above, one very important assumption was made for the one-speed neutron diffusion model, which is that neutrons are characterized by only one single energy level that does not change during a scattering collision. However, the neutrons from reactors usually have a very wide energy spectrum ranging from 10 MeV down to less than 0.01 eV, and the neutron cross sections are also energy dependent. Thus, a more realistic consideration of the neutron energy dependence is needed.

Instead of treating the neutron energy as a continuous variable, the energy domain of neutrons can be divided into a set of energy groups. The neutrons inside each group were assumed to behave as one-speed particles, and the neutron source in one group includes the secondary neutrons from scattering reactions in the other groups with higher energy. Usually, no up-scattering from a group with lower energy to the groups with higher energy is considered.

Sufficient accuracy can be achieved by using only a few energy groups, but the group-averaged parameters must be carefully determined. Two energy groups (two energy levels) can be used for the analysis of neutron-irradiated concrete. One group is to characterize fast neutrons (1 eV~10 MeV) and the other thermal neutrons (0 eV~1 eV), as shown in Figure 4-2. The value of energy used here to separate the fast and thermal groups (1 eV) is only for illustrative purposes. It is not a fixed value, and it can be adjusted based on the specific problem. The neutron source in the thermal group included the production of secondary neutrons from scattering reactions of fast neutrons. Thermal neutrons could never gain energy in a scattering collision and become fast neutrons. Fast neutrons slow down during the process. The governing equations are listed below for fast and thermal neutrons, respectively (Duderstadt and Hamilton 1976).

$$\frac{1}{v_1}\frac{\partial \phi_1(x,t)}{\partial t} - \nabla \cdot \mathcal{D}_1(x,t)\nabla\phi_1(x,t) + \Sigma_{R1}\phi_1(x,t) = 0 \tag{4-4}$$

$$\frac{1}{v_2}\frac{\partial \phi_2(x,t)}{\partial t} - \nabla \cdot \mathcal{D}_2(x,t)\nabla\phi_2(x,t) + \Sigma_{a2}\phi_2(x,t) = \Sigma_{s12}\phi_1(x,t) \tag{4-5}$$

where Σ_R is the macroscopic removal cross section in cm^{-1}; Σ_{s12} is the macroscopic fast to thermal group-transfer cross section; subscripts 1 and 2 = fast group and thermal group, respectively.

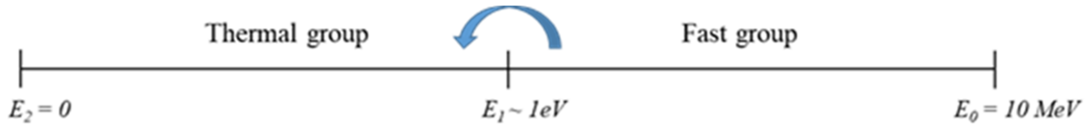

Figure 4-2 The group structure of two-group neutron diffusion model

Usually, the neutron diffusion medium can be treated as a homogeneous material, and its properties do not change with the time, so both $\mathcal{D}$ and Σ are constants. However, in our case, the neutron transport properties of a concrete wall could be affected by the damage induced by neutron radiation and elevated temperatures. As a result, the parameters shown in Equation (4-4) and Equation (4-5), especially, $\mathcal{D}_1$ and $\mathcal{D}_2$, cannot be simply treated as constants. As shown in the previous chapters, the level of damage in a concrete wall depends on the level of neutron fluence which depends on the position in the wall. Therefore, both of the parameters $\mathcal{D}_1$ and $\mathcal{D}_2$ are actually position- and time-dependent variables.

4.1.2 Heat Conduction

The biological shielding wall in a NPP is usually surrounded by an environment whose temperature is above ambient temperature. Nuclear radiation can further lead to localized temperature increases in the concrete. Thus, the temperature profile of the neutron-irradiated concrete is needed. The temperature profile within a medium depends on the rate of its internally generated heat, its capacity to store the heat, and the rate of thermal conduction to the boundaries. The classical one-dimensional heat conduction equation is shown as follows

$$c_p\rho\frac{\partial T(x,t)}{\partial t} = \boldsymbol{\nabla} \cdot k\boldsymbol{\nabla}T(x,t) + Q(x,t) \tag{4-6}$$

where x is location in cm, t is time in sec, c_p is specific heat capacity in J/(kg·K), ρ is mass density in kg/cm^3, T is temperature in K, k is thermal conductivity in W/(cm·K), and Q is the volumetric heat source in W/cm^3.

Neutron radiation generates heat in the material through three primary interactions: capture, elastic scattering, and inelastic scattering (Yevick 1966). However, the heat generated during the attenuation is quite small compared to the heat caused during the capture process (Price et al. 1957). Therefore, the volumetric heating rate caused by neutron radiation can be estimated by only considering the heat generation due to thermal neutron capture (El-Sayed Abdo and Amin 2001; William et al. 2013; Yevick 1966)

$$Q(x,t) \approx 1.6 \times 10^{-13} \Sigma_c \mathcal{E}_b \phi_2(x,t) \tag{4-7}$$

where Σ_c is the macroscopic capture cross section of the transport media for neutrons in cm^{-1} and $\mathcal{E}_b$ is the binding energy for capture reaction in MeV. It is assumed that gamma, beta, or alpha radiation emitted during neutron capture is absorbed at once, and the heat is released immediately.

Like the neutron transport problem, the parameters in Equation (4-6), especially ρ and k, could possibly be affected by radiation and elevated temperature, so these two parameters should also be position- and time-dependent variables.

4.2 Determination of Transport Properties

Neutron transport properties of nuclear-irradiated concrete can be affected by many parameters, especially the microcracks in concrete. For a section of a concrete biological wall shown in Figure 4-3 (a), initially, it can be treated as a wall made of intact concrete material. Therefore, the neutron transport properties are usually constant (the initial values of new concrete). As a result, the neutron flux profile in the biological shielding wall may be considered as unchanged with time once the boundary conditions are determined. However, the neutrons and elevated temperatures in the concrete can lead to degradation of the concrete material, as shown in Figure 4-3 (b). The degradation is mainly due to the expansion of aggregate as well as the shrinkage of cement paste, as described in Chapter 2. This kind of volumetric mismatch can lead to microcracking at the aggregate-cement paste interface which can result in crack networks in the concrete.

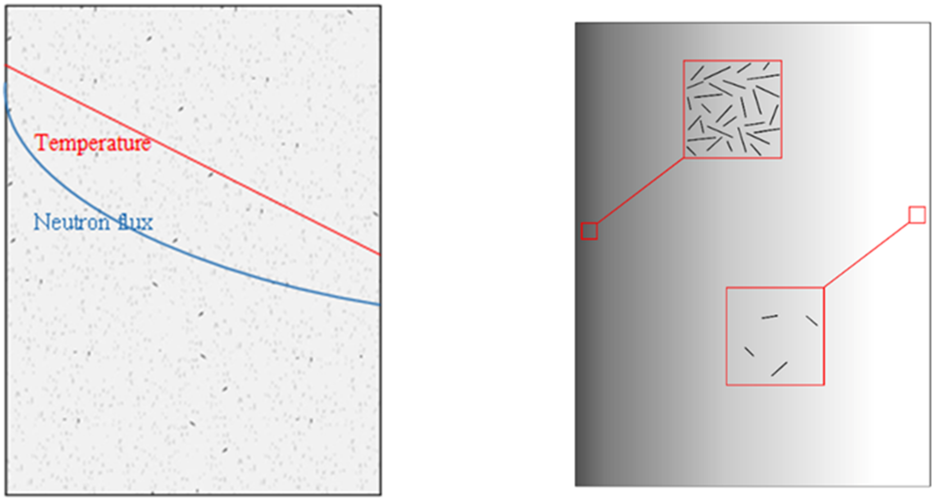

(a) (b)

Figure 4-3 (a) Intact concrete, (b) distressed concrete and its damage mechanism under neutron irradiation

The neutrons are attenuated by the interactions with the nuclei of atoms in the concrete. Therefore, the density of atoms has significant effects on the neutron shielding capacity of the material. The space generated by the microcracks provides an easy pathway for the neutrons because the dimensions of the microcracks are much larger than the space between atoms. So, the neutron macroscopic cross section (describing the probability per unit path length that a neutron will undergo an interaction) in the distressed concrete will decrease. Besides, elevated temperature also has an influence on the neutron macroscopic cross section calculation. The densities of constituent phases in the concrete are reduced by the crack propagation, volume expansion of the concrete, and dehydration of the cement paste. They all have an impact on the neutron macroscopic cross section calculation to a certain extent. As a result, the neutron diffusion coefficient (reciprocally correlated to the neutron macroscopic cross section) could increase, which means the neutron radiation level could be higher in the degraded concrete than in the intact concrete.

Two extreme cases can be used to further explain the effect of cracks on the attenuation capacity of the concrete wall. Figure 4-4 (a) shows that all cracks are formed perpendicular to the wall surface, which is the worst scenario in terms of neutron resistance; and Figure 4-4 (b) shows that all cracks are formed parallel to the wall surface, which is the best scenario. In the case of Figure 4-4 (a), the neutrons can go through the cracks with little resistance, so the attenuation capacity of the concrete wall is reduced considerably; and in the case of Figure 4-4 (b), the resistance of the wall may be reduced slightly by the cracks. In reality, the concrete distressed by neutron irradiation is somewhere between the two extreme cases. The crack network is more like that shown in Figure 4-3 (b).

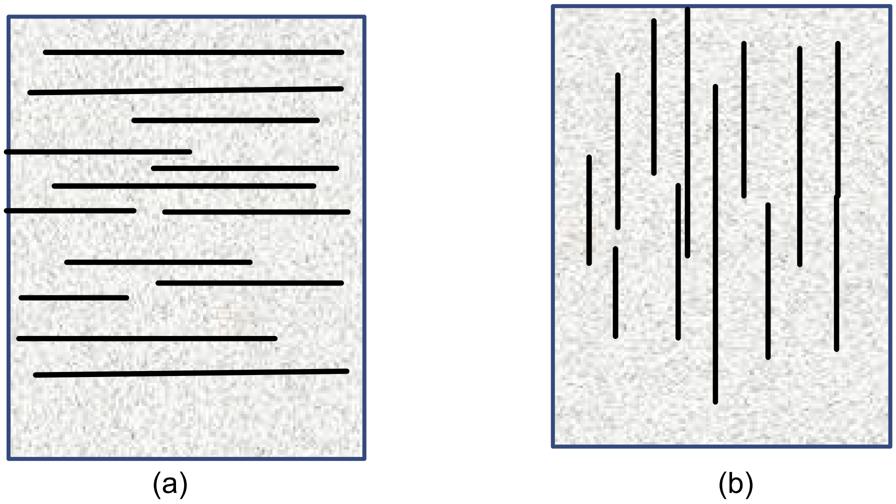

Figure 4-4 (a) All cracks are formed perpendicular to the wall surface; (b) all cracks are formed parallel to the wall surface

As shown in Figure 4-3 (a), the neutrons and temperature are not uniformly distributed inside the concrete wall. Since the extent of neutron-induced aggregate expansion highly depends on the radiation intensity and exposure time, the concrete material closer to the inner surface of the wall will show more severe damage (e.g., more cracks) than the concrete closer to the outer surface of the wall, and thus, the concrete wall cannot be simply treated as a homogeneous material. As discussed above, the neutron diffusion coefficient can be affected by the damage in the concrete, and the level of damage depends on the neutron level, which is a function of the position in the wall. So, the neutron diffusion coefficient depends on the position in the wall and time. The variation of neutron flux profiles in the distressed concrete will be more significant than the variation in intact concrete, especially for the concrete in the immediate vicinity of the inner surface of the wall, which is closer to the source of irradiation. Since the radiation time of a biological shield wall is very long, the potential increase of the neutron flux in that area will lead to more local damage, which could be important in the structural analysis. Therefore, it is important to take into account the effect of damage to the neutron transport properties of concrete.

Similarly, the thermal field in concrete could also be affected by the internal damage, and thus, the thermal transport properties cannot be treated as constants, as well. Unlike the neutron transport in distressed concrete, the process of heat conduction will be slowed down by the damage; this is because cracks in the distressed phase are filled by air whose thermal conductivity is much lower than that of concrete.

Our literature search showed that no research about the degradation of neutron and heat transport properties of concrete (i.e., $\mathcal{D}_1$, $\mathcal{D}_2$, and k) under neutron radiation and elevated temperature is available. In short, there is no test data available about the effect of concrete damage on neutron transport properties. However, as discussed in Chapter 2, there are many experimental data and theoretical studies for the mechanical properties of neutron-irradiated and -heated concrete in the literature, so a cross-property correlation theory can be used to calculate the variation of transport properties of concrete based on the variation of mechanical properties, taking into account the damage induced by nuclear irradiation.

4.2.1 Cross-property Correlation for Distressed Materials

The cross-property correlations for distressed materials were developed based on both composite mechanics and damage mechanics for two-phase composite materials (Eskandari-Ghadi et al. 2014). The theory can provide a link between two different categories of material properties. In this case, it provides the correlation between mechanical properties of distressed concrete and its transport properties. Various composite models can be used in the cross-property correlation theory. In this study, the GSC model as discussed in Chapter 2 was used. The configuration of the GSC model is shown in Figure 2-3.

Based on Equation (2-2) for the GSC model, the effective bulk modulus can be written in terms of the bulk and shear moduli of the inclusion and matrix

$$\frac{K_{eff}}{K_M} = 1 + \frac{d\left(\frac{K_I}{K_M} - 1\right)}{1 + (1-d)\frac{\frac{K_I}{K_M} - 1}{1 + \frac{4}{3}\frac{G_M}{K_M}}} \qquad (4\text{-}8)$$

where *K* with different subscripts are bulk moduli of different phases and *d* is the volume fraction of the inclusion; and subscripts *I*, *M*, and *eff* represent inclusion, matrix, and effective media, respectively. As shown in Chapter 2, the GSC model can also be applied to estimate the stiffness of distressed materials, and the theory is called *composite damage mechanics* (Eskandari-Ghadi et al. 2013; Xi et al. 2006).

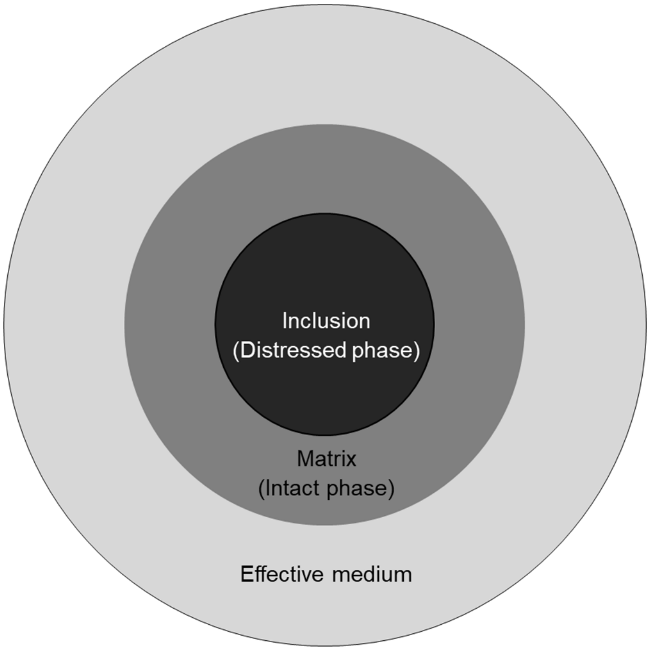

Figure 4-5 Composite damage mechanics model

In this case, as shown in**Error! Reference source not found.**, the inclusion is the distressed phase and the matrix is the intact phase. The distressed phase has a smaller stiffness than the intact phase. The distressed material is treated as a two-phase composite material, and thus the effective stiffness of the composite (the distressed concrete) must be between the two values: when $d = 0$, $K_{eff} = K_M$ (no damage), and when $d = 1$, $K_{eff} = K_I$ (fully damaged). The volume fraction of the inclusion, d, is the variable parameter which describes the development of internal damage in the material and can be derived from Eq. **Error! Reference source not found.**

$$d = \frac{\left(1 - \frac{K_{eff}}{K_M}\right)\left(4\frac{G_M}{K_M} + 3\frac{K_I}{K_M}\right)}{\left(3\frac{K_{eff}}{K_M} + 4\frac{G_M}{K_M}\right)\left(1 - \frac{K_I}{K_M}\right)} \tag{4-9}$$

As shown in Appendix A.1, $\frac{K_I}{K_M}$, and $\frac{G_M}{K_M}$ can all be expressed in terms of $\frac{E_I}{E_M}, \upsilon_\mathrm{I}, \upsilon_\mathrm{M}$. The internal damage of the material reduces the stiffness of the distressed phase, thus, $0 \le d \le 1, 0 < \frac{E_I}{E_M} \le 1, 0 < \frac{K_{eff}}{K_M} \le 1$.

By using the above equation, the damage in a material can be characterized based on its known mechanical performance. In order to model the transport problem in a distressed media, expressions of transport properties need to be obtained first. For the heat conduction problem, the equation for effective thermal conductivity based on the same GSC model has already been derived, see Section 9.2 from page 316 to page 319 in Christensen (2005).

$$k_{eff} = k_M \left(1 + \frac{d}{\frac{1-d}{3} + \frac{1}{\frac{k_I}{k_M} - 1}} \right) \tag{4-10}$$

Then, substitute Eq. **Error! Reference source not found.** in to Eq. **Error! Reference source not found.**

$$\begin{aligned} k_{eff} &= k_M \left(1 + \frac{\frac{\left(1 - \frac{K_{eff}}{K_M}\right)\left(4\frac{3(1-2\upsilon_\mathrm{M})}{2(1+\upsilon_\mathrm{M})} + 3\frac{E_I}{E_M}\frac{1-2\upsilon_M}{1-2\upsilon_I}\right)}{\left(3\frac{K_{eff}}{K_M} + 4\frac{3(1-2\upsilon_\mathrm{M})}{2(1+\upsilon_\mathrm{M})}\right)\left(1 - \frac{E_I}{E_M}\frac{1-2\upsilon_M}{1-2\upsilon_I}\right)}}{\frac{1 - \frac{\left(1 - \frac{K_{eff}}{K_M}\right)\left(4\frac{3(1-2\upsilon_\mathrm{M})}{2(1+\upsilon_\mathrm{M})} + 3\frac{E_I}{E_M}\frac{1-2\upsilon_M}{1-2\upsilon_I}\right)}{\left(3\frac{K_{eff}}{K_M} + 4\frac{3(1-2\upsilon_\mathrm{M})}{2(1+\upsilon_\mathrm{M})}\right)\left(1 - \frac{E_I}{E_M}\frac{1-2\upsilon_M}{1-2\upsilon_I}\right)}}{3} + \frac{1}{\frac{k_I}{k_M} - 1}} \right) \\ &= f_k\left(k_M, \frac{E_I}{E_M}, \frac{k_I}{k_M}, \frac{K_{eff}}{K_M}, \upsilon_\mathrm{I}, \upsilon_\mathrm{M}\right) \end{aligned} \tag{4-11}$$

The distressed phase has a higher porosity such as voids and cracks developed during the damage process. More importantly, the voids and cracks are barriers to the heat conduction in the solid frame because the thermal conductivity of air in the voids and cracks is lower than that of the solid, so the thermal conductivity of distressed concrete should be lower than the intact phase's ($0 < \frac{k_I}{k_M} \leq 1$).

For the effective neutron diffusion coefficient, we can observe the mathematical similarity between the governing equation for the one-speed neutron diffusion and the one-dimensional heat conduction equation, that is the similarity between Equation (4-2) and Equation (4-6). Since the GSC model was derived based on the heat conduction equation for a two-phase composite, the same GSC model can also be used to characterize the effective neutron diffusion coefficient of the two-phase composite (the two phases are damaged and intact phase). Therefore, the formulation of the effective neutron diffusion coefficient with damage shares the same form of Eq. **Error! Reference source not found.**, then

$$\mathcal{D}_{eff} = f_{\mathcal{D}}\left(\mathcal{D}_M, \frac{E_I}{E_M}, \frac{\mathcal{D}_I}{\mathcal{D}_M}, \frac{K_{eff}}{K_M}, \upsilon_\mathrm{I}, \upsilon_\mathrm{M}\right) \tag{4-12}$$

Since the damage in the material provides more accessible pathways for neutron transport, the diffusion coefficient of the distressed phase should be higher than that of the intact phase ($\frac{\mathcal{D}_I}{\mathcal{D}_M} \geq 1$). From the right hand sides of Equation **Error! Reference source not found.** and Equation **Error! Reference source not found.**, one can see that when we know the elastic modulus of distressed concrete at a given damage level, we will be able to calculate the effective thermal conductivity and neutron diffusion coefficient of the concrete at the same damage level. All other parameters involved in the two equations are the initial values of the intact phases.

The application of the method developed above for distressed materials requires that the damage evolution in the material is a random nucleation process. Since neutron radiation and high temperature-induced damage in concrete material fulfills this requirement, the method is capable of calculating the variations of neutron and heat transport properties of concrete by analyzing degradation of the elastic modulus of concrete under neutron radiation and heat which has been investigated by many experimental and theoretical studies (Biwer et al. 2020).

4.2.2 Degradation of Mechanical Properties

When evaluating the neutron radiation-induced degradation, only the fast neutron effect is considered. For including damage due to thermal neutrons, a similar method can be used.

The effect of damage on the mechanical properties of concrete can be represented by the ratio of the bulk moduli with damage and without damage, $\frac{K_{eff}}{K_M}$, which can be obtained using the approach described in Chapter 2. The inclusion is the distressed phase and the matrix is the intact phase, thus $E_M = E_0, E_I = E_d,\ k_M = k_0, k_I = k_d,\ \mathcal{D}_M = \mathcal{D}_0, \mathcal{D}_I = \mathcal{D}_d, \frac{E_I}{E_M} = \frac{E_d}{E_0}, \frac{k_I}{k_M} = \frac{k_d}{k_0}, \frac{\mathcal{D}_I}{\mathcal{D}_M} = \frac{\mathcal{D}_d}{\mathcal{D}_0}$ which are constant values for the intact concrete. It is usually assumed that the Poisson's ratios don't change during the damage process: $v_M = v_I = v_0$(due to the lack of test data). Then, the effective thermal conductivity and effective neutron diffusion coefficient can be determined by Equation **Error! Reference source not found.** and Equation **Error! Reference source not found.** as functions of time, fast neutron flux, and temperature:

$$k_{eff} = f_k\left(k_0, v_0, \frac{E_d}{E_0}, \frac{k_d}{k_0}, \int_0^t \phi_1 dt\, , T\right), \mathcal{D}_{eff} = f_{\mathcal{D}}\left(\mathcal{D}_0, v_0, \frac{E_d}{E_0}, \frac{\mathcal{D}_d}{\mathcal{D}_0}, \int_0^t \phi_1 dt\, , T\right) \qquad (4\text{-}13)$$

It should be mentioned that in the future, if experimental data are available, the measured transport properties should be used. The data can be obtained from laboratory study or from harvesting samples from existing concrete in power plants.

4.2.3 Other Parameters

In addition to k and $\mathcal{D}_i$, other parameters in Equation (4-4), Equation (4-5), and Equation (4-6), including v_i, Σ_a, Σ_c, c_p, and ρ, may potentially be affected by the neutron radiation and temperature.

Generally, neutron speed indicates a neutron's kinetic energy and is temperature-dependent. For example, v_T, the most probable velocity of thermal neutrons at temperature T, can be calculated based on v_0, which is the most probable velocity at room temperature T_0: $v_T = v_0\sqrt{\frac{T}{T_0}}$ (DOE Fundamentals Handbook 1993). The temperature used here is the absolute temperature of the media. Since the temperature considered for a concrete biological shield is not in a high temperature range, the variation of v_i caused by temperature rise is not significant. Thus, the neutron speed v_i can be assumed to be unchanged during the neutron radiation process.

The neutron macroscopic cross section (Σ) of a medium is derived from the atomic number density and neutron microscopic cross section of each element in it (Duderstadt and Hamilton 1976), and both of them can be influenced by radiation and temperature. For instance, loss of hydrogen and oxide due to the dehydration in concrete under high temperature (more than 100 ºC) will lead to the change of atomic number density of these two elements. The neutron microscopic cross section is also temperature-dependent (DOE Fundamentals Handbook 1993). Such kinds of material inhomogeneity (non-uniform distribution of elements) and its variation over time will make the determination of the neutron macroscopic cross section of a heterogeneous material like concrete quite complicated. Since this is not the major task in this work, all of the neutron macroscopic cross sections encountered in this work are considered to be constants for now. To obtain the accurate neutron cross sections of concrete with time, detailed experimental studies or theoretical modeling is needed.

The specific heat capacity of concrete will vary with temperature (Kodur and Sultan 2003; Pan et al. 2016), but there is no research about the effects of nuclear radiation on it. Actually, for the composite material with two phases, the effective specific heat capacity can be determined based on the temperature and the two phases' specific heat capacities, coefficients of thermal expansion, and bulk moduli (Rosen and Hashin 1970). Again, the temperature considered for the concrete biological shield is not in a high-temperature range, so the specific heat capacity is assumed to be a constant in the present study.

Mass density is the ratio of mass to volume. It has been confirmed that concrete expands under neutron radiation. The volumetric change of concrete under neutron irradiation mainly results from a combination of the expansion of aggregates, the shrinkage of cement paste, and the thermal expansion of these two phases, as shown in Chapter 2. The model developed in Chapter 2 can be used to predict the volume change of concrete under neutron radiation. Experimental data (Biwer et al. 2020) showed that weight loss is about 5% or less for concrete samples under neutron radiation and high temperature (up to 400 ºC). The weight loss appears to correlate with changes in temperature rather than neutron fluence. No clear trend was observed. Weight loss induced by both neutron radiation and temperature rise is very likely mainly due to the dehydration of the cement paste. A constant 2% weight loss can be assumed in the calculation.

4.3 Numerical Analyses

4.3.1 Coupled Neutron Radio-Thermo Analysis

As discussed in the previous sections, v, Σ_a, Σ_c, and c_p are considered as constants, and k, ρ, and $\mathcal{D}_i$ are time- and position-dependent parameters. Coupled radio-thermo analysis of fast neutron, thermal neutron, and thermal fields within neutron-irradiated concrete can be performed based on the two-group neutron diffusion model and the heat conduction equation. The effects of neutron radiation-induced degradation and thermal deterioration on concrete can be taken into account. The three governing equations are

$$\frac{1}{v_1}\frac{\partial \phi_1(x,t)}{\partial t} - \nabla \cdot \mathcal{D}_1(x,t)\nabla \phi_1(x,t) + \Sigma_{R1}\phi_1(x,t) = 0 \tag{4-14}$$

$$\frac{1}{v_2}\frac{\partial \phi_2(x,t)}{\partial t} - \nabla \cdot \mathcal{D}_2(x,t)\nabla \phi_2(x,t) + \Sigma_{a2}\phi_2(x,t) = \Sigma_{s12}\phi_1(x,t) \tag{4-15}$$

$$c_p \rho(x,t) \frac{\partial T(x,t)}{\partial t} = \nabla \cdot k(x,t) \nabla T(x,t) + 1.6 \times 10^{-13} \Sigma_c \mathcal{E}_b \phi_2(x,t) \tag{4-16}$$

The analytical solutions of these coupled nonlinear transient equations are too complex to be obtained. Instead, an implicit finite difference approach was adopted to solve the problem, as shown in Appendix A.6 . Initial conditions, boundary conditions, and time step are shown in the next section as a case study. The calculation flowchart is shown in Figure 4-1. First, based on the conditions and properties of the material from the previous time step, neutron and heat transport properties are obtained. Then, coupled radio-thermo analysis is performed to obtain the irradiation field and thermal field. Based on the current neutron fluence and temperature, the damage of the material is obtained through the multiphase and multiscale model in Chapter 2. After that, cross-property correlation is used to estimate the variation of transport properties using the variation in mechanical properties, and the radio-thermo analysis is performed again to update the irradiation field and thermal field. This process will go on until the irradiation field and thermal field do not change significantly within the time step (satisfying the allowable error limit). The bisection method was used for root-finding iteration in each time step, and the speed of convergence is satisfactory.

4.3.2 Input Parameters

All input parameters needed are listed in

Table 2-3 and Table 4-1.

Table 4-1 Input parameters

Neutrons	Concrete
• Neutron source (boundary conditions) • Neutron speed (v_1 and v_2)	• Density (ρ) • Neutron diffusion coefficients ($\mathcal{D}_1$ and $\mathcal{D}_2$) • Curing time, *t* • Neutron cross sections (Σ_c, Σ_{R1}, Σs_{12}, and Σ_{a2}) • Specific heat capacity (c_p) • Thermal conductivity (k) • $\frac{E_d}{E_0}$, $\frac{k_d}{k_0}$, $\frac{\mathcal{D}_d}{\mathcal{D}_0}$

4.3.3 A Case Study

As mentioned at the beginning of Chapter 2, the present models are developed with the intent of application to reinforced concrete structures used in NPPs. Our focus is the models for concrete used in reinforced concrete structures. As a case study, a concrete biological shielding wall, without rebar embedment, shown Figure 4-6, is used to show the capability of the model and the basic trends of the temperature and neutron flux profiles in a concrete wall by considering the effect of damage. The thickness of the wall is 80 cm. It was assumed that the fast and thermal neutron flux and temperature are uniformly distributed on the inner (left) surface of the wall. Thus, the neutron and heat conduction can be considered to be a one-dimensional problem along the depth of the concrete wall. The outer (right) surface of the wall is exposed to the ambient environment. The fast and thermal neutron distribution as well as temperature field in a concrete biological shield during 80 years of operation are obtained by the present model with and without the effect of damage due to fast neutrons and elevated temperature.

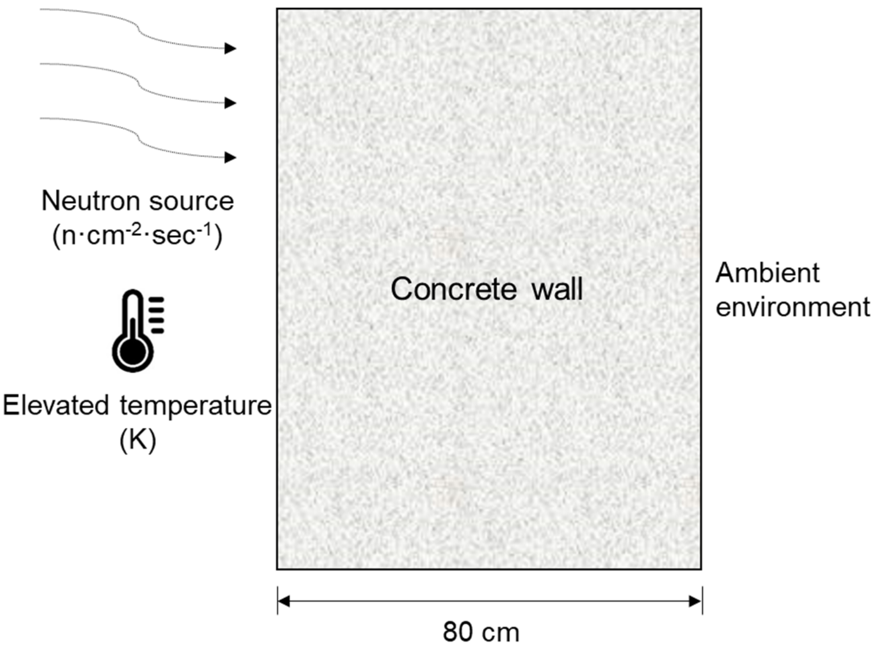

Figure 4-6 The configuration of the concrete wall for numerical analysis

A constant neutron flux density of 3.2×10^{10} n/(cm^2·sec) was assumed at the inner surface of the wall for fast neutrons with a 0.1 MeV energy level, and a neutron flux density of 4×10^{10} n/(cm^2·sec) was assumed for thermal neutrons with up to 0.0253 eV energy level. The neutron flux at the outer surface of the wall was approximately 10^{-3} of the neutron flux at the inner surface (Esselman and Bruck 2013). The temperature was 65 ºC at the inner surface and 20 ºC at the outer surface. Ordinary concrete 02-a from REACTOR PHYSICS CONSTANTS (1963) and Hogerton and Grass (1953) was used, since major parameters for the concrete were provided. The water-cement ratio assumed in Hogerton and Grass (1953) was over 0.8, which is not reasonable for concrete found at NPPs, so their water-cement ratio was not used here. The mix proportion by weight was assumed for an ordinary concrete: water/cement/aggregate = 0.4/1/4.99. The expansion of aggregate particles under neutron radiation was assumed to be Profile 1 shown in Figure 2-20. The expansion of aggregate particles under neutron radiation was assumed to be Profile 1, shown in Figure 2-20. It was also assumed that $\frac{E_d}{E_0}$ = 1/3, $\frac{k_d}{k_0}$ = 1/10, $\frac{D_{1d}}{D_{10}}$ = 10, and $\frac{D_{2d}}{D_{20}}$ = 10. The assumed values are to illustrate the sensitivity of the parameters to degradation and maintain the changes of the transport properties within one order of magnitude. The actual changes could be smaller or larger depending on the level of damage in the concrete. All other parameters of the concrete are listed in

Table 4-2.

Figure 4-7 through Figure 4-15 show the results of the numerical analysis. Figure 4-7 shows the variation of the damage parameter, *d*, which can be calculated from Equation **Error! Reference source not found.**; and *d* = 0 means no damage and *d* = 1 means complete damage. The profiles of the damage parameter, *d*, of the concrete up to 80 years are reported in Figure 4-7 (a). Damage of the concrete due to neutron radiation and the temperature continues to develop with increasing time, especially for the concrete close to the neutron source (at small depths in the wall). The concrete far away from the neutron source has smaller damage. As one can see from Figure 4-7 (b), near the surface, the damage of concrete increases with time; and deeper in the wall, the damage of concrete shows little variation with increasing time even up to 80 years.

Table 4-2 Parameters used in the ordinary concrete numerical analysis

Parameters	Values	Reference
Concrete		
$\mathcal{D}_1$ [cm]	1.14	(REACTOR PHYSICS CONSTANTS 1963)
$\mathcal{D}_2$ [cm]	0.484	(REACTOR PHYSICS CONSTANTS 1963)
Σ_{R1} [cm^{-1}]	0.085	(REACTOR PHYSICS CONSTANTS 1963)
Σs_{12} [cm^{-1}]	0.08*	–
Σ_{a2} [cm^{-1}]	0.0094	(REACTOR PHYSICS CONSTANTS 1963)
v_1 [cm/sec]	4.37×10^{8}†	–
v_2 [cm/sec]	2.2×10^{5}†	–
c_p [J/(kg·K)]	650	(Ursu 1985)
ρ [kg/cm^3]	2.3×10^{-3}	(REACTOR PHYSICS CONSTANTS 1963)
k [W/(cm·K)]	8.7×10^{-3}	(Ursu 1985)
Σ_c [cm^{-1}]	0.0094‡	–
E_b [MeV]	5.5	(Price et al. 1957)
Curing time [days]	28	-
Cement paste		
Chemical composition [mass%]	C=0.654, S=0.2078, A=0.0498,F=0.0246*	-
ρ_c [kg/cm^3]	3.14×10^{-3}	-
f_{cc}' [MPa]	65*	-
f_{ct} [MPa]	4*	-
Drying shrinkage (%)	-0.05*	-
Others	Table 2-1 and Table 2-2	-
Aggregates		
ρ_{agg} [kg/cm^3]	2.55×10^{-3}	(Kelly et al. 1969)
E_{agg} [GPa]	72.4	(Kelly et al. 1969)
υ_{agg}	0.28*	-
α_{agg}^{T} [10^{-5} / ºC]	6.35§	(Kelly et al. 1969)

* Assumed typical value.

† Calculated based on classical kinetic energy equation for 0.1 MeV and 0.0253 eV neutrons.

‡ Use the value of Σa2 as an approximation.
§ 20-120 ºC.

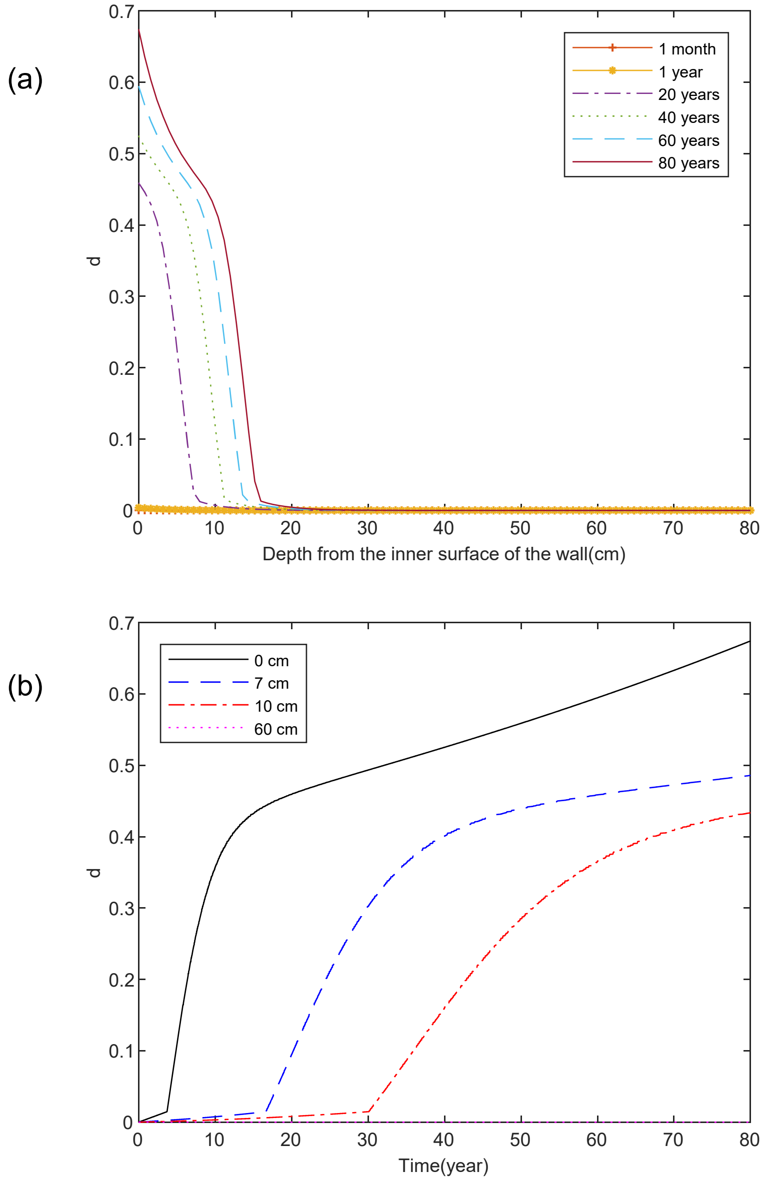

Figure 4-7 Damage progression due to neutron radiation and the temperature: (a) with the depth of concrete at different times; (b) with time at different depths

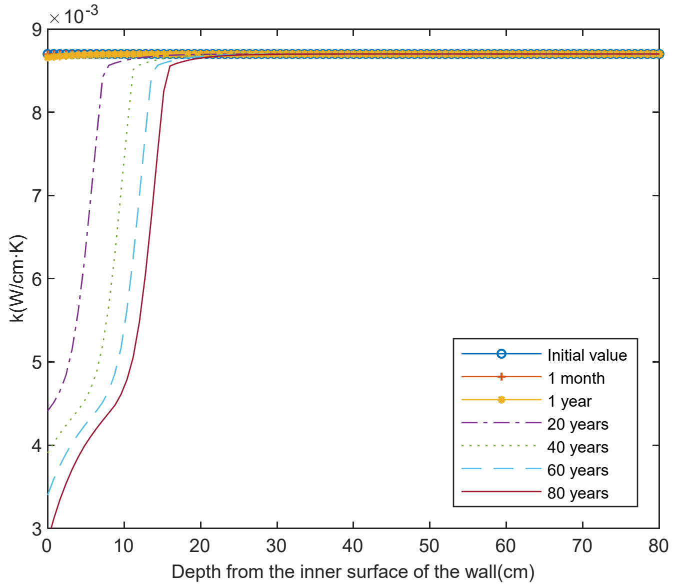

Figure 4-8 Thermal conductivity profiles along the depth at different times

The effect of damage induced by the temperature and neutron radiation was studied from two aspects. One is the impact on temperature profiles, and the other is the impact on neutron flux profiles.

The impact on temperature profiles

The effect of damage induced by the temperature and neutron radiation on thermal conductivity of concrete, *k*, is shown in Figure 4-8. This figure shows important results of the model. At a fixed depth, say 5 cm, the value of *k* gradually decreases with time, which is shown by different types of lines. At different depths, say 5 cm and 10 cm, the concrete closer to the neutron source (5 cm) shows a larger decrease of *k* than the concrete deeper inside the wall (10 cm) since the damage in the locations closer to the neutron source is more significant.

Figure 4-9 shows the temperature profiles in the concrete with and without the effects of damage induced by nuclear irradiation and temperature after 1 month, 40 years, and 80 years of exposure. If the damage is not considered, the temperature profile will not change over time after the steady-state temperature distribution is reached. As one can see from Figure 4-9 (b), which shows the differences of the curves in Figure 4-9 (a), the damage of radiation and temperature in concrete leads to minor changes of the temperature profile in the concrete (maximum change is less than 7 ºC). Since the radiation heating depends on thermal neutron flux and the thermal neutron flux increases over time, as one can see later on in Figure 4-14 (a), the temperature profile should have increased correspondingly. On the other hand, the damage induced by neutron radiation and elevated temperature can reduce the thermal conductivity of concrete, as shown in Figure 4-8, which can slow down the heat conduction process. As a result, the overall change of the temperature profile is not large.

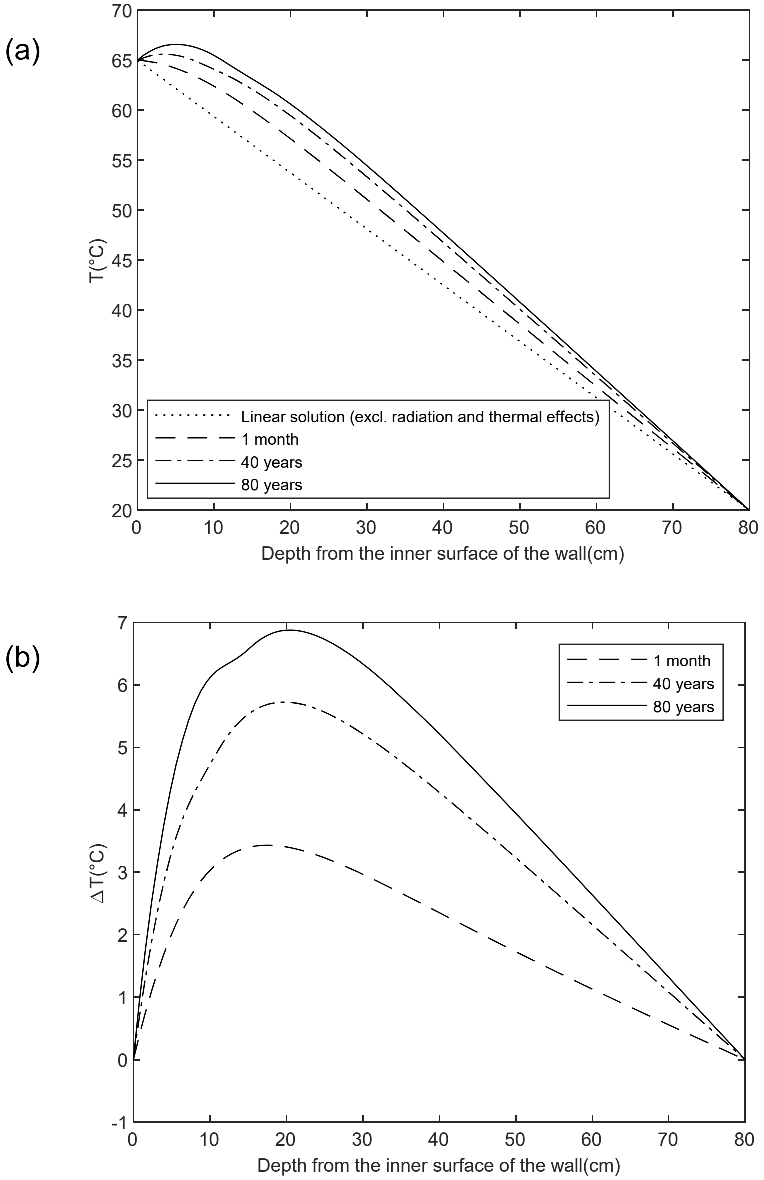

Figure 4-9 Temperature profiles along the concrete depth: (a) absolute values without radiation and thermal effects considered, with these effects considered at 1 month, 40 years, 80 years; (b) temperature changes compared to the initial values

The impact on neutron flux profiles

The effect of damage induced by the temperature and neutron radiation on the transport properties will need to be shown first. The profiles of neutron diffusion coefficients, D_i, are shown in Figure 4-10 and Figure 4-11. The value of D_i gradually increases with time, and the change is quite large compared to its initial value. In the surface layer, the value of D_i is more than tripled. Similar to the behavior of thermal conductivity discussed earlier, D_i of the concrete close to the neutron source shows larger variation than D_i of the concrete deeper in the wall, and this is because the damage of concrete near the neutron source is more severe.

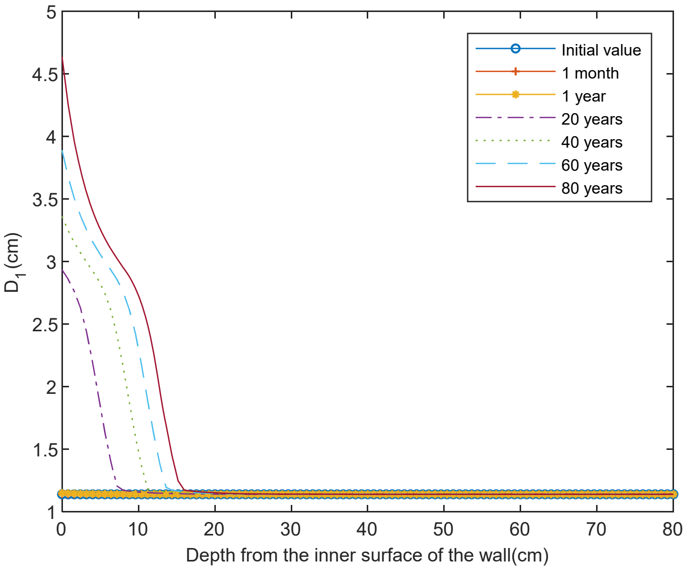

Figure 4-10 Fast neutron diffusion coefficient (D_1) profiles along the concrete depth at different times

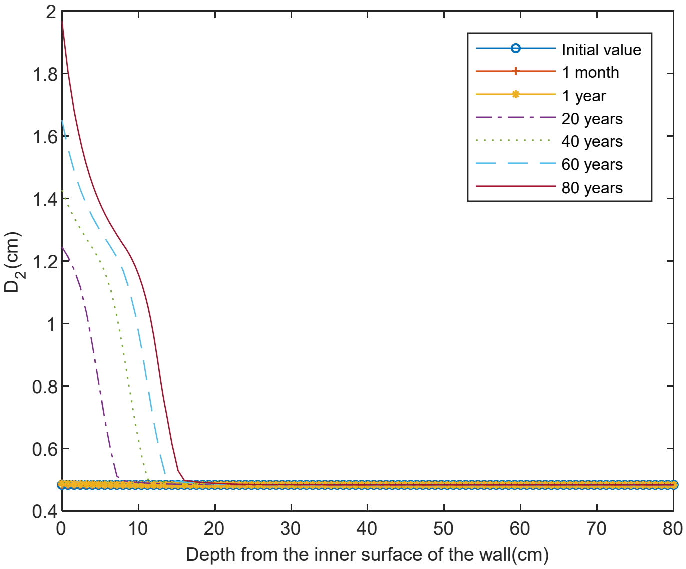

Figure 4-11 Thermal neutron diffusion coefficient (D_2) profiles along the concrete depth at different times

After the determination of the material parameters as functions of time and location (depth), the nonlinear solutions of the neutron flux profiles in the concrete up to 80 years were obtained, as shown in Figure 4-12 to Figure 4-15. The linear solutions in the figures are the solutions excluding the effect of damage, and the nonlinear solutions considered the effect of damage. The profiles are plotted in the figures, and the differences between the linear and nonlinear solutions at different times are also plotted in the figures. It is clearly shown that the damage induced by neutron radiation and elevated temperature can result in considerable degradation of concrete as a shielding material and also as a structural material, and thus, can lead to a large increase of fast and thermal neutron flux in concrete. Taking into account the damage, the neutron flux increases with time significantly, especially for the concrete near the radiation source. The peak of the increase occurs near the inner surface. This is mainly caused by the increase of the neutron diffusion coefficients of concrete, as shown in Figure 4-10 and Figure 4-11. Comparing Figure 4-12 (a) with Figure 4-14 (a), the profiles of thermal neutron flux are different from the profiles of fast neutrons. The thermal neutron flux ϕ_2 decreases at a slower rate than the fast neutron flux ϕ_1 along the depth of the wall. This result is due to the production of secondary thermal neutrons from the fast neutron group.

Since the damage of concrete mainly depends on the neutron fluence in the concrete, which can be obtained from the neutron fluxes, the fast and thermal neutron fluence profiles in the concrete wall at 60 years and 80 years are plotted in Figure 4-13 and Figure 4-15. Similar to the neutron flux profiles, considerable increases of neutron fluence from the linear solution without considering the damage effect are observed for the concrete near the radiation source.

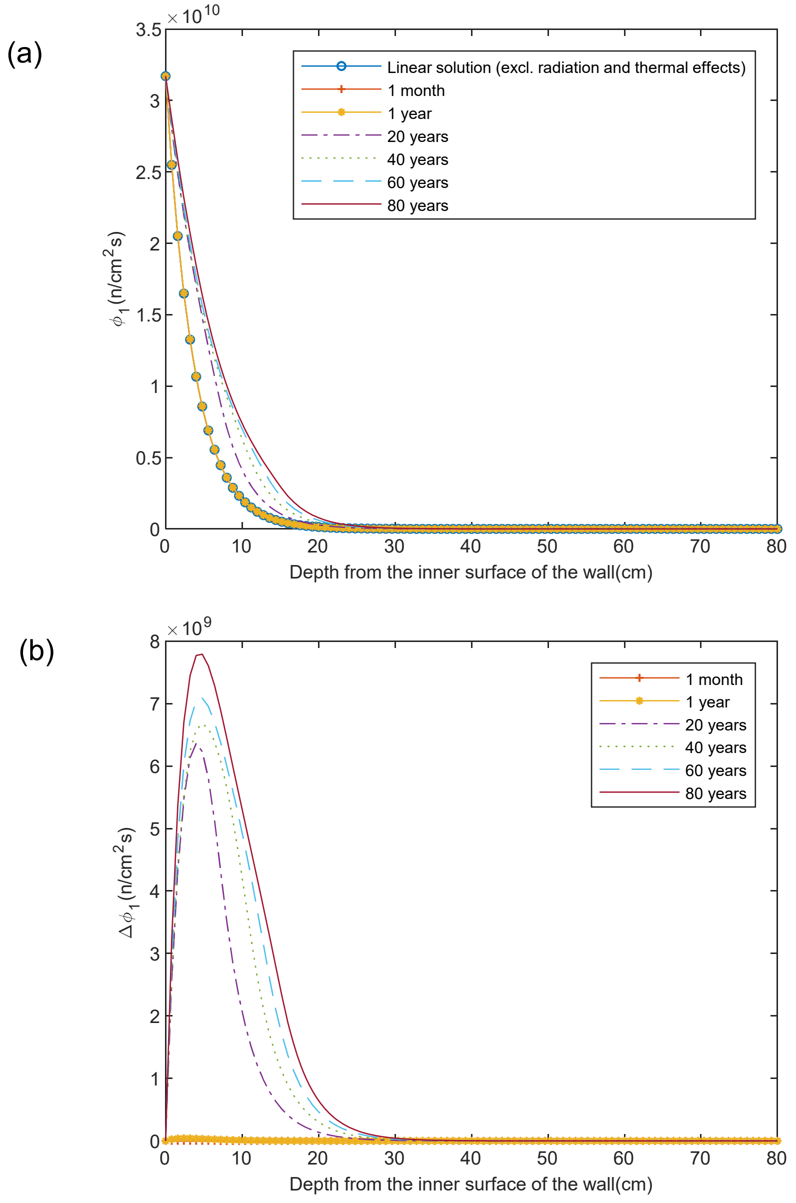

Figure 4-12 Fast neutron flux profiles along the concrete depth (energy > 0.1 MeV): (a) absolute values of fast neutron flux with and without the radiation and thermal effects after different periods of exposure; (b) neutron flux increases compared to the case without the radiation and thermal effects

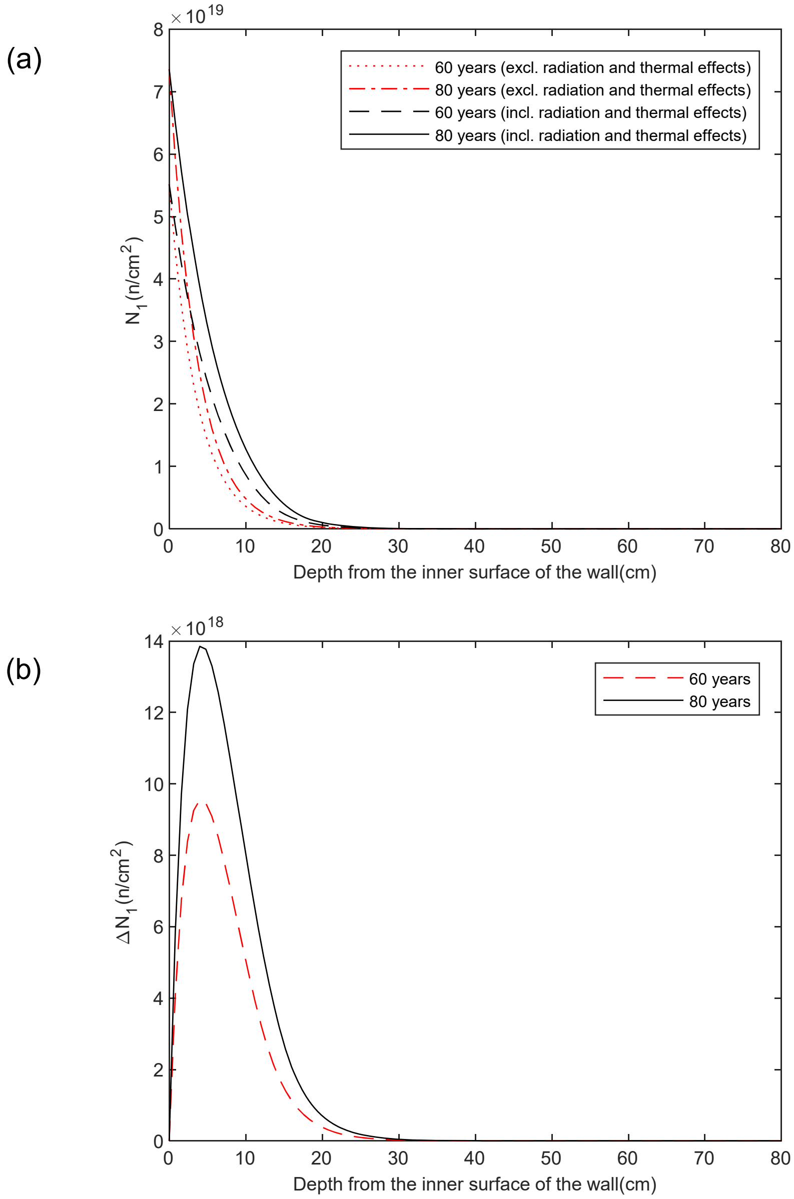

Figure 4-13 Fast neutron fluence profiles along the concrete depth at 60 years and 80 years (energy > 0.1 MeV): (a) absolute values of fast neutron fluence with and without considering the radiation and thermal effects; (b) neutron fluence increase compared to the case without these effects considered

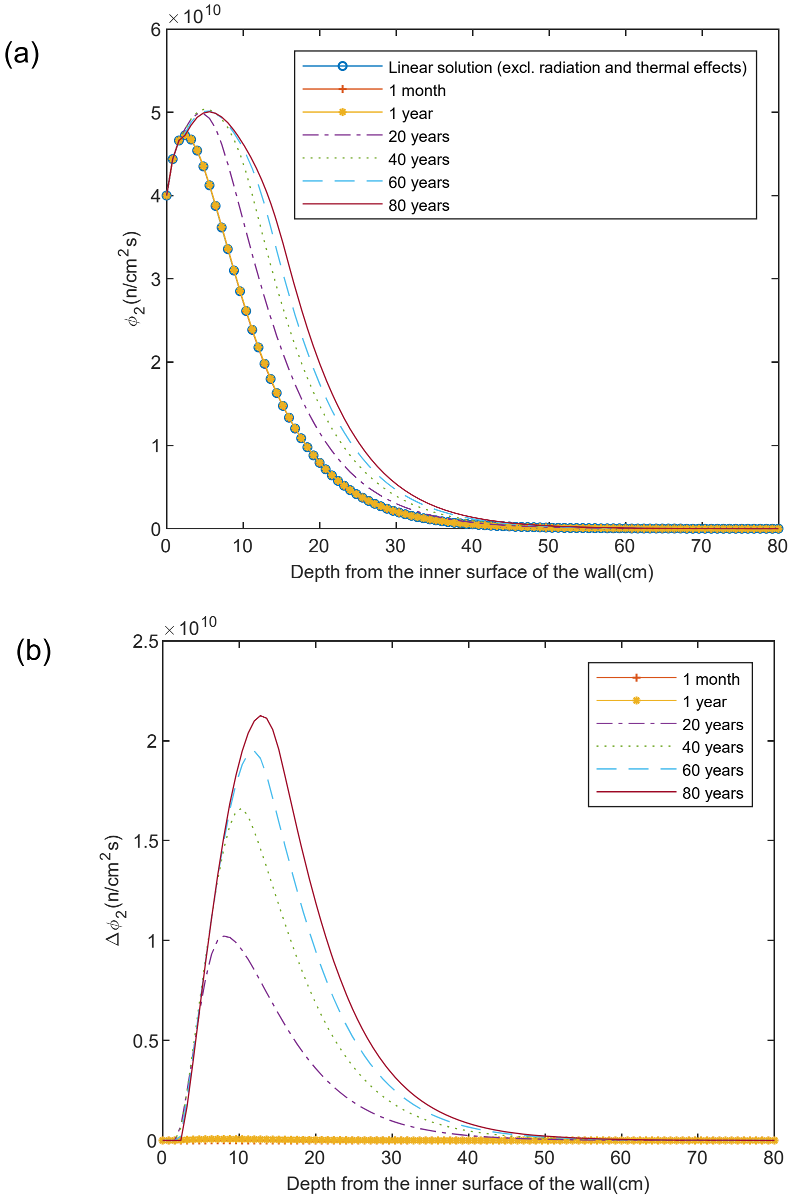

Figure 4-14 Thermal neutron flux profiles along the concrete depth (energy > 0.0253 MeV): (a) absolute values of thermal neutron flux with and without the radiation and thermal effects after different periods of exposure; (b) neutron flux increases compared to the case without the radiation and thermal effects

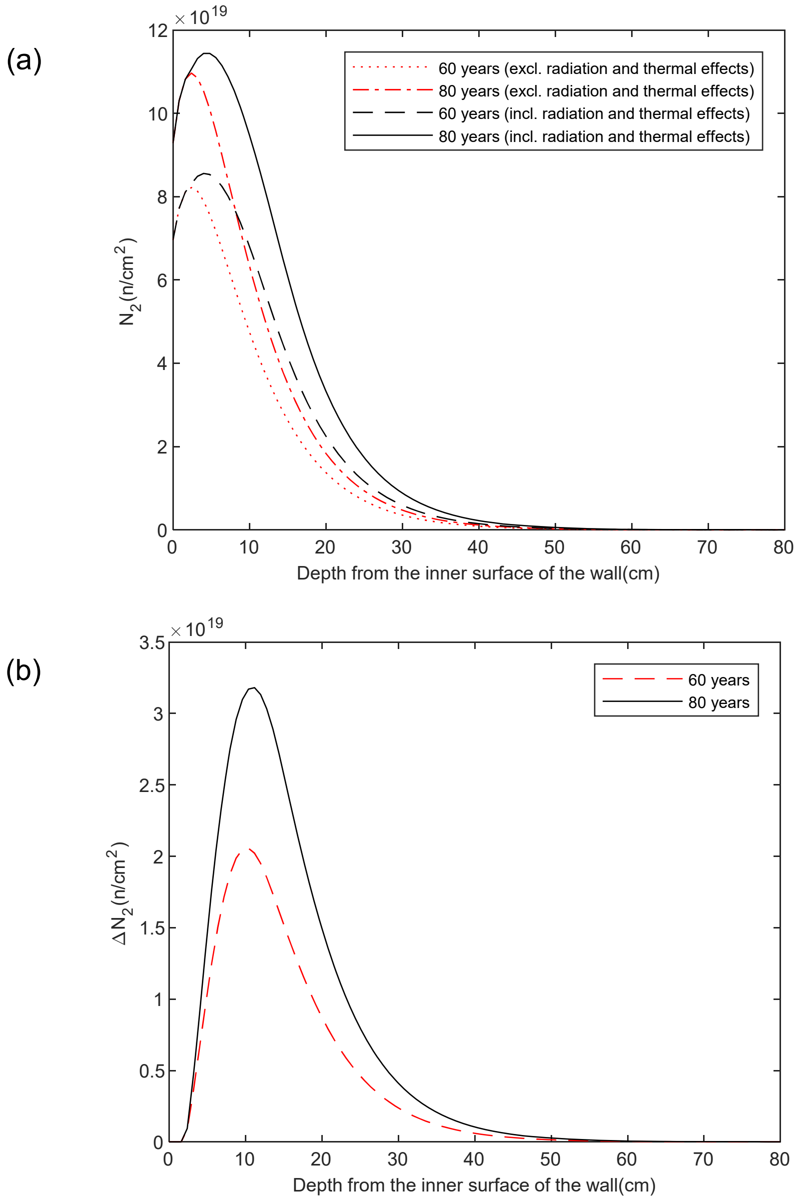

Figure 4-15 Thermal neutron fluence profiles along the concrete depth at 60 years and 80 years (energy > 0.0253 MeV): (a) absolute values of thermal neutron fluence with and without considering the radiation and thermal effects; (b) neutron fluence increase compared to the case without these effects considered

4.4 Summary

The multigroup neutron diffusion model was introduced to simplify the neutron transport equation and consider the neutron energy dependence more realistically. Based on one-dimensional two-group neutron diffusion equations and the heat conduction equation, the fast and thermal neutron fields as well as the thermal field in concrete can be solved. Since the mechanical properties of concrete can be degraded under nuclear radiation and elevated temperature, the neutron transport properties of concrete could be degraded, too. The potential variations of transport properties of distressed concrete were estimated by cross-property correlation theories, which can convert the variation in mechanical properties into the corresponding variation in transport properties of the material. The cross-property correlation theory was used together with the multiphase and multiscale model developed in Chapter 2 to estimate the change of neutron diffusion coefficients as well as the thermal conductivity of concrete due to neutron radiation and thermal effects. An ordinary concrete wall was analyzed up to 80 years of operation as a simplified example of a typical concrete biological shield in NPPs. The results show that the neutron diffusion coefficient of neutron-irradiated concrete gradually increases with time. Assuming that the concrete damage increases the neutron diffusion coefficient by a factor as large as 10 and decreases the thermal conductivity by a factor as small as 0.1, the concrete damage can result in a considerable increase of neutron flux in the concrete, and the neutron flux increases significantly with time, especially for the concrete near the radiation source.

5 LONG-TERM GAMMA RADIATION LEVELS IN DISTRESSED CONCRETE

Similar to the neutron irradiation transport problem, the damage of concrete can also change the gamma-ray transport properties of concrete. With degraded transport properties, the gamma-ray levels in a biological shielding wall will be different from those in the original concrete. Although the direct impact of gamma radiation on concrete is not considered, the radiation heating generated by gamma radiation could lead to additional damage of the concrete. In this chapter, the gamma-ray photon radiation levels in a concrete biological shielding wall will be predicted by taking into account the possible degradation of the transport properties induced by fast neutron radiation and elevated temperatures.

The calculation flowchart is shown in Figure 5-1. First, based on the conditions and properties of the material from the previous time step, neutron, photon, and heat transport properties are obtained. Then, coupled radio-thermo analysis is performed to obtain the irradiation field and thermal field at the same time. Based on the current fast neutron fluence and temperature, the damage of the material, which is *d* shown in Equation **Error! Reference source not found.**, is obtained through the multiphase and multiscale model in Chapter 2. After that, cross-property correlation is used to estimate the variation of transport properties using the variation in mechanical properties, and the radio-thermo analysis is performed again to update the radiation field and thermal field. This process will go on until the radiation field and thermal field do not change significantly within the time step (satisfying the allowable error limit). The new development in this chapter is the multigroup photon diffusion analysis as represented by the "Photon field" box in Figure 5-1.

5.1 Photon Transport and Heat Conduction

5.1.1 Photon Transport

Gamma-rays are photons that originate from nuclear transitions with photon energies typically above 100 keV. As discussed in the Phase 1 study (Biwer et al. 2020), gamma-ray photons interact with matter through three primary mechanisms: photoelectric effect, Compton scattering, and pair production. For the photoelectric effect, a photon is absorbed, resulting in the ejection of an orbital electron. For Compton scattering, the photon is not absorbed, but scattered with some energy lost, and an electron is also ejected. For the pair production, the photon is transformed, and a pair consisting of a positron and an electron is ejected. These three mechanisms predominate as a function of energy and atomic number of the transport medium, as shown in Figure 5-2. Based on the energy range of gamma-rays from nuclear reactors, which is from 100 KeV to 10 MeV, and the atomic numbers of elements usually found in concrete, Compton scattering is the dominant interaction mechanism for the gamma-rays in concrete biological shields (Kontani et al. 2014).

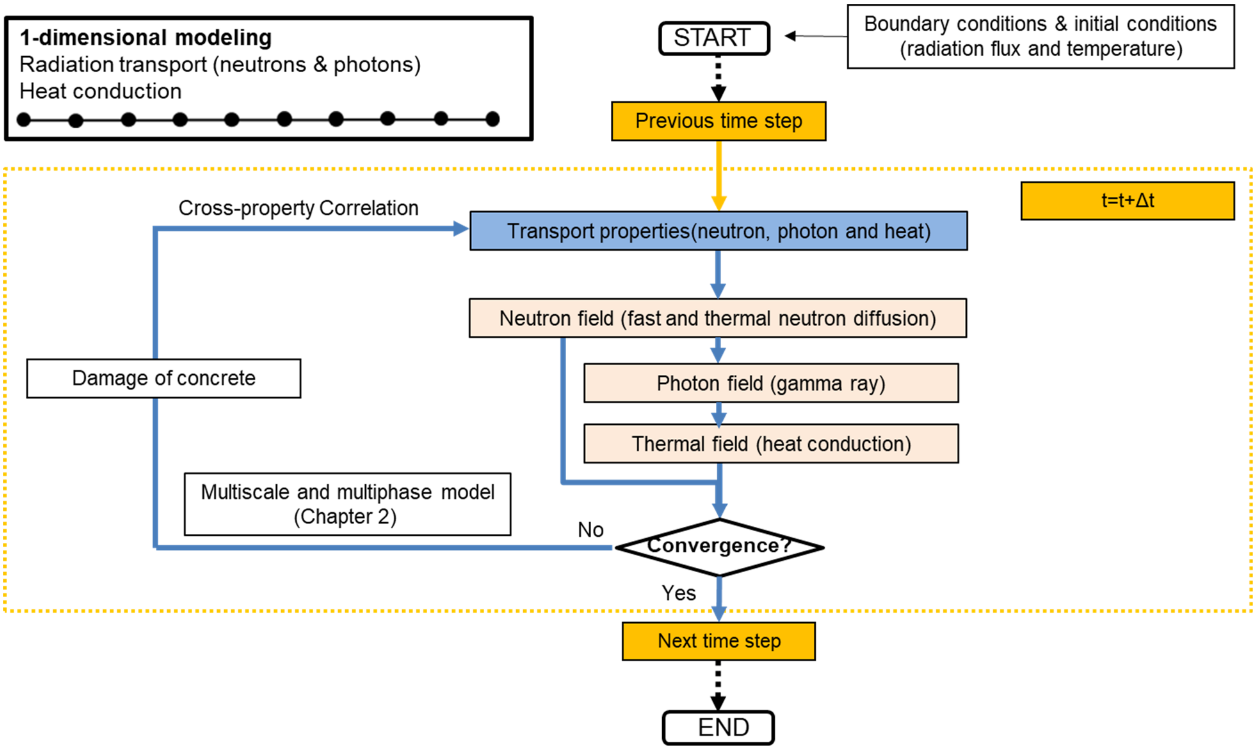

Figure 5-1 Calculation flowchart for photon diffusion and heat conduction

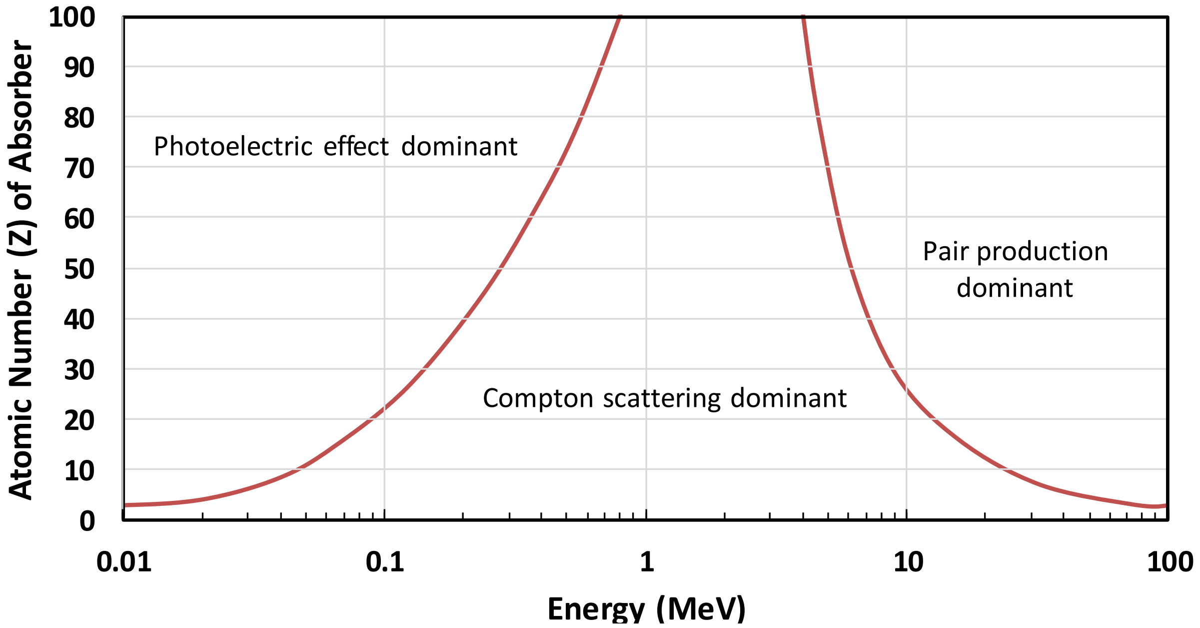

Figure 5-2 Relative importance of the three major interactions of gamma-ray radiation with matter (adapted from Evans 1955)

Both neutrons and photons are neutral particles. Gamma-ray photon transport in a medium can be described using the same form of transport equation shown in Equation **Error! Reference source not found.** for neutron transport. Since Compton scattering is dominant in concrete biological shields, and there are very few absorption events, the diffusion approximation used for neutron transport can still be used for gamma-ray photon transport in this study with different material parameters. The photon diffusion equation without considering energy variations and the one-speed neutron diffusion equation share the same form of governing equation:

$$\frac{1}{c}\frac{\partial\Phi(x,t)}{\partial t} - \boldsymbol{\nabla}\cdot\mathbb{D}(x,t)\boldsymbol{\nabla}\Phi(x,t) + \mu_a(x)\Phi(x,t) = \boldsymbol{S_\gamma}(x,t) \tag{5-1}$$

where Φ is the scalar photon flux in photons/(cm^2·sec); c is light speed in cm/sec; $\mathbb{D}$ is the photon diffusion coefficient in cm; μ_a is the photon absorption coefficient in cm^{-1}; $\boldsymbol{S_\gamma}$ is the internal source term in n/(cm^3·sec); and x and t are the position and time in cm and sec, respectively. Initial conditions and boundary conditions need to be used along with the above equation to obtain the solution of photon flux.

Similar to the multigroup neutron diffusion problem, the photon energy dependence can be handled by dividing the whole energy domain into a set of energy groups instead of treating the energy as a continuous variable. In practice, the group number could be 2 to 20 depending on the actual problem. For instance, two groups may be sufficient for a very simple survey calculation (like neutrons), and 20 groups could be used for problems that require fine details (Duderstadt and Hamilton 1976). The photons inside each group were assumed to behave as particles with the same energy, and the photon source in each group could include the secondary photons from scattering reactions of photons in the other photon groups with higher energy levels. There are two different methods for group structures with more than two groups: directly coupled and non-directly coupled. As shown in Figure 5-3, the direct coupling is achieved once a group-spacing is chosen that lets particles only scatter to the next group with lower energy; and the non-direct coupling means that particles could scatter to any group with lower energy, which is a more general case than the directly coupled method. Usually, no up-scattering is considered, which means a group with a lower energy does not scatter to a group with higher energy.

For the photon source in each group, secondary gamma-rays from neutron interactions should also be included which could be produced in neutron capture and inelastic scattering of neutrons.

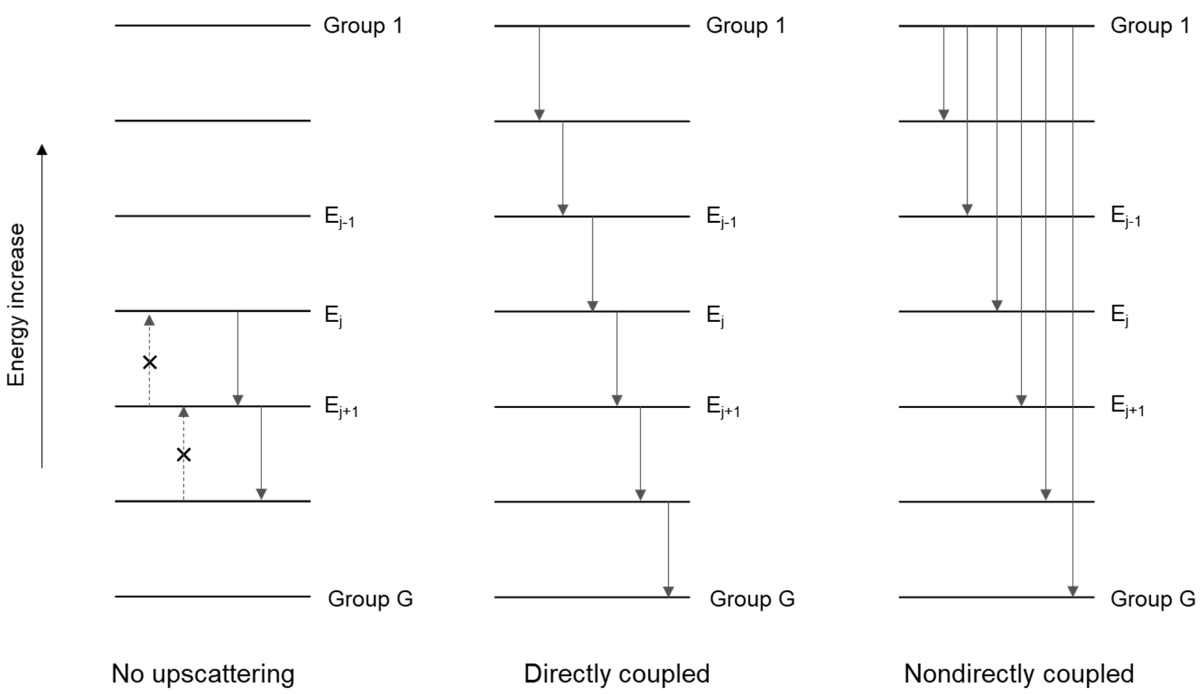

Figure 5-3 Alternative types of multigroup coupling

Neutron interactions with matter can be classified into two general categories: absorption and scattering. In neutron absorption processes, the incident neutron is absorbed into the target nucleus to form a compound nucleus in a highly excited state. The excited nucleus could subsequently decay by emitting one or more energetic gamma-ray photons, which are known as neutron-capture photons. The cross section for neutron capture is very small for high-energy neutrons with energies between 10 keV and 10 MeV, which could be a few percentage of the full neutron scattering cross sections. Therefore, neutron capture is not particularly important for fast neutrons, but should be considered for thermal neutrons (Shultis and Faw 1996).

Two types of neutron scattering are possible – elastic and inelastic. Inelastic scattering is similar to neutron absorption. The incident neutron is first absorbed by the target nucleus to form a compound nucleus in an excited state. The excited nucleus then emits a neutron, usually with lower kinetic energy than the incident neutron, and the excitation energy is released via the emission of one or more gamma-ray photons. Due to constraints in all scattering interactions, inelastic scattering of neutrons usually occurs only for neutrons with relatively high energies (>10 keV) (Duderstadt and Hamilton 1976).

As stated above, the photon source in each group could include the production of secondary photons from scattering reactions of photons in groups with higher energies, neutron capture of thermal neutrons, and inelastic scattering of fast neutrons. The diffusion equation for photon group *g* without any internal source is shown below. The equation is similar to the multigroup neutron diffusion equations but with extra terms to take into account the secondary photons produced in neutron interactions.

$$\frac{1}{c}\frac{\partial\Phi_g(x,t)}{\partial t} - \nabla\cdot\mathbb{D}_g(x,t)\nabla\Phi_g(x,t) + \mu_g\Phi_g(x,t) = \sum_{g'=1}^{G}\mu_{sg'g}\Phi_{g'} + \Sigma_{\gamma g}\phi_2 + \Sigma_{ing}\phi_1 + S_{\gamma g}(x,t) \tag{5-2}$$

where μ_g is the group *g* attenuation coefficient in cm^{-1}; $\mu_{sg'g}$ is the group-transfer coefficient from group g' to group *g* in cm^{-1}; $\Sigma_{\gamma g}$ is the macroscopic neutron capture cross section from thermal neutron to photon group *g* in cm^{-1}; and Σ_{ing} is the macroscopic neutron inelastic scattering cross section to photon group *g* in cm^{-1}.

Since photons will only lose energy during the transport process, as shown in Figure 5-3, we can set

$$\mu_{sg'g} = 0\,,\ \text{for}\ g' > g \tag{5-3}$$

The group *g* attenuation coefficient μ_g already considers the in-group scattering term μ_{sgg} which characterizes the probability that a particle can suffer a scattering collision that reduces its energy but will still remain within the current group. Therefore, the photon scattering terms can be simplified:

$$\sum_{g'=1}^{G}\mu_{sg'g}\Phi_{g'} = \sum_{g'=1}^{g-1}\mu_{sg'g}\Phi_{g'} \tag{5-4}$$

The multigroup diffusion equation for photons without any internal source (besides secondary photons) can be written as

$$\frac{1}{c}\frac{\partial\Phi_g(x,t)}{\partial t} - \nabla\cdot\mathbb{D}_g(x,t)\nabla\Phi_g(x,t) + \mu_g\Phi_g(x,t) = \sum_{g'=1}^{g-1}\mu_{sg'g}\Phi_{g'} + \Sigma_{\gamma g}\phi_2 + \Sigma_{ing}\phi_1 \qquad g = 1,2,\ldots,G \tag{5-5}$$

For photon radiation, absorbed dose is frequently used to quantify the radiation level in the material. Dose is a measure of the amount of energy from an ionizing radiation that is deposited in a mass of some material. The SI unit of dose is gray (symbol: Gy) which is defined as the absorption of one joule of radiation energy per kilogram of matter. The dose can be calculated through the equation shown below.

$$Dose = \sum_{g=1}^{G}\Psi_g\left(\frac{\mu_{en}}{\rho}\right)_g\,,\ \text{where}\ \Psi_g = \int_0^t \Phi_g dt\,\mathcal{E}_{\gamma g} \tag{5-6}$$

where Ψ_g is the photon energy fluence in group *g* in MeV/cm^2 which can be calculated by multiplying the photon fluence (photons/cm^2) with the photon energy $\mathcal{E}_{\gamma g}$ (MeV), and $\frac{\mu_{en}}{\rho}$ is the mass energy absorption coefficient in cm^2/g which depends on photon energy and transport material.

5.1.2 Heat Conduction

Gamma radiation also can lead to localized temperature rise in the concrete. The same one-dimensional heat conduction equation with an internally generated heat source, as shown in Equation (4-6), can still be used to obtain the thermal field in the concrete.

Photon energy is converted to heat when photons are absorbed during transport. Therefore, the volumetric heating rate caused by photon radiation can be estimated by the summation of the photon energy absorbed in all groups (William et al. 2013):

$$Q(x,t) \approx \sum_{g=1}^{G} 1.6 \times 10^{-13} \mathcal{E}_{\gamma g} \mu_{ag} \Phi_g(x,t) \tag{5-7}$$

where μ_{ag} is the linear energy-absorption coefficient for gamma-rays in group g in cm^{-1} which is μ_{en}. This parameter is equal to μ_{en} in $\frac{\mu_{en}}{\rho}$.

5.1.3 Determination of Transport Properties

Similar to neutron transport, the photon transport properties of a concrete wall could be affected by the damage of concrete induced by fast neutron radiation and elevated temperatures. The approach based on the cross-property correlation presented in Section 4.2 is still assumed to be valid here to estimate the variation of transport properties for photon diffusion and heat conduction. The effective thermal conductivity and effective photon diffusion coefficient can be determined as functions of time, fast neutron flux, and temperature:

$$k_{eff} = f_k\left(k_0, \upsilon_0, \frac{E_d}{E_0}, \frac{k_d}{k_0}, \int_0^t \phi_1 dt\,, T\right), \mathbb{D}_{eff} = f_{\mathbb{D}}\left(\mathbb{D}_0, \upsilon_0, \frac{E_d}{E_0}, \frac{\mathbb{D}_d}{\mathbb{D}_0}, \int_0^t \phi_1 dt\,, T\right) \tag{5-8}$$

5.2 Numerical Analyses

5.2.1 Coupled Neutron and Gamma-Ray Radio-Thermo Analysis

As shown in Section 4.2 and Section 5.1.3, *k*, *ρ*, $\mathcal{D}_i$, and $\mathbb{D}_g$are time- and position-dependent parameters, and all other parameters are assumed to be constants. The coupled radio-thermo analysis of fast neutrons, thermal neutrons, gamma-ray photons, and thermal fields within nuclear-irradiated concrete can be performed based on the two-group neutron diffusion model, the multigroup photon diffusion model, and the heat conduction equation. The effects of neutron radiation-induced degradation and thermal deterioration of concrete can be taken into account. The governing equations are

$$\frac{1}{v_1}\frac{\partial \phi_1(x,t)}{\partial t} - \nabla \cdot \mathcal{D}_1(x,t) \nabla \phi_1(x,t) + \Sigma_{R1}\phi_1(x,t) = 0 \tag{5-9}$$

$$\frac{1}{v_2}\frac{\partial \phi_2(x,t)}{\partial t} - \nabla \cdot \mathcal{D}_2(x,t)\nabla \phi_2(x,t) + \Sigma_{a2}\phi_2(x,t) = \Sigma_{s12}\phi_1(x,t) \tag{5-10}$$

$$\frac{1}{c}\frac{\partial \Phi_g(x,t)}{\partial t} - \nabla \cdot \mathbb{D}_g(x,t)\nabla \Phi_g(x,t) + \mu_g \Phi_g(x,t) = \sum_{g'=1}^{g-1} \mu_{sg'g}\Phi_{g'} + \Sigma_{\gamma g}\phi_2 + \Sigma_{ing}\phi_1 \qquad g = 1,2,\ldots,G \tag{5-11}$$

$$\begin{aligned} c_p\rho(x,t)\frac{\partial T(x,t)}{\partial t} &= \nabla \cdot k(x,t)\nabla T(x,t) + 1.6\times 10^{-13}\Sigma_c \mathcal{E}_b \phi_2(x,t) \\ &+ \sum_{g=1}^{G} 1.6\times 10^{-13}\mathcal{E}_{\gamma g}\mu_{ag}\Phi_g(x,t) \end{aligned} \tag{5-12}$$

The same implicit finite difference approach used in Chapter 4 was adopted to solve the problem. Initial conditions, boundary conditions, and time step are shown in the next section as a case study. The bisection method was used for root-finding iteration in each time step, and the speed of convergence is satisfactory.

5.2.2 Input Parameters

The input parameters include all of the parameters listed in Section 4.3.2 and in Table 5-1.

Table 5-1 Input parameters

Gamma-ray/photon	Concrete
• Photon source (boundary conditions)	• Photon diffusion coefficients ($\mathbb{D}_g$) • Coefficients and cross sections (μ_g, $\mu_{sg'g}$, $\left(\frac{\mu_{en}}{\rho}\right)_g$, Σ_{in}, and $\Sigma_{\gamma ig}$) • $\frac{\mathbb{D}_d}{\mathbb{D}_0}$

5.2.3 Verification

In this section, the neutron/photon diffusion theory is verified using MCNP 6.2 (Werner et al. 2018). MCNP is a general-purpose Monte Carlo N-Particle (MCNP) transport code developed by Los Alamos National Laboratory which can be used to calculate the transport of different particles including neutrons and photons. To compare the results between the neutron/photon diffusion theory developed in this study with MCNP results, a simple case study was developed as shown in Figure 5-4. The comparison with MCNP is to verify the characterization of the diffusion processes in the present models, not the impact of concrete damage on neutron and photon diffusion because MCNP 6.2 cannot handle degraded concrete.

There is a beam of particles with energy 1 MeV which transports through a cylinder filled with light water. The particles can be either neutrons or photons. The height of the cylinder is 50 cm and the diameter is 10 cm. The composition of the light water is shown in Table 5-2, which includes the constituent elements, their atomic fraction, and the identification number (ZAID). Since the particles only have one energy level, a one-speed diffusion equation can be used for both neutrons and photons (Equation (4-2) and Equation (5-1)). In these two equations, the actual values of neutron speed v, light speed c, macroscopic absorption cross section of neutrons Σ_a, and photon absorption coefficient μ_a can be obtained through known databases once the particle energy levels and transport medium are known. However, the diffusion coefficients $\mathcal{D}$ and $\mathbb{D}$ are the two parameters that need to be estimated and adjusted to ensure the accuracy of the diffusion approximation of particle transport. First, reference values were obtained in the literature. Then, they were adjusted to obtain the best match with the MCNP results. All parameters needed for diffusion theory are listed in Table 5-3.

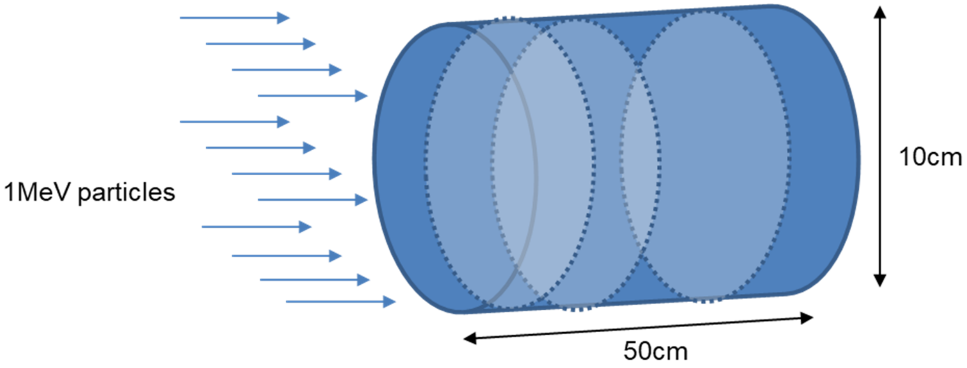

Figure 5-4 The configuration of the study case for verification

Table 5-2 Composition of the light water

Element	Nuclide fraction	ZAID
O	1	8016
H	2	1001

Table 5-3 Input parameters for the verification of diffusion equations

Parameters	Values	Note
Neutron		
$\mathcal{D}$ [cm]	0.13	
Σ_a [cm^{-1}]	0.022	(Shultis and Faw 1996)
v [cm/sec]	1.38×10^9	1 MeV neutron
Photon		
$\mathbb{D}$ [cm]	0.45	
μ_a [cm^{-1}]	0.03103	(Hubbell and Seltzer 1995)
c [cm/sec]	3×10^{10}	Light speed

The results of diffusion theory and MCNP are plotted in Figure 5-5, which shows the profiles of the normalized neutron/photon flux along the height of the cylinder. Normalized flux means the flux of the particles at the left side boundary of the light water cylinder is 1 for all cases. The results of diffusion theory well match the results of MCNP for both neutrons and photons.

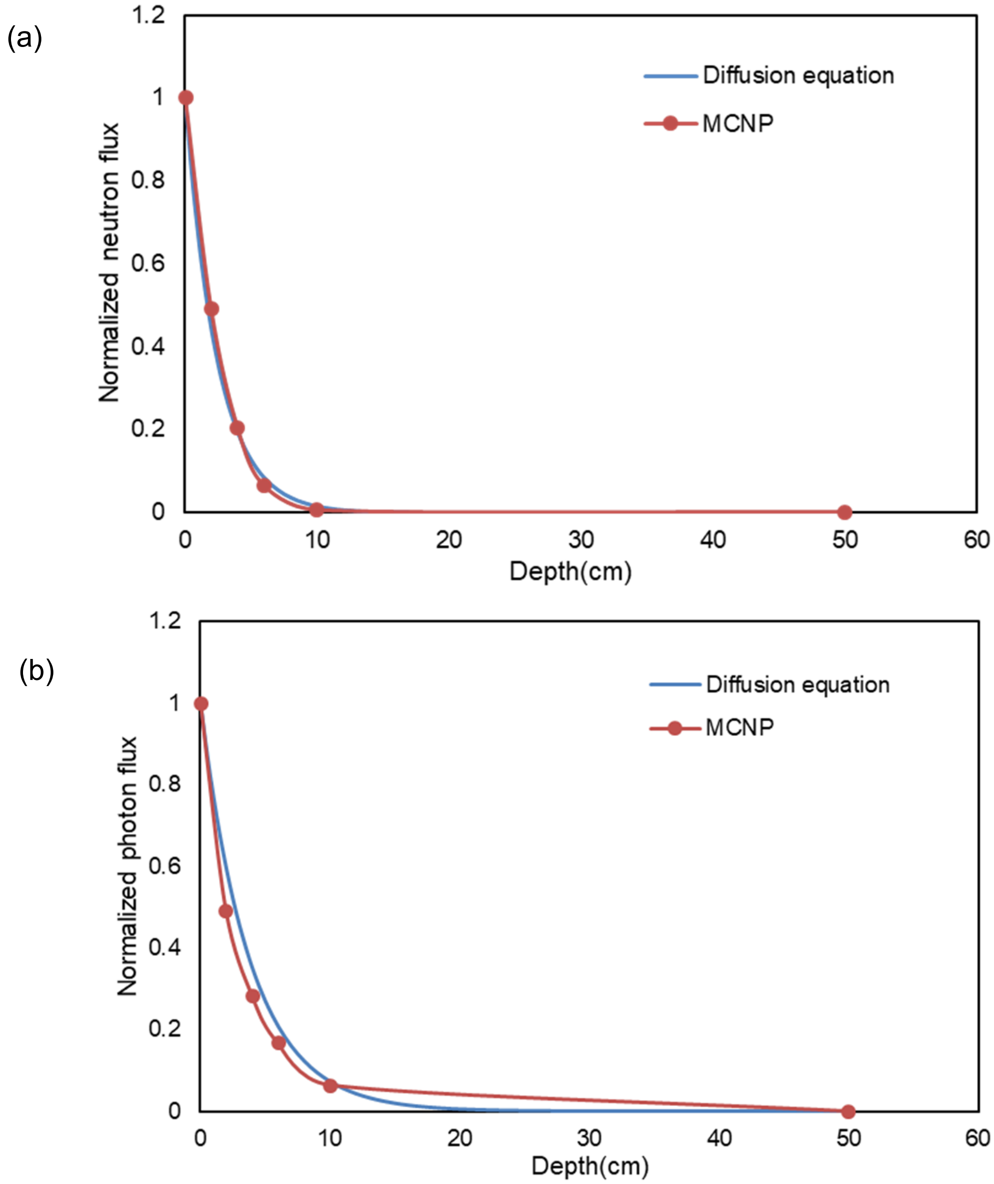

Figure 5-5 Comparison between diffusion theory and MCNP: (a) neutron (b) photon

5.2.4 A Case Study

The same concrete biological shielding wall without rebar embedment shown in Figure 4-6 is used here as a study case to show the capability of the model. The radiation source includes both neutrons and gamma-rays. The radiation field (neutron and gamma) as well as the temperature field in a concrete biological shield during 80 years of operation are obtained.

All parameters used in the case study for neutron diffusion shown in Section 4.2.4 are used. The additional input parameters needed are shown below. The energy range of the gamma-ray photon source is assumed to be 0.3 to 7.2 MeV, which is the energy spectrum of gamma-rays emitted from fission measured by Maienschein et al. (1958). The photons are divided into 5 groups (from group 5 to group 1): 0.3-0.6, 0.6-1.2, 1.2-2.4, 2.4-4.8, and 4.8-7.2. There is little data available on the expected gamma flux in the reactor cavity and concrete biological shield. Remec et al. (2016) provided an estimated maximum value in concrete for two-loop pressurized water reactors (PWRs) (9.08×10^9 photons/($\text{cm}^2 \cdot \text{sec}$)) and three-loop PWRs ($3.37 \times 10^9$ photons/($\text{cm}^2 \cdot \text{sec}$)) for $E > 0.01$ MeV. For this study case, a constant photon flux of 1.6×10^9 photons/($\text{cm}^2 \cdot \text{sec}$) for each group was assumed at the inner surface of the wall. Thus, the total photon flux is 9×10^9 photons/($\text{cm}^2 \cdot \text{sec}$). The photon flux at the outer surface of the wall was approximately 10^{-3} of the flux at the inner surface (Esselman and Bruck 2013). All other parameters are listed in Figure 5-6 and Figure 5-7 show the results of numerical analyses for pure gamma-ray photon diffusion. Neutron radiation and damage of concrete is not considered. Figure 5-6 shows the temperature profiles in the concrete with and without considering radiation heating. As one can see from Figure 5-6 (b), compared to the neutron radiation problem, the gamma radiation in concrete leads to negligible changes of the temperature profile in the concrete (maximum change is less than 0.3 ºC). Figure 5-7 shows the photon flux for each group and the total absorbed dose in Gray after 80 years. If the damage is not considered, the profiles of photon flux and temperature will not change over time.

Table 5-4 Parameters used in the ordinary concrete numerical analysis

Parameter	Values	Reference
$\mathbb{D}_1$ [cm]	1*	-
$\mathbb{D}_2$ [cm]	1*	-
$\mathbb{D}_3$ [cm]	1*	-
$\mathbb{D}_4$ [cm]	1*	-
$\mathbb{D}_5$ [cm]	1*	-
μ_1 [cm^{-1}]	0.06203	(Hubbell and Seltzer 1995)
μ_2 [cm^{-1}]	0.07855	(Hubbell and Seltzer 1995)
μ_3 [cm^{-1}]	0.11192	(Hubbell and Seltzer 1995)
μ_4 [cm^{-1}]	0.15578	(Hubbell and Seltzer 1995)
μ_5 [cm^{-1}]	0.21682	(Hubbell and Seltzer 1995)
μ_{s12} [cm^{-1}]	0.03*	-
μ_{s13} [cm^{-1}]	0.02*	-
μ_{s23} [cm^{-1}]	0.025*	-

Table 5-5 (Cont.)

Parameter	Values	Reference
μ_{s14} [cm^{-1}]	0.015*	-
μ_{s24} [cm^{-1}]	0.013*	-
μ_{s34} [cm^{-1}]	0.035*	-
μ_{s15} [cm^{-1}]	0.01*	-
μ_{s25} [cm^{-1}]	0.011*	-
μ_{s35} [cm^{-1}]	0.018*	-
μ_{s45} [cm^{-1}]	0.045*	-
$\left(\frac{\mu_{en}}{\rho}\right)_1$ [cm^2/g]	0.01763	(Hubbell and Seltzer 1995)
$\left(\frac{\mu_{en}}{\rho}\right)_2$ [cm^2/g]	0.02031	(Hubbell and Seltzer 1995)
$\left(\frac{\mu_{en}}{\rho}\right)_3$ [cm^2/g]	0.02445	(Hubbell and Seltzer 1995)
$\left(\frac{\mu_{en}}{\rho}\right)_4$ [cm^2/g]	0.02892	(Hubbell and Seltzer 1995)
$\left(\frac{\mu_{en}}{\rho}\right)_5$ [cm^2/g]	0.03029	(Hubbell and Seltzer 1995)
$\Sigma_{\gamma 1}$ [cm^{-1}]	0.003*	-
$\Sigma_{\gamma 2}$ [cm^{-1}]	0.003*	-
$\Sigma_{\gamma 3}$ [cm^{-1}]	0.003*	-
$\Sigma_{\gamma 4}$ [cm^{-1}]	0.003*	-
$\Sigma_{\gamma 5}$ [cm^{-1}]	0.003*	-
Σ_{in1} [cm^{-1}]	0*	-
Σ_{in2} [cm^{-1}]	0.008*	-
Σ_{in3} [cm^{-1}]	0.01*	-
Σ_{in4} [cm^{-1}]	0.012*	-
Σ_{in5} [cm^{-1}]	0.01*	-
c [cm/sec]	3×10^{10}	-
$\frac{\mathbb{D}_d}{\mathbb{D}_0}$	10*	-

* Assumed values to illustrate sensitivity.

. Some of them are available in the literature, and their values were assumed for the sensitivity analysis.

Figure 5-6 and Figure 5-7 show the results of numerical analyses for pure gamma-ray photon diffusion. Neutron radiation and damage of concrete is not considered. Figure 5-6 shows the temperature profiles in the concrete with and without considering radiation heating. As one can see from Figure 5-6 (b), compared to the neutron radiation problem, the gamma radiation in concrete leads to negligible changes of the temperature profile in the concrete (maximum change is less than 0.3 ºC). Figure 5-7 shows the photon flux for each group and the total absorbed dose in Gray after 80 years. If the damage is not considered, the profiles of photon flux and temperature will not change over time.

Table 5-4 Parameters used in the ordinary concrete numerical analysis

Parameter	Values	Reference
$\mathbb{D}_1$ [cm]	1^*	-
$\mathbb{D}_2$ [cm]	1^*	-
$\mathbb{D}_3$ [cm]	1^*	-
$\mathbb{D}_4$ [cm]	1^*	-
$\mathbb{D}_5$ [cm]	1^*	-
μ_1 [cm^{-1}]	0.06203	(Hubbell and Seltzer 1995)
μ_2 [cm^{-1}]	0.07855	(Hubbell and Seltzer 1995)
μ_3 [cm^{-1}]	0.11192	(Hubbell and Seltzer 1995)
μ_4 [cm^{-1}]	0.15578	(Hubbell and Seltzer 1995)
μ_5 [cm^{-1}]	0.21682	(Hubbell and Seltzer 1995)
μ_{s12} [cm^{-1}]	0.03^*	-
μ_{s13} [cm^{-1}]	0.02^*	-
μ_{s23} [cm^{-1}]	0.025^*	-

Table 5-5 (Cont.)

Parameter	Values	Reference
μ_{s14} [cm^{-1}]	0.015^*	-
μ_{s24} [cm^{-1}]	0.013^*	-
μ_{s34} [cm^{-1}]	0.035^*	-
μ_{s15} [cm^{-1}]	0.01^*	-
μ_{s25} [cm^{-1}]	0.011^*	-

μ_{s35} [cm^{-1}]	0.018*	-
μ_{s45} [cm^{-1}]	0.045*	-
$\left(\frac{\mu_{en}}{\rho}\right)_1$ [cm^2/g]	0.01763	(Hubbell and Seltzer 1995)
$\left(\frac{\mu_{en}}{\rho}\right)_2$ [cm^2/g]	0.02031	(Hubbell and Seltzer 1995)
$\left(\frac{\mu_{en}}{\rho}\right)_3$ [cm^2/g]	0.02445	(Hubbell and Seltzer 1995)
$\left(\frac{\mu_{en}}{\rho}\right)_4$ [cm^2/g]	0.02892	(Hubbell and Seltzer 1995)
$\left(\frac{\mu_{en}}{\rho}\right)_5$ [cm^2/g]	0.03029	(Hubbell and Seltzer 1995)
$\Sigma_{\gamma 1}$ [cm^{-1}]	0.003*	-
$\Sigma_{\gamma 2}$ [cm^{-1}]	0.003*	-
$\Sigma_{\gamma 3}$ [cm^{-1}]	0.003*	-
$\Sigma_{\gamma 4}$ [cm^{-1}]	0.003*	-
$\Sigma_{\gamma 5}$ [cm^{-1}]	0.003*	-
Σ_{in1} [cm^{-1}]	0*	-
Σ_{in2} [cm^{-1}]	0.008*	-
Σ_{in3} [cm^{-1}]	0.01*	-
Σ_{in4} [cm^{-1}]	0.012*	-
Σ_{in5} [cm^{-1}]	0.01*	-
c [cm/sec]	3×10^{10}	-
$\frac{\mathbb{D}_d}{\mathbb{D}_0}$	10*	-

* Assumed values to illustrate sensitivity.

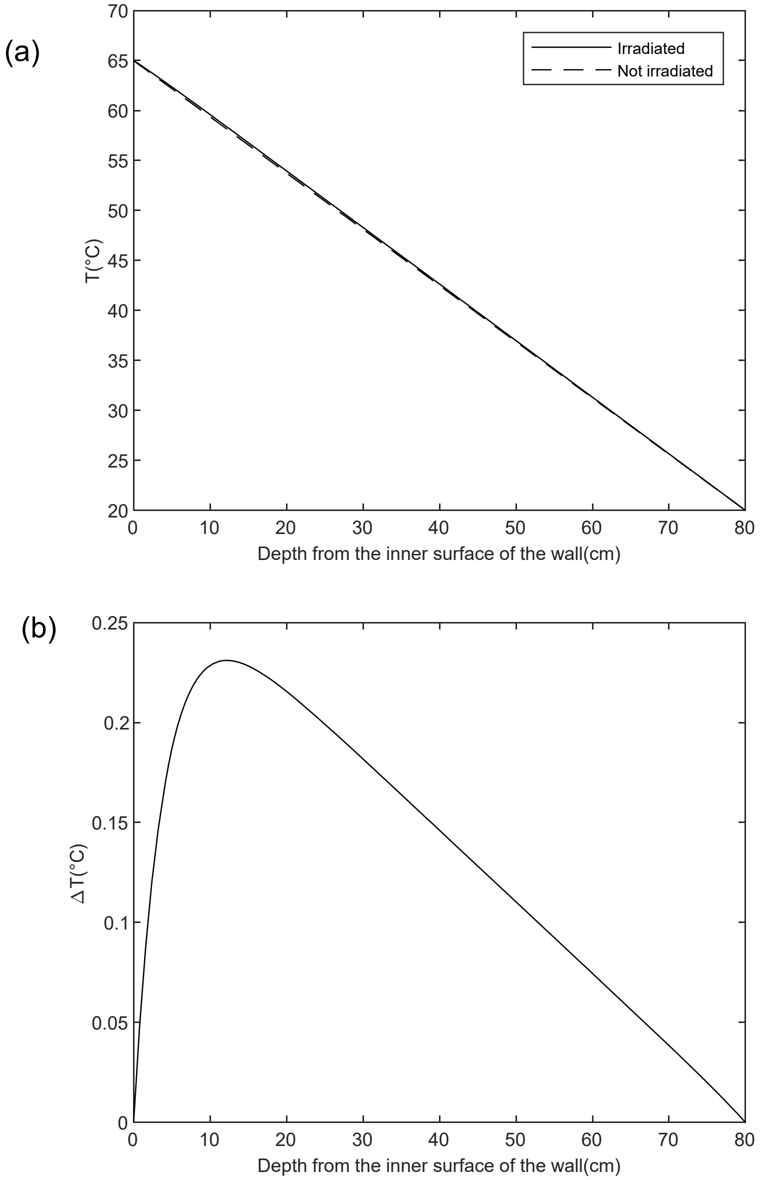

Figure 5-6 Temperature profiles along the concrete depth for pure gamma radiation: (a) absolute values without radiation and with radiation heating considered; (b) temperature changes compared to the initial values

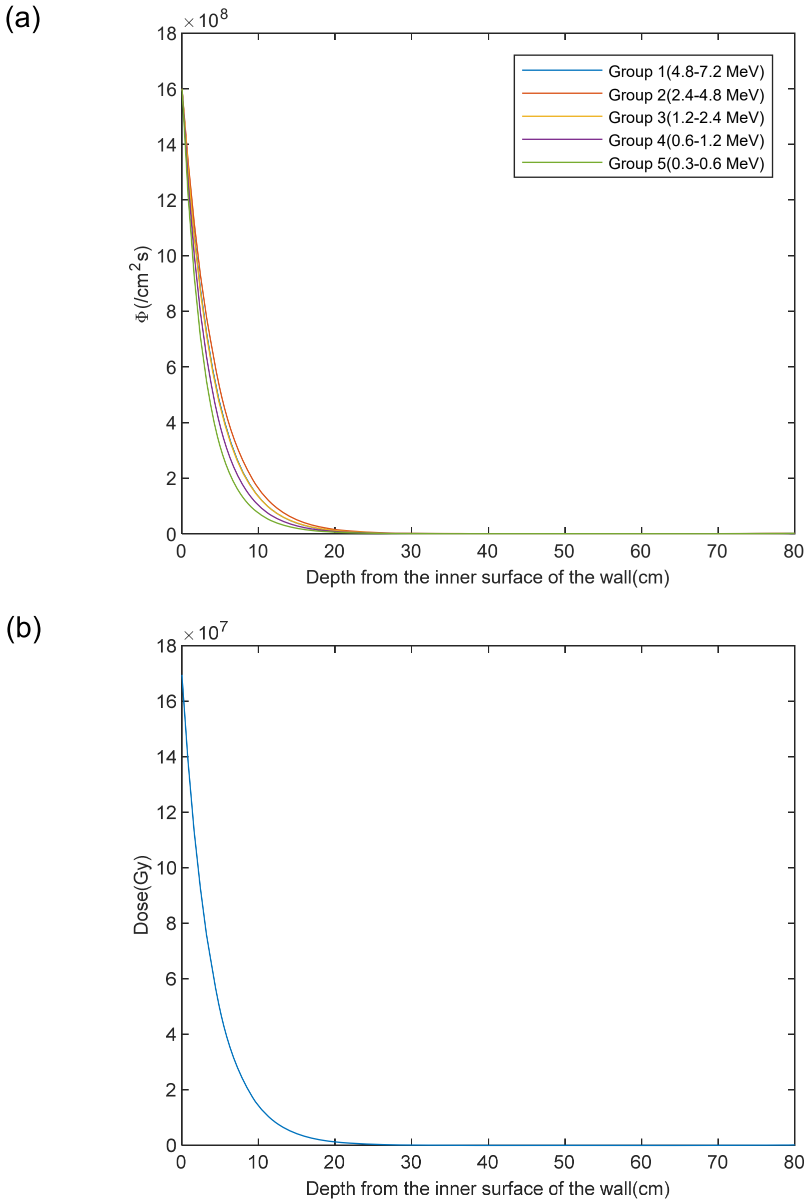

Figure 5-7 Gamma-ray photon level: (a) photon flux for each group; (b) absorbed dose in Gray after 80 years

Figure 5-8 through Figure 5-10 show some of the numerical results of the coupled neutron and gamma-ray radio-thermo analysis. Some results are not shown, since they are very similar to the neutron diffusion results in Section 4.3.4, including the profiles of the damage parameter, thermal conductivity profiles, neutron diffusion coefficient profiles, and neutron flux and fluence profiles.

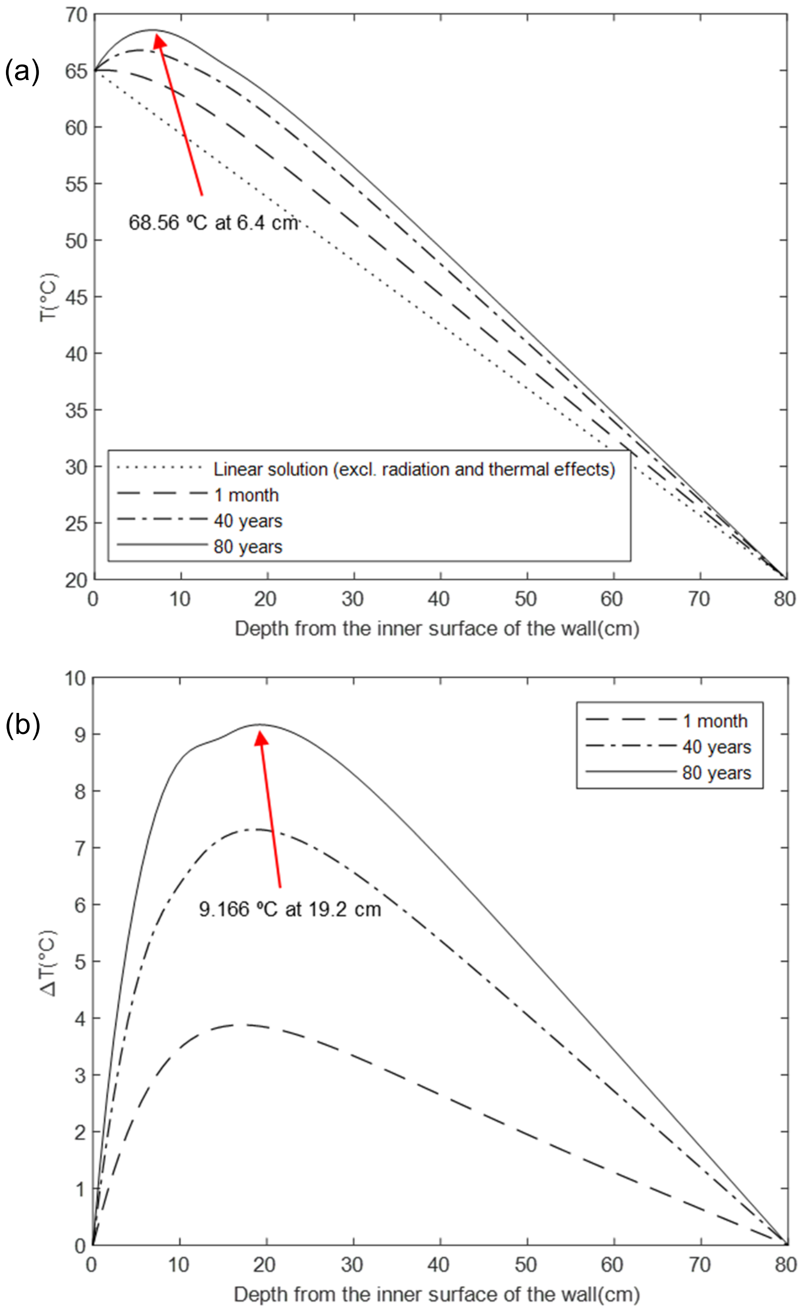

Figure 5-8 Temperature profiles along the concrete depth: (a) absolute values without radiation and thermal effects considered and with these effects considered at 1 month, 40 years, and 80 years; (b) temperature changes compared to the initial values

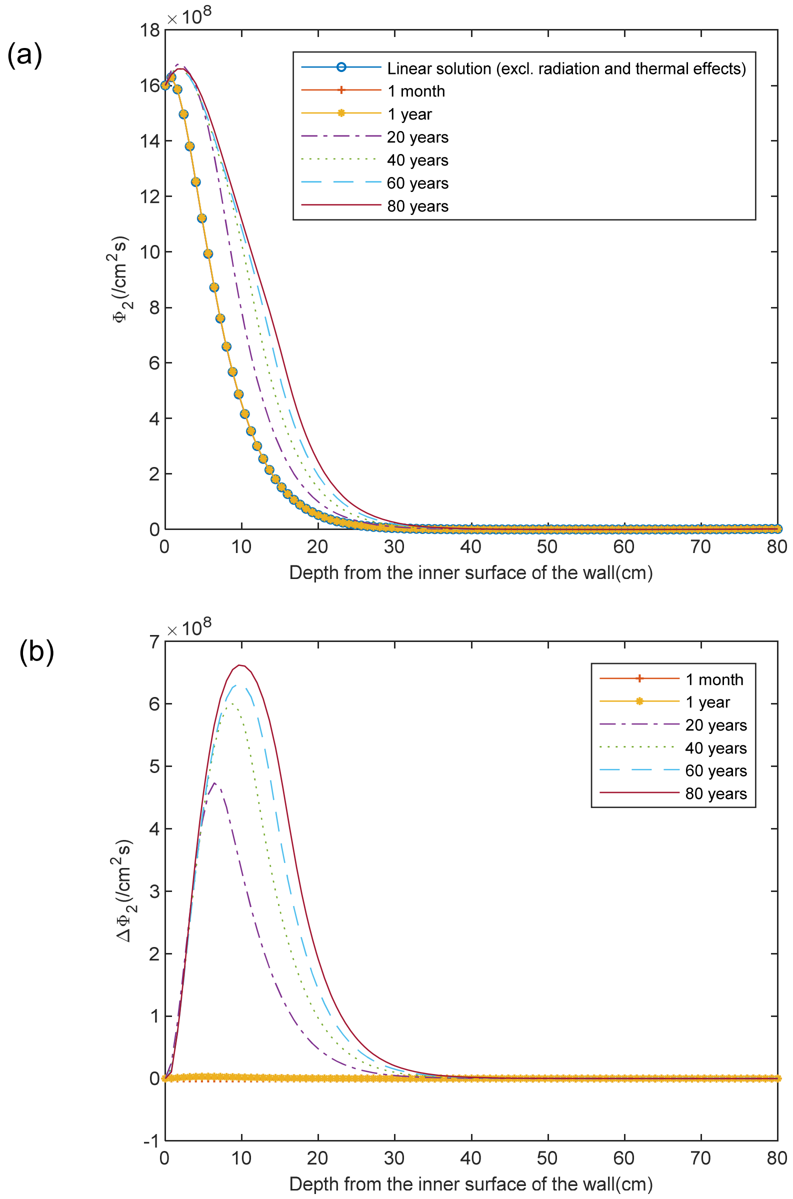

Figure 5-9 Photon flux profiles in group 2 along the concrete depth: (a) absolute values with and without the radiation and thermal effects after different periods of exposure; (b) photon flux increases compared to the case without the radiation and thermal effects

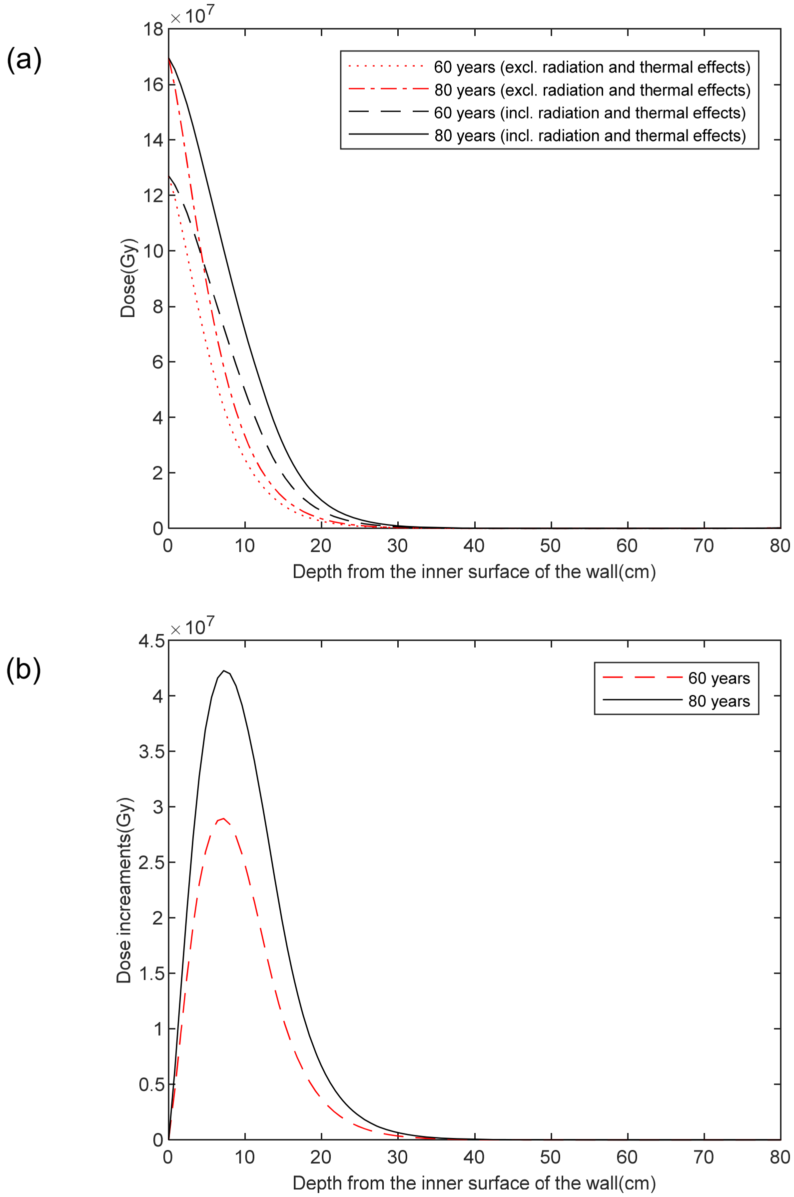

Figure 5-10 **Gamma radiation absorbed dose (Gy) along the concrete depth at 60 years and 80 years: (a) absolute values with and without considering the radiation and thermal effects; (b) dose increments compared to the case without these effects considered**

Figure 5-8 shows the temperature profiles in the concrete with and without the effects of damage induced by nuclear irradiation and temperature after 1 month, 40 years, and 80 years of exposure. If the damage is not considered, the temperature profile will not change over time after the steady-state temperature distribution is reached. As one can see from Figure 5-8, the damage of radiation and temperature in concrete leads to larger changes of the temperature profile in the concrete compared to the temperature rises caused by neutron heating only (Figure 4-9 (b)) or gamma radiation heating only (Figure 5-6 (b)). The maximum change is less than 10 ºC and the locations are also marked. Also, the increase of thermal neutron flux and photon flux over time will contribute to the additional temperature rise.

The nonlinear solutions of the neutron flux and gamma-ray photon flux profiles in the concrete up to 80 years were obtained. Figure 5-9 and Figure 5-10 show the results of photon diffusion in group 2. The results for other photon groups are very similar. The linear solution in the figures are the solutions excluding the effect of damage, whereas the nonlinear solutions considered the effect of damage. Similar to the results of neutron diffusion, it is shown that the photon flux increases significantly with time, especially for the concrete near the radiation source. The peak of the increase occurs near the inner surface. This is mainly caused by the damage induced by neutron radiation and elevated temperature, which can result in considerable degradation of concrete as a shielding material. The profiles of gamma-ray dose in the concrete wall at 60 years and 80 years are plotted in Figure 5-10. Similar to the gamma-ray photon profiles, considerable increases of absorbed dose from the linear solution without considering the damage effect are observed for the concrete near the radiation source.

5.3 Summary

A multigroup diffusion model was used to simplify the gamma-ray photon transport equation. The photon source in each photon group includes the production of secondary photons from scattering reactions of photons in the photon groups with higher energies, neutron captures of thermal neutrons, and inelastic scattering of fast neutrons. In this chapter, coupled radio-thermo analysis was performed based on one-dimensional two-group neutron diffusion equations, multigroup photon diffusion equations, and the heat conduction equation with heat sources considering neutron and gamma-ray heating. The fast and thermal neutron fields, gamma-ray photon fields of all photon groups, as well as the thermal field in concrete can be obtained. Similar to the neutron irradiation transport problem, the damage of concrete can also change the gamma-ray photon transport properties of concrete. The same approach used in Chapter 4 can still be used here, which is the cross-property correlation theory combined with the multiphase and multiscale model developed in Chapter 2 to estimate the variations of neutron diffusion coefficients, photon diffusion coefficients, as well as the thermal conductivity of concrete caused by neutron radiation and thermal effects. The same ordinary concrete wall used for the neutron transport case study was analyzed for up to 80 years of operation as a simplified example of a typical concrete biological shield in NPPs. Similar results for neutron transport were observed. In the sensitivity study case, the concrete damage increases the photon diffusion coefficient by a factor of 10, and considerable increases in absorbed doses of gamma rays compared to the linear solution (without considering the damage effect) are observed for the concrete near the radiation source.

6 COUPLED RADIO-THERMO-MECHANICAL ANALYSIS

In this chapter, a comprehensive case study is developed to analyze the long-term performance of a simplified concrete biological shielding wall under nuclear radiation, elevated temperature, and mechanical loadings in an NPP. The coupled radio-thermo-mechanical analysis combines all models developed in previous chapters, including the multiscale and multiphase model (Chapter 2), the coupled damage-creep model (Chapter 3), and the coupled radio-thermo model (Chapter 4 and Chapter 5). The objective of the case study is to show the capability of the approach that can be used to estimate the long-term mechanical and transport response and the state of a concrete biological shielding wall in NPPs under normal operational conditions.

Figure 6-1 shows the overall calculation flowchart of the analysis. The inputs needed to start the analysis are environment information (boundary conditions and initial conditions of the concrete, e.g., neutron flux, photon flux, and environmental temperature) and concrete properties, which are shown in detail in Section 6.2. There are two stages in the case study. In the first stage, the radio-thermo analysis for neutron, photon, and heat transport, developed in Chapters 4 and 5, and the multiscale and multiphase model developed in Chapter 2, are fully coupled, and a coupled radio-thermo analysis is performed. At this stage, it is a one-dimensional problem along the depth of the concrete wall that is solved through an implicit finite difference approach. The results are the state of concrete (e.g., the extent of concrete damage, D_{Rad}) and radiation levels at different depths of the concrete biological shielding wall at each time step. It should be noted that the modeling in the first stage is only one-dimensional. Then, in the second stage, some of these results from the first stage, such as concrete damage, are applied to the coupled damage-creep analysis shown in Chapter 3. In each time step, the results obtained in the first stage will feed the coupled damage-creep analysis in the second stage as inputs in ABAQUS. The radio-thermo analysis in the first stage is quite complex and will take some time to be solved numerically. So, the coupled radio-thermo analysis at the first stage will not be included in the ABAQUS subroutine with the coupled damage-creep analysis to improve the overall calculation speed. Otherwise, the computational time of finite element analysis in ABAQUS will be very long even when a coarse element mesh is used. As a result, these two stages of analyses are not fully coupled. As shown in Figure 6-1, the three-dimensional radio-thermo-mechanical analysis through ABAQUS is a one-way coupling process, which means that within each time step, the damage calculated in ABAQUS will not be considered in the coupled radio-thermo analysis in the first stage.

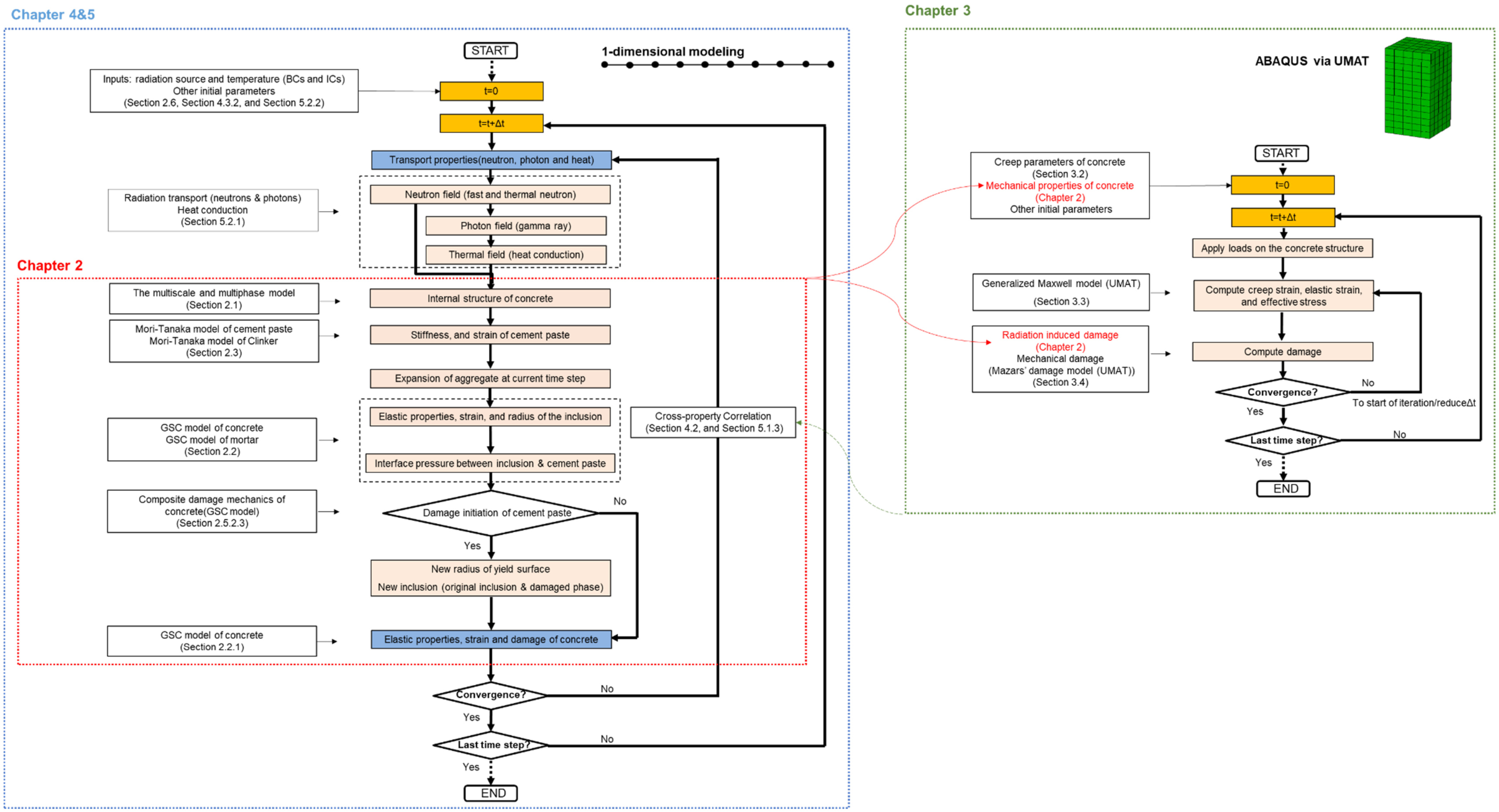

Figure 6-1 Calculation flowchart for coupled radio-thermo-mechanical analysis

6.1 Configuration of the Case Study

A concrete wall without rebar embedment shown in Figure 6-2(a) is used for the comprehensive case study. The thickness of the wall is 1.6 meters, the height is 6 meters, and the width of the section is 1 meter (a unit width). It represents a section of simplified concrete biological shielding wall in NPPs. It was assumed that the neutron flux, photon flux, and temperature are uniformly distributed on the inner (left) surface of the wall. The outer (right) surface of the wall is exposed to the ambient environment. Thus, the neutron, photon, and heat conduction can be considered to be a one-dimensional problem along the depth of the concrete wall. One-dimensional coupled radio-thermo analysis can be applied to obtain the state of concrete material and radiation level at each point up to 80 years of normal operation. In ABAQUS, the three-dimensional radio-thermo-mechanical analysis is applied to the whole concrete section. The finite element model with the applied boundary conditions and mechanical loadings is shown in Figure 6-2 (b). The bottom is fixed in the z direction, and the front and back surfaces are fixed in the y direction. The mechnical loadings could include self-weight of the concrete material; other normal operating loads, such as the weight of a nuclear reactor if the concrete biological shielding wall also supports the RPV; and posssible loads in accidentical conditions.

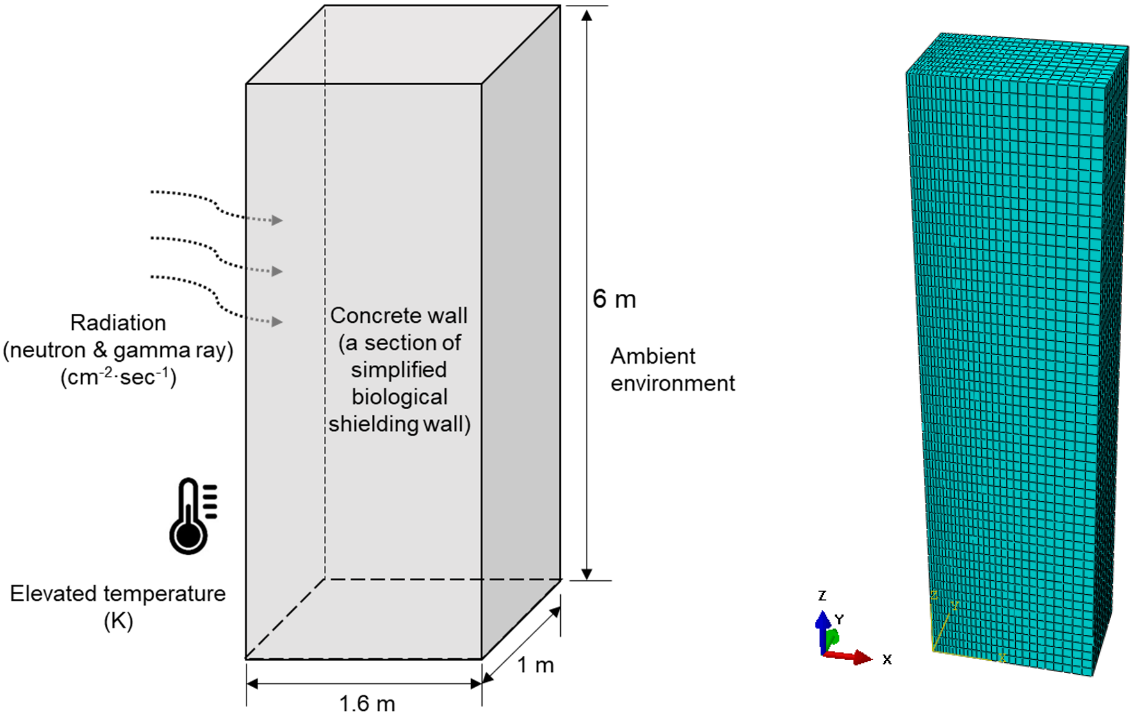

(a) (b)

Figure 6-2 The configuration of the section of simplified biological shielding wall: (a) geometry; (b) finite element model

6.2 Input Parameters

First, the properties of concrete need to be determined. For the case study, the concrete wall is considered to be made of ordinary Portland cement concrete and crushed gravel without rebar embedment. The mix proportion is water/cement/aggregate= 0.4/1/4.99 by weight, and the curing time is one year. The strengths of the hardened cement paste are f_c' = 65 MPa and f_t = 4 MPa. Prony series parameters are listed in Table 3-1. Parameters for the Mazars' damage model used are $A_t = 1$, $B_t = 15000$, $A_c = 1.2$, $B_c = 1500$, which can be measured through compression and tension tests of concrete specimens.

Second, the loadings need to be obtained, such as the mechanical loadings, temperature and radiation level, as well as the corresponding transport properties of concrete. For the case study, only the self-weight of concrete is considered. The temperature was 65 ºC at the inner surface and 20 ºC at the outer surface. A constant neutron flux density of 3.2×10^{10} n/(cm^2·sec) was assumed at the inner surface of the wall for fast neutrons with an 0.1 MeV energy level and a neutron flux density of 4×10^{10} n/(cm^2·sec) was assumed for thermal neutrons with an 0.0253 eV energy level. The gamma-ray source has the same characteristics as the source used in Section 5.2.4. The photons were divided into five groups (from group 5 to group 1): 0.3-0.6, 0.6-1.2, 1.2-2.4, 2.4-4.8, 4.8-7.2 MeV, and a constant photon flux of 1.6×10^9 photons/(cm^2·sec) for each group was assumed at the inner surface of the wall. Thus, the total photon flux is 9×10^9 photons/(cm^2·sec).

Then, the behavior of some concrete components under nuclear radiation also needs to be obtained in order to analyze the performance of the concrete wall. Again, for our case, a linear regression of the serpentine data shown in Figure 2-17 was used as the degradation trend of the Young's modulus for the aggregate under neutron radiation. The expansion of aggregate particles under neutron radiation was assumed to be the middle trend line shown in Figure 6-3 based on Equation (2-11) and data collected in Biwer et al. (2020). All parameters used in the case study are listed in Table 6-1.

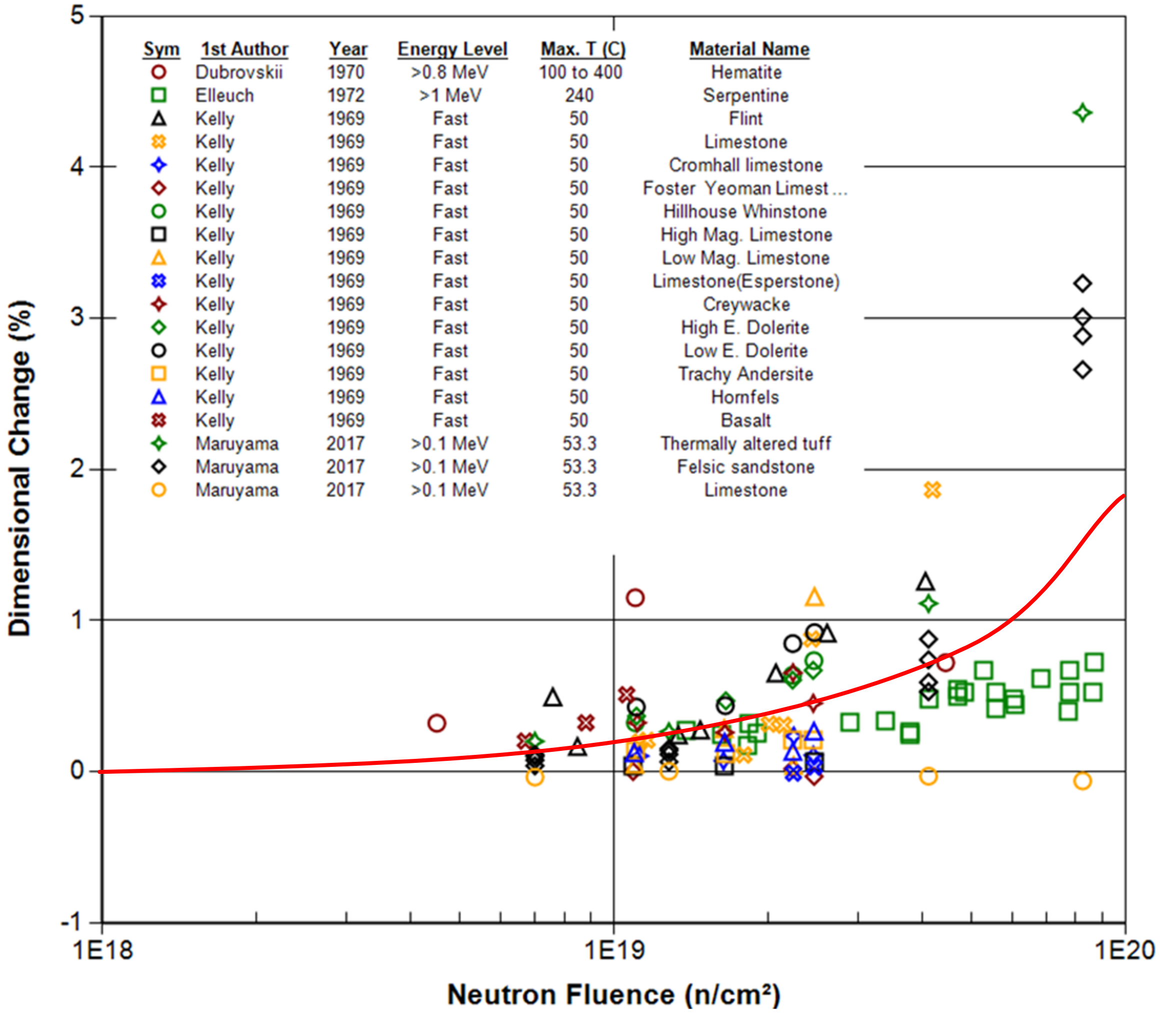

Figure 6-3 Dimensional change of aggregates curved fit using Equation (2-11): $\varepsilon_u = 4\%$, $\mathcal{A} = 0.77$, $\mathcal{B} = 5.8 \times 10^{-20}$

Table 6-1 Parameters used in the ordinary concrete numerical analysis

Parameters	Values	Reference
Environment		
Temperature, *T* [ºC]	65, left side; 20, right side	-
Fast neutron flux, ϕ_1 [/(cm^2·sec)]	3.2×10^{10} ($E > 0.1$ MeV), left side 3.2×10^{7} ($E > 0.1$ MeV), right side	-
Thermal neutron flux, ϕ_2 [/(cm^2·sec)]	4×10^{10} ($E < 0.0253$ eV), left side 4×10^{7} ($E < 0.0253$ eV), right side	-
The photon energy groups [MeV]	0.3-0.6, 0.6-1.2, 1.2-2.4, 2.4-4.8, 4.8-7.2,	-

Table 6-2 (Cont.)

Parameters	Values	Reference
Photon flux, Φ [/(cm^2·sec)]	1.6×10^9, left side; 1.6×10^6, right side	-
Concrete		
Mix proportion	water/cement/aggregate= 0.4/1/4.99	(REACTOR PHYSICS CONSTANTS 1963)
$\mathcal{D}_1$ [cm]	1.14	(REACTOR PHYSICS CONSTANTS 1963)
$\mathcal{D}_2$ [cm]	0.484	(REACTOR PHYSICS CONSTANTS 1963)
Σ_{R1} [cm^{-1}]	0.085	(REACTOR PHYSICS CONSTANTS 1963)
Σ_{s12} [cm^{-1}]	0.08**	–
Σ_{a2} [cm^{-1}]	0.0094	(REACTOR PHYSICS CONSTANTS 1963)
v_1 [cm/sec]	4.37×10^8	–
v_2 [cm/sec]	2.2×10^5	–
c_p [J/(kg·K)]	650	(Ursu 1985)
ρ [kg/cm^3]	2.3×10^{-3}	(REACTOR PHYSICS CONSTANTS 1963)
k [W/(cm·K)]	8.7×10^{-3}	(Ursu 1985)
Σ_c [cm^{-1}]	0.0094**	–
$\mathcal{E}_b$ [MeV]	5.5	(Price et al. 1957)
Curing time[days]	1 year	-
$\mathbb{D}_1$ [cm]	1**	-
$\mathbb{D}_2$ [cm]	1**	-
$\mathbb{D}_3$ [cm]	1**	-
$\mathbb{D}_4$ [cm]	1**	-
$\mathbb{D}_5$ [cm]	1**	-
μ_1 [cm^{-1}]	0.06203	(Hubbell and Seltzer 1995)
μ_2 [cm^{-1}]	0.07855	(Hubbell and Seltzer 1995)

Table 6-3 (Cont.)

Parameters	Values	Reference
μ_3 [cm^{-1}]	0.11192	(Hubbell and Seltzer 1995)
μ_4 [cm^{-1}]	0.15578	(Hubbell and Seltzer 1995)
μ_5 [cm^{-1}]	0.21682	(Hubbell and Seltzer 1995)
μ_{s12} [cm^{-1}]	0.03**	-
μ_{s13} [cm^{-1}]	0.02**	-
μ_{s23} [cm^{-1}]	0.025**	-
μ_{s14} [cm^{-1}]	0.015**	-
μ_{s24} [cm^{-1}]	0.013**	-
μ_{s34} [cm^{-1}]	0.035*	-
μ_{s15} [cm^{-1}]	0.01**	-
μ_{s25} [cm^{-1}]	0.011**	-
μ_{s35} [cm^{-1}]	0.018**	-
μ_{s45} [cm^{-1}]	0.045**	-
$\left(\frac{\mu_{en}}{\rho}\right)_1$ [cm^2/g]	0.01763	(Hubbell and Seltzer 1995)
$\left(\frac{\mu_{en}}{\rho}\right)_2$ [cm^2/g]	0.02031	(Hubbell and Seltzer 1995)
$\left(\frac{\mu_{en}}{\rho}\right)_3$ [cm^2/g]	0.02445	(Hubbell and Seltzer 1995)
$\left(\frac{\mu_{en}}{\rho}\right)_4$ [cm^2/g]	0.02892	(Hubbell and Seltzer 1995)
$\left(\frac{\mu_{en}}{\rho}\right)_5$ [cm^2/g]	0.03029	(Hubbell and Seltzer 1995)
$\Sigma_{\gamma 1}$ [cm^{-1}]	0.003**	-
$\Sigma_{\gamma 2}$ [cm^{-1}]	0.003**	-
$\Sigma_{\gamma 3}$ [cm^{-1}]	0.003**	-
$\Sigma_{\gamma 4}$ [cm^{-1}]	0.003**	-
$\Sigma_{\gamma 5}$ [cm^{-1}]	0.003**	-
Σ_{in1} [cm^{-1}]	0**	-
Σ_{in2} [cm^{-1}]	0.008**	-

Table 6-4 (Cont.)

Parameters	Values	Reference
Σ_{in3} [cm^{-1}]	0.01**	-
Σ_{in4} [cm^{-1}]	0.012**	-
Σ_{in5} [cm^{-1}]	0.01**	-
c [cm/sec]	3×10^{10}	-
Mazars' damage model	A_t = 1, B_t = 15000, A_c =1.2, B_c =1500, f_{t0} =4 MPa	(Pijaudier-Cabot and Mazars 2001)
Prony series parameters	Table 3-1	-
Cement paste		
Chemical composition [mass%]	C = 0.654, S = 0.2078, A = 0.0498, F = 0.0246*	-
ρ_c [kg/cm^3]	3.14×10^{-3}	-
f_{cc}' [MPa]	65*	-
f_{ct} [MPa]	4*	-
Others	Table 2-1 and Table 2-2	-
Aggregates		
Expansion		-
ρ_{agg} [kg/cm^3]	2.55×10^{-3}	(Kelly et al. 1969)
E_{agg} [GPa]	72.4	(Kelly et al. 1969)
υ_{agg}	0.28*	-
α_{agg}^T [10^{-5} / ºC]	6.35 (20-120 ºC)	(Kelly et al. 1969)
Other parameters		
$\frac{E_d}{E_0}$	1/3*	-
$\frac{k_d}{k_0}$	1/10*	-
$\frac{D_d}{D_0}$	10*	-
$\frac{\mathbb{D}_d}{\mathbb{D}_0}$	10*	-

* Assumed values to illustrate sensitivity.

6.3 Results

Figure 6-4 shows the variation of the damage due to nuclear radiation, D_{Rad}, obtained at the first stage of analysis, which is the radio-thermo analysis for neutron, photon, and heat transport. It is the volume fraction of the distressed concrete phase under nuclear irradiation obtained by the multiphase and multiscale model developed in Chapter 2 and Equation **Error! Reference source not found.** in Chapter 4. The profiles of D_{Rad} of the concrete up to 80 years are reported at different times and different depths. As shown in the figure, the damage of concrete due to radiation continues to develop with increasing time, especially for the concrete within the first 20 cm from the inner surface of the wall which is closer to the radiation source. The concrete farther from the radiation source seems to not change significantly with increasing time, and almost shows negligible damage even at 80 years. The damage profile obtained then is applied to the finite element analysis in ABAQUS to represent the radiation damage of concrete.

Figure 6-5 and Figure 6-6 show some results of the three-dimensional radio-thermo-mechanical analysis of the simplified concrete biological shielding wall in NPPs. Figure 6-5 shows the total damage at 80 years which is a combination of the radiation damage and potential mechanical damage during normal NPP operating conditions. Similarly, damage of the concrete due to the radiation continues to develop with increasing time, especially for the concrete material within the first 20 cm from the inner surface of the wall which is closer to the radiation source. The concrete farther from the radiation source has negligible damage. Figure 6-6 shows the total strain in the z-direction at 80 years under normal loadings during the normal NPP operating conditions. The displacement of concrete closer to the neutron source is larger than the displacement of concrete farther from the radiation source. The results suggest that if even a small part of the concrete biological shielding wall deteriorates in a normal NPP operational environment, the structural behavior of the concrete biological shielding wall could change noticeably after a certain age. The degradation of concrete material and its potential effects on the structural capacities of reinforced concrete structures need to be considered when evaluating long-term NPP operation.

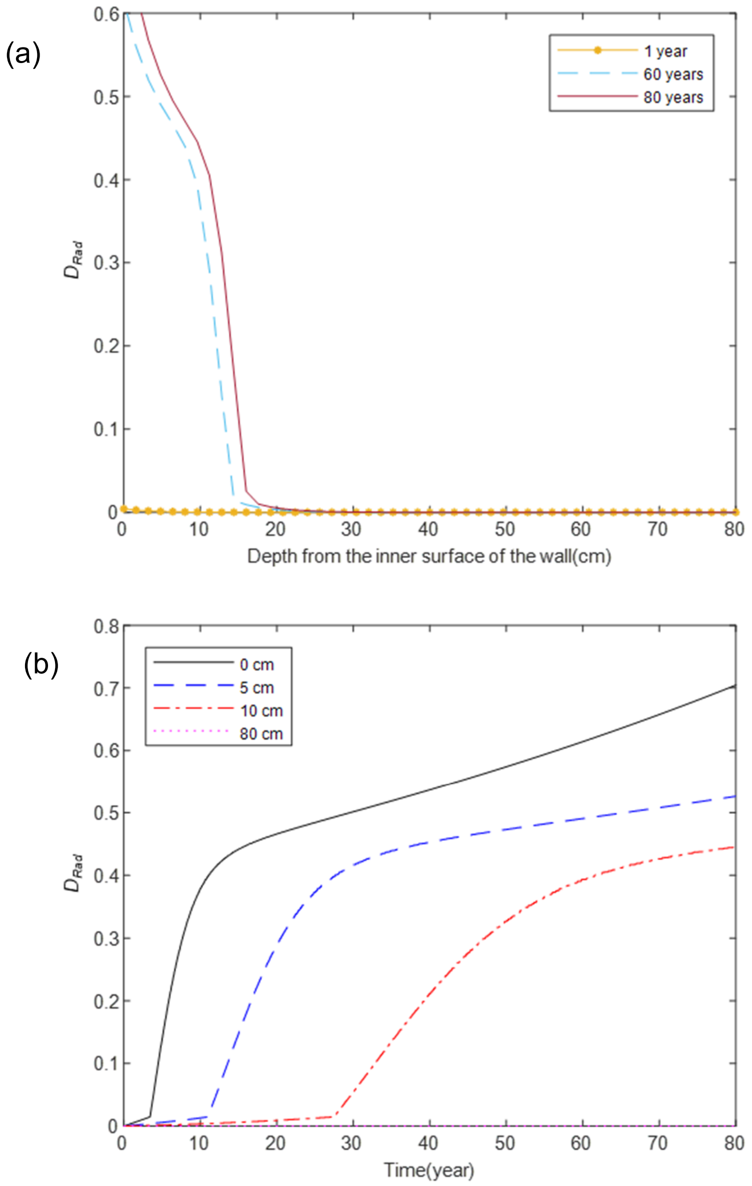

Figure 6-4 Damage progression due to radiation and the temperature (D_{Rad}) up to 80 years: (a) with the depth of concrete at different times; (b) with time at different depths (damage at 80 cm is not noticeable)

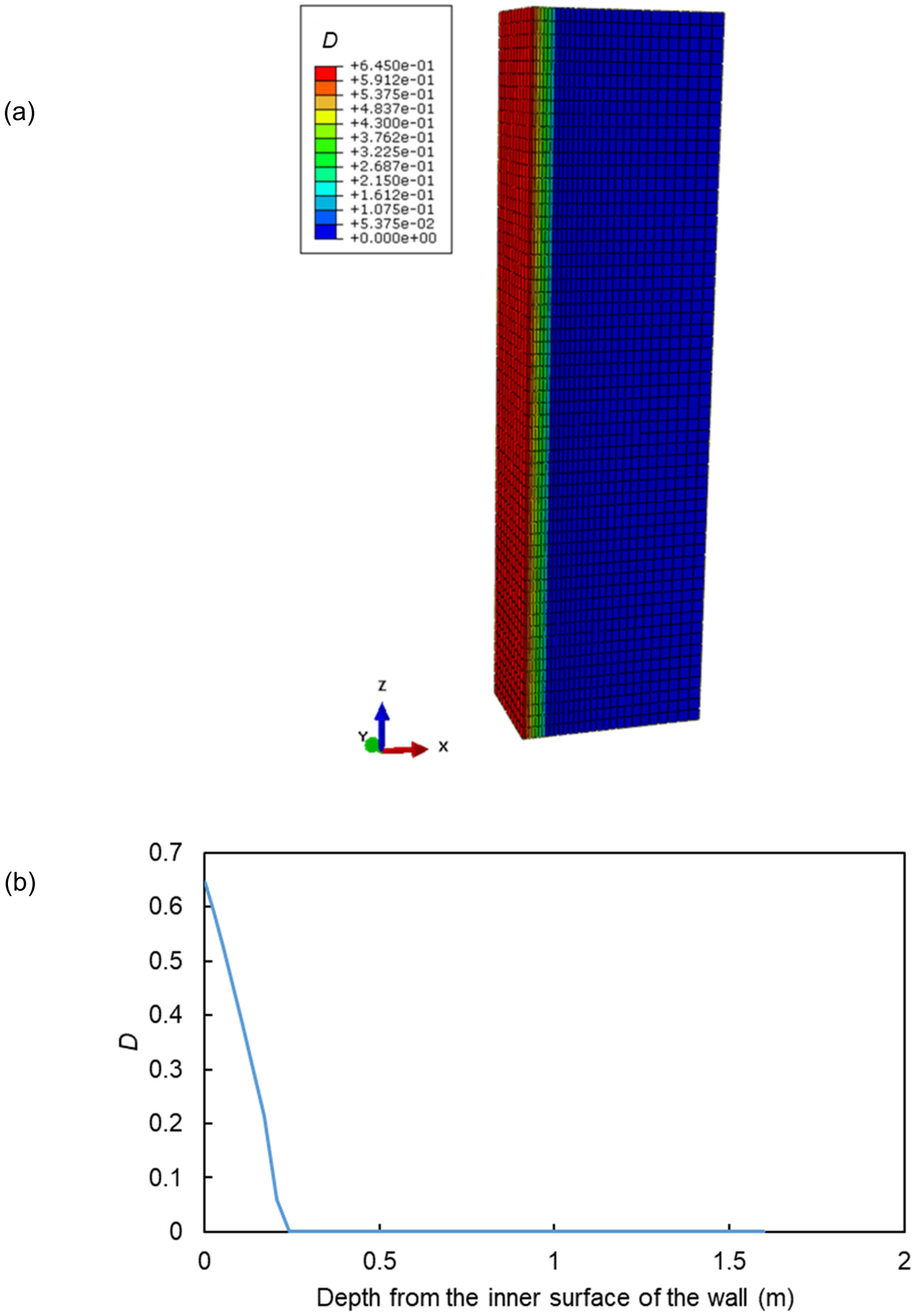

Figure 6-5 Total damage profile at 80 years: (a) whole structure; (b) profile at the middle z plane

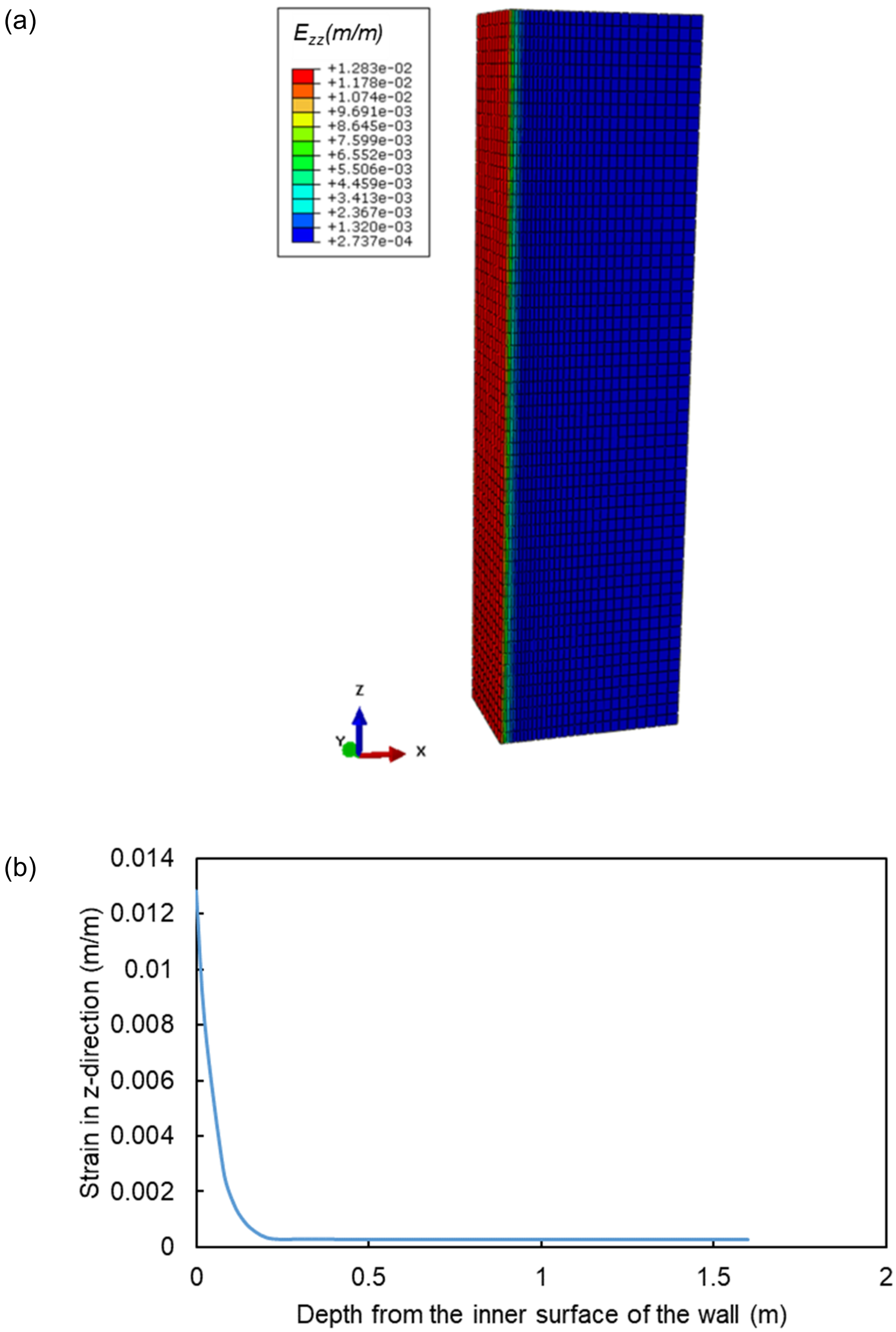

Figure 6-6 Total strain in z-direction at 80 years: (a) whole structure; (b) profile at the middle z plane

7 CONCLUSIONS AND DISCUSSION

7.1 Conclusions

The damage induced by mechanical loading and environmental loads (high/low temperatures, drying/wetting, and chemical reactions) has shown various effects on the mechanical properties of concrete such as strength and stiffness; volumetric properties such as creep, shrinkage, and coefficient of thermal expansion; and transport properties such as the diffusion coefficients of heat conduction, moisture, and chemical transport. Thus, it was a hypothesis that the damage induced by nuclear irradiation has similar effects on the same mechanical, volumetric, and transport properties of concrete. Furthermore, by the same hypothesis, the damage may also have effects on the resistance to neutron and gamma transport in concrete.

This modeling work is an attempt to model the degradation of concrete material under nuclear irradiation and the effect of the degradation on various properties of concrete. It establishes a general framework for integrating various phenomena associated with concrete degradation at different scale levels and constituent phases due to exposure to nuclear irradiation. The results of the project represent one comprehensive model that can be further improved when more test data are available for calibration. More details can be found in Section 7.2.

Constitutive models of plain concrete under nuclear irradiation were developed taking into account the aging and damage effects on both the transport (neutron, gamma rays, and heat) and mechanical properties of concrete. The theoretical models were developed and implemented in finite element and finite difference codes for future application of numerical analysis of concrete and reinforced concrete structures in nuclear power plants.

A theoretical model was developed for the prediction of the modulus of elasticity and deformation of nuclear-irradiated concrete. The model can take into account the degradation mechanisms at multiscale levels and different spatial distributions of the multiphase constituents in concrete. The Mori-Tanaka model and the Generalized Self-Consistent (GSC) model were used to characterize the multiphase internal structure of concrete ranging from the nanometer to the meter scale level. The volume fraction of each constituent phase was calculated based on the concrete mix design and the hydration reactions of Portland cement. The responses of specific constituent phases, such as the aggregate or the cement paste, to nuclear irradiation and temperature at different scale levels were quantitatively characterized based on the collected test data or estimated based on available models. Damage development in the hardened cement paste in the nuclear irradiated concrete was calculated based on composite damage mechanics. The overall irradiation effect on concrete as a composite material can be calculated by considering the effects of the irradiation and temperature on each constituent phase at each scale level. The model was validated preliminarily with experimental data available in the literature for the modulus of elasticity of distressed concrete.

A coupled damage-creep model of nuclear-irradiated concrete is developed based on the generalized Maxwell model and Mazars' damage model. The coupled model was implemented in ABAQUS/standard via a subroutine UMAT. The purpose of using ABAQUS was to consider the effect of mechanical loadings on the concrete. The effect of neutron irradiation and elevated temperature generated by gamma rays is considered by the multiphase and multiscale model.

The transport of neutrons and gamma rays in damaged concrete were calculated using multi-group diffusion equations. The heat equation was also included in the modeling to account for the heat generated by the neutron and gamma radiation. The transport parameters of concrete related to neutron and gamma diffusion as well as heat transfer were modeled using cross-property correlation theory in which the transport parameters of distressed concrete can be determined based on the mechanical properties of the distressed concrete. The degradation of the mechanical properties of distressed concrete by neutron irradiation and elevated temperature was determined by the multiphase and multiscale model. The results obtained from the present diffusion models were compared with the results obtained using the Monte Carlo N-Particle transport code (MCNP 6.2). Good agreements were obtained.

As a comprehensive case study, a coupled radio-thermo-mechanical analysis was conducted using a section of a concrete wall. The case study combined all models developed in this project, including the multiscale and multiphase model for neutron-induced damage, the coupled damage-creep model, and the coupled radio-thermo model for neutron and gamma transport. The case study showed the capability of the models developed in this project, in that they can be used to estimate the long-term mechanical and transport response of concrete, including the state of structural concrete in NPPs under design loading conditions.

7.2 Suggestions for Future Research

Further improvement of the models developed in this project can be made in the following areas:

1) The expansion of various aggregates under nuclear irradiation is the most important factor for the damage of concrete. The multiscale model characterized the concrete, mortar, and cement paste all the way to the nanometer level, but the expansion of aggregates could not be modeled in a similar manner. The response of various mineralogical compositions in different rocks under nuclear irradiation must be studied. This should be an important research topic in the future.

2) The models were developed for properties of concrete and calibrated by available test data obtained from small concrete samples. The models need to be used in structural analysis programs to examine the impact of the nuclear irradiation at the material level on the performance of structures at the meter scale. Several numerical case studies need to be conducted on a typical concrete shielding structure with typical concrete mix designs and typical cements and aggregates used in nuclear power plants in the U.S. This can be done using the present models and the information collected in Biwer et al. (2020). However, data on the concrete-steel bond under irradiation, as well as data on harvested irradiated concrete, are needed to more accurately predict long-term performance. Moreover, further study is needed to understand the behavior and response of the structures exposed to irradiation and subjected to static and dynamic loading during normal operation, design basis seismic events, and accident conditions.

3) The coupled creep-damage model needs to be experimentally calibrated. The present model was calibrated by creep of concrete without nuclear irradiation. There is no test result available on the creep of concrete degraded by nuclear irradiation.

4) The effect of temperature on concrete creep has been experimentally studied, especially in the range of operating temperatures of nuclear power plants (< 65°C). The modeling approach is also available. The temperature effect on concrete creep is not currently implemented in the current creep-damage model but can be done in the future.

5) The multiple group diffusion models for neutron and gamma transport in concrete have not been calibrated with test data. The model results were compared with the predictions by MCNP 6.2, which is not sufficient since the degradation of concrete is not included in MCNP6.2. Nevertheless, the extent of the impact of the damage on the transport properties has not been examined by any systematic experimental study. To gain more insight on the damage effects on radiation diffusion coefficients and thermal conductivities of concrete material, a joint study by experts from both fields is recommended.

6) In order to obtain reliable results through the developed models, critical input parameters need to be well determined. As one can see, some input parameters, such as the group coefficients and macroscopic cross sections for multigroup photon or neutron diffusion problems were assumed or the values from other concrete test results were used during the analysis. For example, as shown in Appendix A.8 for neutron diffusion, those parameters are averaged values for each group and can be only calculated by approximating the neutron flux density. Further study is needed.

7) The aim of the models is structural evaluation of concrete and reinforced concrete structures in nuclear power plants. Currently, the models can only characterize the behavior of concrete. More knowledge or models are needed to evaluate the performance of other materials under nuclear irradiation, such as the behavior of steel bar reinforcement and the associated steel-concrete interaction under nuclear irradiation. Then, a comprehensive structural analysis of reinforced concrete structure in NPPs can be done in commercial software packages, such as ABAQUS.

8) The steel-concrete bond strength is important for analysis of reinforced concrete structures. The bond strength is related to the cement paste in the interface transition zone (ITZ) between the steel and concrete. The characteristics of the ITZ can be described by the multiscale and multiphase model by revising the model properly (for example, the porosity of cement paste in the ITZ is higher than that in the regular cement paste, which can be reflected in the model). The shear strength of the ITZ under nuclear irradiation must be tested, and the test data will be useful for improving the present model and for the numerical analysis at the structural level.

9) The present models can be linked with other available commercial FE software, together or separately. For example, the multiphase and multiscale model developed in Chapter 2 can be used together with ABAQUS with or without combining the coupled damage-creep model developed in Chapter 3 and radiation transport models presented in Chapter 4 and Chapter 5.

10) Uncertainties in the output of the present models come from several sources, such as the deviation of the models from actual mechanisms, the random nature of the material parameters (e.g., water-cement ratio), and the fluctuation of environmental parameters (e.g., relative humidity). The random variables and fluctuating variables can be analyzed

and their impact can be evaluated by using the present models with the random input variables generated from their actual random distribution functions, so the statistical features of the model outputs can be evaluated. With the statistical features of the model output at the material level, the uncertainty of structural analysis at meter scales can be estimated.

11) In order to perform a comprehensive validation of the present models (or any material models), comprehensive experimental studies testing for a section of concrete structure instead of small concrete samples are needed. If possible, the best case would be a section of reinforced concrete structure from a demolished nuclear power plant for model validation. One of the advantages of a reinforced concrete structure from a NPP is that the distressed concrete in the structure has a distribution of neutron and gamma ray irradiation, in which some of the concrete may have high levels of neutron and gamma irradiation. Two types of experimental studies can be performed. The first type is to harvest samples from different locations of the structure, so the mechanical and transport properties of concrete samples with different levels of nuclear irradiation can be examined. This should be a systematic multiscale characterization for concrete, mortar, aggregates, cement paste, and hydration products (e.g., C-S-H) in the cement paste. The test data will provide valuable information for validation of the present model. The second type is to use the structure as a model and apply thermal, hygro, and chemical boundary conditions on the structure. Mechanical loadings and additional nuclear irradiation can also be applied, if possible. Various sensors can be installed on and in the structure to monitor the responses of the structure under the coupled effects of the environmental loadings. This type of test requires a very large hot cell which may or may not be available at the present time and should be considered as an important future development. These test data will provide important information about the structure under various realistic environmental conditions. So, the effect of material degradation induced by nuclear irradiations on the structural performance can be evaluated using the present multiscale and multiphase model together with a finite element model for the structure, which is the ultimate goal for the development of the present model.

8 REFERENCES

Acker, P. (2004). “Swelling, shrinkage and creep: a mechanical approach to cement hydration.” *Materials and Structures*, 37(4), 237–243.

Alexander, M., and Mindess, S. (2005). *Aggregates in Concrete*. CRC Press, Boca Raton, FL.

Bažant, Z. P., and Kaplan, M. F. (1996). *Concrete at high temperatures: material properties and mathematical models*. Longman, Harlow.

Benveniste, Y. (1987). “A new approach to the application of Mori-Tanaka’s theory in composite materials.” *Mechanics of Materials*, 6(2), 147–157.

Biwer, B., Ma, D., Xi, Y., and Jing, Y. (2020). *Review of Radiation-Induced Concrete Degradation and Potential Implications for Structures Exposed to High, Long-Term Radiation Levels in Nuclear Power Plants*, U.S. Nuclear Regulatory Commission, NUREG/CR-xxxx, ANL/EVS-20/8, in press.

Chen, J., X. Jin, J. Nanguo, and Y. Tian. (2014). A nano-model for micromechanics-based elasticity prediction of hardened cement paste. *Magazine of Concrete Research*, 66(22), 1145–1153.

Christensen, Richard M. (2005). *Mechanics of Composite Materials.* Dover Publications.

Constantinides, G., and Ulm, F.-J. (2004). “The effect of two types of CSH on the elasticity of cement-based materials: Results from nanoindentation and micromechanical modeling.” *Cement and Concrete Research*, 34(1), 67–80.

Damien, D., Wang, Y., and Xi, Y. (2019). Prediction of Elastic Properties of Cementitious Materials Based on Multiphase and Multiscale Micromechanics Theory. *Journal of Engineering Mechanics*, *145*(10), 04019074.

DOE Fundamentals Handbook. (1993). *Nuclear Physics and Reactor Theory*. U.S. Department of Energy, Washington, D.C.

Dubrovskii, V. B., Ibragimov, S. S., Kulakovskii, M. Y., Ladygin, A. Y., and Pergamenshchik, B. K. (1967). “Radiation damage in ordinary concrete.” *Soviet Atomic Energy*, 23(4), 1053–1058.

Dubrovskii, V. B., Ibragimov, S. S., Ladygin, A. Y., and Pergamenshchik, B. K. (1966). “Effect of neutron irradiation on some properties of heat-resistant concretes.” *Soviet Atomic Energy*, 21(2), 740–744.

Duderstadt, J. J., and Hamilton, L. J. (1976). *Nuclear reactor analysis*. Wiley, New York.

Elleuch, L. F., Dubois, F., and Rappeneau, J. (1972). “Effects of neutron radiation on special concretes and their components.” *ACI Special Publication*, 34, 1071–1108.

El-Sayed Abdo, A., and Amin, E. (2001). “Distribution of temperature rise in biological shield due to thermal neutrons.” *Annals of Nuclear Energy*, 28(3), 275–283.

Eskandari-Ghadi, M., Xi, Y., and Sture, S. (2014). “Cross-Property Relations between Mechanical and Transport Properties of Composite Materials.” *Journal of Engineering Mechanics*, 140(7).

Eskandari-Ghadi, M., Zhang, W., Xi, Y., and Sture, S. (2013). “Modeling of Moisture Diffusivity of Concrete at Low Temperatures.” *Journal of Engineering Mechanics*, 139(7), 903–915.

Esselman, T., and Bruck, P. (2013). *Expected Condition of Concrete at Age 80 Years of Reactor Operation. Technical Report, A13276-R-001*. Lucius Pitkin, Inc., Amesbury, MA.

Evans, R.D., (1955). *The Atomic Nucleus*. New York: McGraw-Hill, Inc.

Field, K. G., Remec, I., and Le Pape, Y. (2015). “Radiation effects in concrete for nuclear power plants – Part I: Quantification of radiation exposure and radiation effects.” *Nuclear Engineering and Design*, 282, 126–143.

Hilsdorf, H., Kropp, J., and Koch, H. (1978). “The effects of nuclear radiation on the mechanical properties of concrete.” *ACI Special Publication*, 55, 223–254.

Hogerton, J. F., & Grass, R. C. (1953). *THE REACTOR HANDBOOK. VOL. 1. PHYSICS* (No. AECD-3645). Atomic Energy Commission, Washington, DC.

Hubbell, J. H., and Seltzer, S. M. (1995). *Tables of X-ray mass attenuation coefficients and mass energy-absorption coefficients 1 keV to 20 MeV for elements Z= 1 to 92 and 48 additional substances of dosimetric interest* (No. PB-95-220539/XAB; NISTIR-5632). National Inst. of Standards and Technology-PL, Gaithersburg, MD (United States). Ionizing Radiation Div..

Jing, Y., and Xi, Y. (2017) “Theoretical Modeling of the Effects of Neutron Irradiation on Properties of Concrete”, *J. Eng. Mech.,* ASCE, 143(12), 04017137, 1-14.

Kelly, B. T., Brocklehurst, J. E., Mottershead, D., McNearney, S., and Davidson, I. (1969). “Effects of Reactor Radiation on Concrete.” Commision of the European Communities, Brussels, 237–265.

Kodur V. K. R., and Sultan M. A. (2003). “Effect of Temperature on Thermal Properties of High-Strength Concrete.” *Journal of Materials in Civil Engineering*, 15(2), 101–107.

Lee, J. (2006). “Experimental studies and theoretical modeling of concrete subjected to high temperatures.” Ph.D. Thesis, University of Colorado at Boulder, Boulder, CO.

Kontani, O., Ichikawa, Y., Ishizawa, A., Takizawa, M., and Sato, O. (2014). “Irradiation Effects on Concrete Structures.” *Infrastructure Systems for Nuclear Energy*, T. T. C. Hsu, C.-L. Wu, and J.-L. Li, eds., John Wiley & Sons, Ltd, Chichester, UK, 459–473.

Lee, J., Xi, Y., Willam, K., and Jung, Y. (2009). “A multiscale model for modulus of elasticity of concrete at high temperatures.” *Cement and Concrete Research*, 39(9), 754–762.

Maienschein, F. C., Peelle, R. W., Zobel, W., and Love, T. A. (1958). *Gamma rays associated with fission (No. A/CONF. 15/P/670)*. Oak Ridge National Lab., TN.

Maruyama, I., Haba, K., Sato, O., Ishikawa, S., Kontani, O., and Takizawa, M. (2016). “A Numerical Model for Concrete Strength Change under Neutron and Gamma-ray Irradiation.” *Journal of Advanced Concrete Technology*, 14(4), 144–162.

Maruyama, I., Kontani, O., Takizawa, M., Sawada, S., Ishikawao, S., Yasukouchi, J., Sato, O., Etoh, J., and Igari, T. (2017). “Development of Soundness Assessment Procedure for Concrete Members Affected by Neutron and Gamma-Ray Irradiation.” *Journal of Advanced Concrete Technology*, 15(9), 440–523.

Mazars, J. (1986). “A description of micro- and macroscale damage of concrete structures.” *Engineering Fracture Mechanics*, 25(5), 729–737.

Mazars, J., and Pijaudier-Cabot, G. (1989). “Continuum Damage Theory—Application to Concrete.” *Journal of Engineering Mechanics*, 115(2), 345–365.

Meshgin, P., and Xi, Y. (2013). “Multi-scale composite models for the effective thermal conductivity of PCM-concrete.” *Construction and Building Materials*, 48, 371–378.

Monteiro, P. J., & Chang, C. T. (1995). The elastic moduli of calcium hydroxide. *Cement and Concrete Research*, *25*(8), 1605–1609.

Mori, T., and Tanaka, K. (1973). “Average stress in matrix and average elastic energy of materials with misfitting inclusions.” *Acta Metallurgica*, 21(5), 571–574.

Naus, D.J., 2007, *Primer on Durability of Nuclear Power Plant Reinforced Concrete Structures - A Review of Pertinent Factors*, NUREG.CR-6927, prepared by Oak Ridge National Laboratory, for the U.S.Nuclear Regulatory Commission, Washington, DC, February.

Neubauer, C. M., Jennings, H. M., and Garboczi, E. J. (1996). “A three-phase model of the elastic and shrinkage properties of mortar.” *Advanced Cement Based Materials*, 4(1), 6–20.

NRC, U.S. Nuclear Regulatory Commission, 2010, *Standard Review Plan for Review of License Renewal Applications for Nuclear Power Plants,* NUREG-1800, Rev. 2, Office of Nuclear Reactor Regulation, Washington, DC.

NRC, U.S. Nuclear Regulatory Commission, 2017, *Standard Review Plan for Review of Subsequent License Renewal Applications for Nuclear Power Plants, NUREG-2192*, Office of Nuclear Reactor Regulation, Washington, DC. ADAMS Accession No. ML17188A158.

Pan, J., Zou, R., and Jin, F. (2016). “Experimental Study on Specific Heat of Concrete at High Temperatures and Its Influence on Thermal Energy Storage.” *Energies*, 10(1), 33.

Pijaudier-Cabot, G., and Mazars, J. (2001). Damage Models for Concrete, *in* J. Lemaite (ed.), *Handbook of Material Behaviour Models*, Academic Press, pp. 500–512.

Pomaro, B., Salomoni, V. A., Gramegna, F., Prete, G., and Majorana, C. E. (2011a). “Radiation damage evaluation on concrete within a facility for Selective Production of Exotic Species (SPES Project), Italy.” *Journal of Hazardous Materials*, 194, 169–177.

Pomaro, B., Salomoni, V. A., Gramegna, F., Prete, G., and Majorana, C. E. (2011b). “Radiation damage evaluation on concrete shielding for nuclear physics experiments.” *Annals of Solid and Structural Mechanics*, 2(2–4), 123–142.

Price, B. T., Horton, C. C., and Spinney, K. T. (1957). *Radiation shielding*. Pergamon Press, London.

REACTOR PHYSICS CONSTANTS. (1963). ANL-5800 (2nd Ed.), Argonne National Laboratory, Argonne, IL.

Remec, I., Rosseel, T. M., Field, K. G., and Pape, Y. L. (2016). “Characterization of Radiation Fields in Biological Shields of Nuclear Power Plants for Assessing Concrete Degradation.” *EPJ Web of Conferences*, 106.

Rosen, B. W., and Hashin, Z. (1970). “Effective thermal expansion coefficients and specific heats of composite materials.” *International Journal of Engineering Science*, 8(2), 157–173.

Shultis, J. K., and Faw, R. E. (1996). *Radiation shielding*. Prentice Hall PTR, Upper Saddle River, NJ.

Speziale, S., Jiang, F., Mao, Z., Monteiro, P. J., Wenk, H. R., Duffy, T. S., and Schilling, F. R. (2008). "Single-crystal elastic constants of natural ettringite." *Cement and Concrete Research*, *38*(7), 885-889.

Stora, E., He, Q. C., and Bary, B. (2006). "Influence of inclusion shapes on the effective linear elastic properties of hardened cement pastes." Cement and Concrete Research, 36(7), 1330-1344.

Taylor, H. F. (1997). *Cement chemistry, 2nd ed.*, Thomas Telford, London.

Termkhajornkit, P., Vu, Q. H., Barbarulo, R., Daronnat, S., and Chanvillard, G. (2014). "Dependence of compressive strength on phase assemblage in cement pastes: Beyond gel–space ratio—Experimental evidence and micromechanical modeling." *Cement and Concrete Research*, *56*, 1-11.

Townsend, B. D. (2003). Creep and shrinkage of a high strength concrete mixture (Doctoral dissertation, Virginia Tech).

Ursu, I. (1985). *Physics and Technology of Nuclear Materials*. Pergamon Press, Oxford, UK.

Vandamme, M., Ulm, F. J., and Fonollosa, P. (2010). "Nanogranular packing of C–S–H at substochiometric conditions." *Cement and Concrete Research*, *40*(1), 14-26.

Vandamme, M., and Ulm, F. J. (2009). "Nanogranular origin of concrete creep." *Proceedings of the National Academy of Sciences*, *106*(26), 10552-10557.

Velez, K., Maximilien, S., Damidot, D., Fantozzi, G., and Sorrentino, F. (2001). "Determination by nanoindentation of elastic modulus and hardness of pure constituents of Portland cement clinker." *Cement and Concrete Research*, 31(4), 555-561.

Wang, S. X., Wang, L. M., and Ewing, R. C. (2000). “Irradiation-induced amorphization: Effects of temperature, ion mass, cascade size, and dose rate.” *Physical Review B*, 63(2).

Weber, W. J., Ewing, R. C., Catlow, C. R. A., De La Rubia, T. D., Hobbs, L. W., Kinoshita, C., Matzke, H., Motta, A. T., Nastasi, M., Salje, E. K. H., and others. (1998). “Radiation effects in crystalline ceramics for the immobilization of high-level nuclear waste and plutonium.” *Journal of Materials Research*, 13(06), 1434–1484.

Weber, W. J., Ewing, R. C., and Wang, L.-M. (1994). “The radiation-induced crystalline-to-amorphous transition in zircon.” *Journal of Materials Research*, 9(03), 688–698.

Werner, C. J., et al., "MCNP6.2 Release Notes," Los Alamos National Laboratory, report LA-UR-18-20808 (2018).

Willam, K., Xi, Y., Lee, K., and Kim, B. (2009). “Thermal Response of Reinforced Concrete Structures in Nuclear Power Plants”, University of Colorado at Boulder, SESM Report No. 02-2009.

William, K., Xi, Y., and Naus, D. (2013). *A review of the effects of radiation on microstructure and properties of concretes used in nuclear power plants (NUREG/CR-7171)*. Office of Nuclear Regulatory Research, U.S. Nuclear Regulatory Commission, Washington, DC.

Xi, Y., and Jennings, H. M. (1997). “Shrinkage of cement paste and concrete modelled by a multiscale effective homogeneous theory.” *Materials and Structures*, 30(6), 329–339.

Xi, Y., Eskandari-Ghadi, M., Suwito, and Sture, S. (2006). “Damage theory based on composite mechanics.” *Journal of engineering mechanics*, 132(11), 1195–1204.

Xi, Y., Willam, K., and Frangopol, D. (2000). “Multiscale Modeling of Interactive Diffusion Processes of Concrete,” *Journal of Engineering Mechanics*, ASCE, 126(3), 258–265.

Yevick, J. G. (1966). *Fast Reactor Technology: Plant Design*. M.I.T. Press, Cambridge, MA.

Zohdi, T. I., Monteiro, P. J. M., and Lamour, V. (2002). “Extraction of elastic moduli from granular compacts.” *International journal of fracture*, *115*(3), 49-54.

APPENDIX A

A.1 Generalized Self-Consistent Model

For any phase *i* (*i* = 1 is inclusion and *i* = 2 is matrix) in the composite material shown in Figure **2-3** (c) that deforms, the elastic equilibrium equation in spherical coordinates is given as

$$U_{i,rr} + \frac{2}{r} U_{i,r} - \frac{2}{r^2} U_i - \frac{1+v_i}{1-v_i} \varepsilon_{i,r} = 0 \tag{A-1}$$

where

U_i = displacement of phase *i* in the radial direction (cm),

r = the location coordinate in the radial direction when the center of the inclusion is the origin of the system (cm),

v_i = Poisson's ratio for phase *i* (unitless), and

ε_i = the linear strain for phase *i* (unitless).

$U_{i,r}$ is the derivative of U_i with respect to *r*, where the comma is common tensor notation for a derivative and $U_{i,rr}$ is the second derivative of U_i with respect to *r*.

Since a very small scale deformation is considered, the last term in the above equation can be neglected. Thus, the equation can be simplified to

$$U_{i,rr} + \frac{2}{r} U_{i,r} - \frac{2}{r^2} U_i = 0. \tag{A-2}$$

The above equation is the basic differential equation of the problem shown in Figure 2-3 (c). $U_{i1}(r) = r$ is one solution of this second-order linear differential equation. A second solution that is linearly independent of the first solution can be obtained using the reduction of order method. The second solution is in the form:

$$U_{i2}(r) = v(r)U_{i1}(r) = v(r)r \tag{A-3}$$

where *v*(*r*) is an arbitrary function.

Substitute $U_{i2}(r)$ into Equation (A-2) to get

$$rv_{,rr} + 2v_{,r} + \frac{2}{r}\left(rv_{,r} + v\right) - \frac{2}{r} v = 0 \tag{A-4}$$

Rearranging the above equation, then

$$v_{,rr} + \frac{4}{r} v_{,r} = 0 \tag{A-5}$$

which is a first-order equation for $w = v_{,r}$, given by

$$w_{,r} + \frac{4}{r} w = 0 \tag{A-6}$$

which can be easily solved by method of separation of variables

$$w = c_1 r^{-4},\ c_1 \in \mathbb{R} \tag{A-7}$$

Integrating the equation above, *v* is obtained

$$v = c_2 r^{-3} + c_3, c_2, c_3 \in \mathbb{R} \tag{A-8}$$

Then

$$U_{i2}(r) = v(r)r = c_2 r^{-2} + c_3 r, \qquad c_2, c_3 \in \mathbb{R} \tag{A-9}$$

When $c_2 = 0$ and $c_3 = 1$, $U_{i2}(r) = r$ which is $U_{i1}(r)$. Based on the principle of superposition, $U_{i2}(r)$ shown in Equation (A-9) is the general solution of Equation (A-2).

Based on Hooke's law for an isotropic material, the expressions of displacements and corresponding stresses valid in all phases can be obtained

$$U_i = C_i r + \frac{D_i}{r^2} \tag{A-10}$$

$$\sigma_{ri} = 3K_i C_i - 4G_i \frac{D_i}{r^3} - 3K_i \varepsilon_i \tag{A-11}$$

where

σ_{ri} = the stress of phase *i* in the radial direction (MPa),

K_i = bulk modulus of phase *i* (MPa),

G_i = shear modulus of phase *i* (MPa)

C_i are unknown coefficient (unitless), and

D_i are unknown coefficient (cm^3), $D_1 = 0$ to avoid a singularity at $r = 0$.

Apply continuity conditions at $r = R_1$, which is $U_1(R_1) = U_2(R_1)$ and $\sigma_{r1}(R_1) = \sigma_{r2}(R_1)$ and assume the displacement along the radial direction at boundary $r = R_2$ is δ, then we have

$$C_1 R_1 = C_2 R_1 + \frac{D_2}{{R_1}^2} \tag{A-12}$$

$$3K_1 C_1 - 3K_1 \varepsilon_1 = 3K_2 C_2 - 4G_2 \frac{D_2}{{R_1}^3} - 3K_2 \varepsilon_2 \tag{A-13}$$

$$U_2(R_2) = C_2 R_2 + \frac{D_2}{{R_2}^2} = \delta \tag{A-14}$$

Then, the three unknown coefficients C_1, C_2, and D_2 can be solved through the three equations shown above.

$$C_1 = \frac{\delta}{R_2} - \frac{D_2}{{R_2}^3} + \frac{D_2}{{R_1}^3} \tag{A-15}$$

$$C_2 = \frac{\delta}{R_2} - \frac{D_2}{{R_2}^3} \tag{A-16}$$

$$D_2 = \frac{3K_1\varepsilon_1 - 3K_2\varepsilon_2 + \frac{3\delta}{R_2}(K_2 - K_1)}{3K_1\left(\frac{1}{{R_1}^3} - \frac{1}{{R_2}^3}\right) + \frac{3K_2}{{R_2}^3} + \frac{4G_2}{{R_1}^3}} \tag{A-17}$$

Equation (A-10) and Equation (A-11) are also valid for the effective medium. For the effective medium and the matrix sphere, the displacement and stress should be the same at boundary $r = R_2$, respectively. Therefore, $U_{eff}(R_2) = U_2(R_2)$ and $\sigma_{reff}(R_2) = \sigma_{r2}(R_2)$ which is

$$C_{eff}R_2 = \delta \tag{A-18}$$

$$3K_{eff}C_{eff} - 3K_{eff}\varepsilon_{eff} = 3K_2C_2 - 4G_2\frac{D_2}{{R_2}^3} - 3K_2\varepsilon_2 \tag{A-19}$$

where the subscript *eff* stands for effective medium. Solve C_{eff} from Equation (A-18) and substitute it into Equation (A-19) to get

$$3K_{eff}\frac{\delta}{R_2} - 3K_{eff}\varepsilon_{eff} = 3K_2C_2 - 4G_2\frac{D_2}{{R_2}^3} - 3K_2\varepsilon_2 \tag{A-20}$$

First, take all strains, ε_1, ε_2, and ε_{eff} to be zero, and all the equations are still valid, then K_{eff} can be solved from Equation (A-20)

$$K_{eff} = K_2 + \frac{f_1(K_1 - K_2)}{1 + (1 - f_1)\frac{K_1 - K_2}{K_2 + \frac{4}{3}G_2}} \tag{A-21}$$

Alternative form:

$$\frac{K_{eff}}{K_2} = 1 + \frac{d(\frac{K_1}{K_2} - 1)}{1 + (1 - d)\frac{\frac{K_1}{K_2} - 1}{1 + \frac{4}{3}\frac{G_2}{K_2}}}$$

where $f_1 = \frac{R_1^3}{R_2^3}$, the volume fraction of phase 1 (inclusion). By substituting K_{eff} into Equation (A-20), the strain of the effective medium is obtained

$$\varepsilon_{eff} = \frac{K_1\varepsilon_1 f_1(3K_2 + 4G_2) + K_2\varepsilon_2(1 - f_1)(3K_1 + 4G_2)}{K_2(3K_1 + 4G_2) - 4f_1G_2(K_2 - K_1)} \tag{A-22}$$

Apply free boundary condition in the radial direction at boundary *r* = *R*₂, which is

$$\sigma_{r2}(R_2) = 3K_2C_2 - 4G_2\frac{D_2}{{R_2}^3} - 3K_2\varepsilon_2 = 0 \tag{A-23}$$

Substitute C_2 and D_2, which are expressed in terms of δ, into the above equation, and the displacement δ can be solved. Then it is inserted into C_2, D_2, and the following equation to get the radial stress at $r = R_1$

$$\sigma_{r2}(R_1) = 3K_2C_2 - 4G_2\frac{D_2}{{R_1}^3} - 3K_2\varepsilon_2 \tag{A-24}$$

which is the internal pressure *P* at the inclusion-matrix interface of the composite material shown in Figure 2-3 (c)

$$P = \frac{12K_1K_2G_2(1-f_1)}{K_2(3K_1+4G_2) - 4f_1G_2(K_2-K_1)}(\varepsilon_1 - \varepsilon_2) \tag{A-25}$$

The effective shear modulus can be obtained through the equations shown below (the detailed derivations can be found in Section 2.4 from page 53 to page 57 in Christensen (2005)).

$$C_1\left(\frac{G_{eff}}{G_2}\right)^2 + 2C_2\left(\frac{G_{eff}}{G_2}\right) + C_3 = 0 \tag{A-26}$$

where

$$\begin{aligned}
C_1 &= 8\left(\frac{G_1}{G_2}-1\right)(4-5\upsilon_2)\eta_1 d^{\frac{10}{3}} - 2\left[63\left(\frac{G_1}{G_2}-1\right)\eta_2 + 2\eta_1\eta_3\right]d^{\frac{7}{3}} + 252\left(\frac{G_1}{G_2}-1\right)\eta_2 d^{\frac{5}{3}} \\
&\quad - 50\left(\frac{G_1}{G_2}-1\right)(7-12\upsilon_2+8{\upsilon_2}^2)\eta_2 d + 4(7-10\upsilon_2)\eta_2\eta_3 \\
C_2 &= -2\left(\frac{G_1}{G_2}-1\right)(1-5\upsilon_2)\eta_1 d^{\frac{10}{3}} + 2\left[63\left(\frac{G_1}{G_2}-1\right)\eta_2 + 2\eta_1\eta_3\right]d^{\frac{7}{3}} - 252\left(\frac{G_1}{G_2}-1\right)\eta_2 d^{\frac{5}{3}} \\
&\quad + 75\left(\frac{G_1}{G_2}-1\right)(3-\upsilon_2)\eta_2\upsilon_2 d + \frac{3}{2}(15\upsilon_2-7)\eta_2\eta_3 \\
C_3 &= 4\left(\frac{G_1}{G_2}-1\right)(5\upsilon_2-7)\eta_1 d^{\frac{10}{3}} - 2\left[63\left(\frac{G_1}{G_2}-1\right)\eta_2 + 2\eta_1\eta_3\right]d^{\frac{7}{3}} + 252\left(\frac{G_1}{G_2}-1\right)\eta_2 d^{\frac{5}{3}} \\
&\quad + 25\left(\frac{G_1}{G_2}-1\right)({\upsilon_2}^2-7)\eta_2 d - (7+5\upsilon_2)\eta_2\eta_3
\end{aligned}$$

$$\begin{aligned}
\eta_1 &= (49-50\upsilon_1\upsilon_2)\left(\frac{G_1}{G_2}-1\right) + 35\frac{G_1}{G_2}(\upsilon_1-2\upsilon_2) + 35(2\upsilon_1-\upsilon_2) \\
\eta_2 &= 5\upsilon_1\left(\frac{G_1}{G_2}-8\right) + 7\left(\frac{G_1}{G_2}+4\right) \\
\eta_3 &= \frac{G_1}{G_2}(8-10\upsilon_2) + 7 - 5\upsilon_2
\end{aligned}$$

Young’s modulus *E* can be expressed in terms of *K* and *G*:

$$E = \frac{9KG}{3K + G} \tag{A-27}$$

Then, the effective Young’s modulus E_{eff} can be obtained

$$E_{eff} = \frac{9K_{eff}G_{eff}}{3K_{eff} + G_{eff}} \tag{A-28}$$

Or it can be directly calculated from several input parameters as shown below

$$\begin{aligned}\frac{E_{eff}}{E_2} &= \frac{\frac{9K_{eff}G_{eff}}{3K_{eff} + G_{eff}}}{\frac{9K_2G_2}{3K_2 + G_2}} = \frac{K_{eff}}{K_2}\frac{G_{eff}}{G_2}\frac{3K_2 + G_2}{3K_{eff} + G_{eff}} = \frac{K_{eff}}{K_2}\frac{G_{eff}}{G_2}\frac{3 + \frac{G_2}{K_2}}{3\frac{K_{eff}}{K_2} + \frac{G_{eff}}{K_2}} \\ &= \frac{K_{eff}}{K_2}\frac{G_{eff}}{G_2}\frac{3 + \frac{G_2}{K_2}}{3\frac{K_{eff}}{K_2} + \frac{G_{eff}}{G_2}\frac{G_2}{K_2}} = \frac{K_{eff}}{K_2}\frac{G_{eff}}{G_2}\frac{3 + \frac{3(1 - 2v_2)}{2(1 + v_2)}}{3\frac{K_{eff}}{K_2} + \frac{G_{eff}}{G_2}\frac{3(1 - 2v_2)}{2(1 + v_2)}}\end{aligned} \tag{A-29}$$

where

$$\frac{K_1}{K_2} = \frac{\frac{E_1}{3(1 - 2v_1)}}{\frac{E_2}{3(1 - 2v_2)}} = \frac{E_1}{E_2}\frac{1 - 2v_2}{1 - 2v_1} \tag{A-30}$$

$$\frac{G_1}{G_2} = \frac{\frac{E_1}{2(1 + v_1)}}{\frac{E_2}{2(1 + v_2)}} = \frac{E_1}{E_2}\frac{1 + v_2}{1 + v_1} \tag{A-31}$$

$$\frac{G_2}{K_2} = \frac{3(1 - 2v_2)}{2(1 + v_2)} \tag{A-32}$$

Therefore, the parameters needed in order to obtain $\frac{E_{eff}}{E_2}$ are

$$\frac{E_1}{E_2}, v_1, v_2 \tag{A-33}$$

A.2 Fractions of the Phases in Hardened Cement Paste

The volume fractions of each constituent phase in hardened cement paste can be evaluated as follows (Xi and Jennings 1997):

$$f_{clinker} = b\frac{(1-\alpha)}{\rho_c}p \tag{A-34}$$

$$f'_{CH} = b(0.189\alpha_{C_3S}W_{C_3S} + 0.058\alpha_{C_2S}W_{C_2S})p \tag{A-35}$$

$$f_{CSH\,solid} = b\big(0.278\alpha_{C_3S}W_{C_3S} + 0.369\alpha_{C_2S}W_{C_2S}\big)p \tag{A-36}$$

$$f_{gel\,pores} = 0.219f_{CSH\,solid} \tag{A-37}$$

$$f_{AFm} = b\big(0.849\alpha_{C_3A}W_{C_3A} + 0.472\alpha_{C_4AF}W_{C_4AF}\big)p \tag{A-34}$$

$$\begin{gathered} f_{cap} = (1-b-b\Omega)p, \\ \Omega = 0.437\alpha_{C_3S}W_{C_3S} + 0.503\alpha_{C_2S}W_{C_2S} + 0.397\alpha_{C_3A}W_{C_3A} + \\ 0.136\alpha_{C_4AF}W_{C_4AF} \end{gathered} \tag{A-35}$$

$$f_{CSH} = f_{gel\,pores} + f_{CSH\,solid} \tag{A-40}$$

$$f_{AFt} = 1 - \big(f_{Clinker} + f_{CH} + f_{AFm} + f_{cap} + f_{CSH}\big) \tag{A-41}$$

$$f_{LD\,CSH} = 0.7f_{CSH} \tag{A-42}$$

$$f_{HD\,CSH} = 0.3f_{CSH} - f_{UHD\,CSH} \tag{A-43}$$

$$\begin{gathered} f_{UHD\,CSH} = 0.2f_{CSH},\, f_{\text{nanoCH}} = 0.83 * 0.76f_{\text{UHD CSH}} \quad (0.2 < \text{w/c} \le 0.4) \\ f_{UHD\,CSH} = 0,\, f_{nanoCH} = 0 \quad (\text{w/c} > 0.4) \\ f_{CH} = f'_{CH} - f_{\text{nanoCH}} \end{gathered} \tag{A-44}$$

$$b = \frac{1}{1+w/c};\ p = \rho_c\frac{1+w/c}{1+w/c\,\frac{\rho_c}{\rho_w}} \tag{A-45}$$

where

α = overall degree of hydration of Portland cement (calculation method can be found in Appendix A.3

α_i = degree of hydration for reacting compound *i* in Portland cement (unitless) (*i* = C_3S, C_2S, C_3A, *or* C_4AF) (calculation method can be found in Appendix A.3

W_i = weight fraction for reacting compound *i* in Portland cement (unitless), depending on the type of cement used for the concrete (can be found in ASTM C150 for Portland cement),

w/c = water-to-cement ratio (unitless), and

ρ_c = cement density (g/cm^3), and

ρ_w = water density (g/cm^3).

A.3 Hydration Model of Portland Cement

The Avrami equations (Taylor 1987) are employed to approximate the individual degree of hydration for each reacting compound as given by

$$\alpha_i = 1 - exp[-a_i(t - b_i)^{c_i}] \tag{A-36}$$

where

t = time (days) and

a_i, b_i, c_i, = coefficients with values listed in Table A-1.

Table A-1 Coefficients a_i, b_i, and c_i

Compound	a_i	b_i	c_i
C_3S	0.25	0.90	0.70
C_2S	0.46	0.00	0.12
C_3A	0.28	0.90	0.77
C_3AF	0.26	0.90	0.55

Based on the individual degrees of hydration for reacting compounds, the overall degree of hydration of the cement-based material can be obtained from

$$\alpha = \frac{\sum_i W_i \alpha_i}{\sum_i W_i} \tag{A-47}$$

A.4 Determination of the Yield Surface of Cement Paste

The Drucker-Prager plasticity failure criterion is adopted as the criterion for cement paste damage

$$\alpha I_1 + \sqrt{J_2} = k \tag{A-48}$$

where

I_1 = first invariant of the stress tensor (MPa),

J_2 = second invariant of the deviatoric stress tensor (MPa^2),

α,k = constants in terms of the tensile strength (f_t) and compressive strength (f_c') of cement paste

$$\alpha = \left(\frac{1}{\sqrt{3}}\right)(f_c{}' - f_t)/(f_t + f_c{}')$$

$$k = \left(\frac{2}{\sqrt{3}}\right)(f_c{}' f_t)/(f_t + f_c{}')$$

The above equation can be rewritten in terms of principle stresses as

$$\alpha(\sigma_1 + \sigma_2 + \sigma_2) + \sqrt{\frac{1}{6}[(\sigma_1 - \sigma_2)^2 + (\sigma_1 - \sigma_3)^2 + (\sigma_3 - \sigma_2)^2]} = k \qquad \text{(A-37)}$$

In the case of a spherical aggregate, the distribution of radial and tangential stresses in the cement paste are

$$\text{Radial stress} \quad \sigma_r = -P\frac{r_s^3}{r^3} \qquad \text{(A-50)}$$

$$\text{Tangential stress} \quad \sigma_\theta = \sigma_\phi = P\frac{r_s^3}{2r^3} \qquad \text{(A-51)}$$

Where r_s is the aggregate radius (cm). By substituting Equations (A-50) and (A-51) into Equation (A-37), the value for the P that can lead to cement paste damage can be solved

$$P = \left(\frac{r^3}{r_s^3}\right)\frac{4f_c{}' f_t}{3(f_t + f_c{}')} \qquad \text{(A-52)}$$

When the cement paste in the vicinity of aggregates starts to undergo plastic yielding ($r = r_s$), the critical interface pressure (P_c) for the plastic yielding initiation of cement paste is obtained

$$P_c = \frac{4f_c{}' f_t}{3(f_t + f_c{}')} \qquad \text{(A-53)}$$

Once P_c is reached, the cement paste surrounding the aggregate will undergo plastic yielding, with a small increase ΔP in P with time. As shown in Figure 2-13 (a), the thickness of the potential cracked zone is Δx in the radial direction. In this case, the new interface pressure is $P = P_c + \Delta P$ and the new yield surface of the cement paste *is* $r = r_s + \Delta x$. Substituting the new P and r into Equation (A-53), the ratio between Δx and r_s is

$$\frac{\Delta x}{r_s} = \sqrt[3]{1 + \frac{3\Delta P(f_t + f_c{}')}{4f_c{}' f_t}} - 1 \qquad \text{(A-54)}$$

The new yield surface of the cement paste has a radius

$$r = r_s + \Delta x = r_s\sqrt[3]{1 + \frac{3\Delta P(f_t + f_c{}')}{4f_c{}' f_t}} \qquad \text{(A-55)}$$

This process can be repeated with the change of pressure P along time. Therefore, a recursive equation describing the radius of yield surface of the cement paste at time t_n can be obtained

$$r_{n+1} = r_n + \Delta x_n = r_n \sqrt[3]{1 + \frac{3\Delta P_n(f_t + f_c{}')}{4 f_c{}' f_t}} \tag{A-56}$$

A.5 Analytical Solution of Linear One-Dimensional One-Speed Neutron Diffusion Equation with Specific I.C. and B.C.s

The governing equation is shown below ($S(x,t) = 0$).

$$\frac{1}{v}\frac{\partial \phi(x,t)}{\partial t} - \boldsymbol{\nabla} \cdot \mathcal{D}(x)\boldsymbol{\nabla}\phi(x,t) + \Sigma_a(x)\phi(x,t) = 0 \tag{A-57}$$

Apply this partial differential equation (PDE) to a shielding wall with thickness *L* suffering neutron radiation from an external source. The properties do not change with time which means all coefficients are constants. The initial condition (I.C.) and boundary conditions (B.C.s) are shown as follows

I.C.: $\phi(x,0) = 0$ (A-38)

B.C.s: $\phi(0,t) = R$ (a constant value), $\phi(L,t) = 0$ (A-39)

The problem is a nonhomogeneous PDE with nonhomogeneous B.C.s. First, homogenization of the B.C.s is made by using a simple reference function w(x) = -*R*/*L*(*x* - *L*). Take

$$\phi(x,t) = u(x,t) + w(x),\ w(x) = -\tfrac{R}{L}(x - L) \tag{A-60}$$

Then the equation is converted into a PDE in terms of *u*(*x*, *t*) with homogeneous B.C.s

$$\frac{\partial u(x,t)}{\partial t} = a^2 \frac{\partial^2 u(x,t)}{\partial x^2} - bu(x,t) - bw(x) \tag{A-61}$$

I.C.: $u(x,0) = -w(x)$

B.C.s: $u(0,t) = 0,\ u(L,t) = 0$

where $\mathrm{a} = \sqrt{\mathcal{D}v}, b = \Sigma_a v$. A related homogeneous problem with homogeneous B.C.s is

$$\frac{\partial u(x,t)}{\partial t} = a^2 \frac{\partial^2 u(x,t)}{\partial x^2} \tag{A-62}$$

B.C.s: $u(0,t) = 0,\ u(L,t) = 0$

which has eigenvalues $\lambda_n = \left(\frac{n\pi}{L}\right)^2$ ($n = 1,2,\dots$) with associated eigenfunctions $X(x) = sin\frac{n\pi x}{L}$. Thus, the eigenfunction expansion method is used

$$u(x,t) = \sum_{n=1}^{\infty} T_n(t) \sin\frac{n\pi x}{L} \tag{A-63}$$

which is the general solution form of Equation (A-61). $T_n(t)$ are unknown functions. Substitute this expansion into Equation (A-61) to get

$$\sum_{m=1}^{\infty} [T_m'(t) + (\beta_m^2 + b)\, T_m(t)] \sin\frac{m\pi x}{L} = -bw(x) \tag{A-64}$$

$$\beta_m = \frac{ma\pi}{L}$$

Multiply both sides of the equation above by $\sin\frac{m\pi x}{L}$ and integrate from x = 0 to x = L

$$\sum_{m=1}^{\infty} [T_m'(t) + (\beta_m^2 + b)\, T_m(t)] \int_0^L \sin\frac{m\pi x}{L} \sin\frac{n\pi x}{L} dx = -b \int_0^L \sin\frac{n\pi x}{L} w(x) dx \tag{A-65}$$

The orthogonality of the eigenfunctions gives

$$T_n'(t) + (\beta_n^2 + b)\, T_n(t) = w_n \tag{A-66}$$

$$w_n = -b\frac{\int_0^L \sin\frac{n\pi x}{L} w(x)dx}{\int_0^L \sin^2\frac{n\pi x}{L} dx} = \frac{2bR}{L^2}\int_0^L \sin\frac{n\pi x}{L}(x-L)dx = -\frac{2bR}{n\pi}$$

The general solution of the above ordinary differential equation can be obtained

$$T_n(t) = e^{-(\beta_n^2+b)t} T_n(0) + \frac{w_n}{\beta_n^2 + b}(1 - e^{-(\beta_n^2+b)t}) \tag{A-67}$$

Apply the I.C. in Equation (A-61)

$$u(x,0) = \sum_{n=1}^{\infty} T_n(0) \sin\frac{n\pi x}{L} = -w(x) \tag{A-40}$$

$$T_n(0) = -\frac{2}{L}\int_0^L \sin\frac{n\pi x}{L} w(x)dx = -\frac{2R}{n\pi} \tag{A-41}$$

Thus, the linear one-dimensional solution for neutron flux profile is obtained

$$\phi(x,t) = -\frac{R}{L}(x-L) + \sum_{n=1}^{\infty} T_n(t) \sin\frac{n\pi x}{L}\ , n = 1,2, \dots \tag{A-70}$$

where

$$T_n(t) = e^{-(\beta_n^2+b)t}T_n(0) + \frac{w_n}{\beta_n^2+b}\left(1 - e^{-(\beta_n^2+b)t}\right)$$

$$T_n(0) = -\frac{2R}{n\pi},\ w_n = -\frac{2bR}{n\pi},\ \beta_n = \frac{na\pi}{L},\ a = \sqrt{Dv}, b = \Sigma_a v$$

A.6 Finite Differential Solution of Coupled Neutron Radio-Thermo Equations

The governing equations of neutron coupled radio-thermo analysis are

$$\frac{1}{v_1}\frac{\partial \phi_1(x,t)}{\partial t} - \nabla \cdot \mathcal{D}_1(x,t)\nabla\phi_1(x,t) + \Sigma_{R1}\phi_1(x,t) = 0 \qquad \text{(A-71)}$$

$$\frac{1}{v_2}\frac{\partial \phi_2(x,t)}{\partial t} - \nabla \cdot \mathcal{D}_2(x,t)\nabla\phi_2(x,t) + \Sigma_{a2}\phi_2(x,t) = \Sigma_{s12}\phi_1(x,t) \qquad \text{(A-72)}$$

$$c_p\rho(x,t)\frac{\partial T(x,t)}{\partial t} = \nabla \cdot k(x,t)\nabla T(x,t) + 1.6 \times 10^{-13}\Sigma_c\mathcal{E}_b\phi_2(x,t) \qquad \text{(A-73)}$$

The continuous space domain and time domain, $x \in [0,L_x]$ and $t \in [0,L_t]$, are replaced by two sets of equally spaced mesh points

$$\begin{aligned} x_j &= (j-1)\,\delta x, \delta x = \frac{L_x}{N_x - 1}\ (j = 1,2,\dots,N_x) \\ t_n &= (n-1)\delta t, \delta t = \frac{L_t}{N_t - 1}(n = 1,2,\dots,N_t) \end{aligned} \qquad \text{(A-74)}$$

The backward Euler method is used for the finite difference spatial discretization of derivatives at t_{n+1}

$$\frac{\partial \phi}{\partial t} = \frac{\phi_j^{n+1} - \phi_j^n}{\delta t} \qquad \text{(A-42)}$$

$$\begin{aligned} \frac{\partial \phi}{\partial x}\left(\mathcal{D}\frac{\partial \phi}{\partial x}\right) &= \frac{1}{2(\delta x)^2}\left[\left(\mathcal{D}_{j+1}^{n+1} + \mathcal{D}_j^{n+1}\right)\left(\phi_{j+1}^{n+1} - \phi_j^{n+1}\right) + \left(\mathcal{D}_{j-1}^{n+1} + \mathcal{D}_j^{n+1}\right)\left(\phi_j^{n+1} - \phi_{j-1}^{n+1}\right)\right] \\ &= \frac{1}{2(\delta x)^2}\left[\left(\mathcal{D}_{j+1}^{n+1} + \mathcal{D}_j^{n+1}\right)\phi_{j+1}^{n+1} - \left(\mathcal{D}_{j+1}^{n+1} + 2\mathcal{D}_j^{n+1} + \mathcal{D}_{j-1}^{n+1}\right)\phi_j^{n+1} + \left(\mathcal{D}_{j-1}^{n+1} + \mathcal{D}_j^{n+1}\right)\phi_{j-1}^{n+1}\right] \end{aligned} \qquad \text{(A-76)}$$

$$\phi = \phi_j^{n+1} \qquad \text{(A-77)}$$

Then, Equation (A-71) to Equation (A-73) can be converted into discrete form at interior nodes (j = 2 to $N_x - 1$) as shown below

$$\begin{aligned} &-\frac{1}{2(\delta x)^2}\left(\mathcal{D}_{1,j+1}^{n+1}+\mathcal{D}_{1,j}^{n+1}\right)\phi_{1,j+1}^{n+1}+\left[\frac{1}{2(\delta x)^2}\left(\mathcal{D}_{1,j+1}^{n+1}+2\mathcal{D}_{1,j}^{n+1}+\mathcal{D}_{1,j-1}^{n+1}\right)+\frac{1}{v_1\delta t}+\Sigma_{R1}\right]\phi_{1,j}^{n+1} \\ &\qquad -\frac{1}{2(\delta x)^2}\left(\mathcal{D}_{1,j-1}^{n+1}+\mathcal{D}_{1,j}^{n+1}\right)\phi_{1,j-1}^{n+1}-\frac{\phi_{1,j}^{n}}{v_1\delta t}=0 \end{aligned} \tag{A-43}$$

$$\begin{aligned} &-\frac{1}{2(\delta x)^2}\left(\mathcal{D}_{2,j+1}^{n+1}+\mathcal{D}_{2,j}^{n+1}\right)\phi_{2,j+1}^{n+1}+\left[\frac{1}{2(\delta x)^2}\left(\mathcal{D}_{2,j+1}^{n+1}+2\mathcal{D}_{2,j}^{n+1}+\mathcal{D}_{2,j-1}^{n+1}\right)+\frac{1}{v_2\delta t}+\Sigma_{a2}\right]\phi_{2,j}^{n+1} \\ &\qquad -\frac{1}{2(\delta x)^2}\left(\mathcal{D}_{2,j-1}^{n+1}+\mathcal{D}_{2,j}^{n+1}\right)\phi_{2,j-1}^{n+1}-\Sigma_{s12}\phi_{1,j}^{n+1}-\frac{\phi_{2,j}^{n}}{v_2\delta t}=0 \end{aligned} \tag{A-44}$$

$$\begin{aligned} &-\frac{1.6\times 10^{-13}\Sigma_c\mathcal{E}_b\phi_{2,j}^{n+1}\delta t}{c_p\rho_j^n}-\frac{\delta t}{2(\delta x)^2c_p\rho_j^n}\left(k_{j+1}^{n+1}+k_j^{n+1}\right)T_{j+1}^{n+1} \\ &\qquad +\left[\frac{\delta t}{2(\delta x)^2c_p\rho_j^n}\left(k_{j+1}^{n+1}+2k_j^{n+1}+k_{j-1}^{n+1}\right)+1\right]T_j^{n+1} \\ &\qquad -\frac{\delta t}{2(\delta x)^2c_p\rho_j^n}\left(k_{j-1}^{n+1}+k_j^{n+1}\right)T_{j-1}^{n+1}-T_j^n=0 \end{aligned} \tag{A-80}$$

The equations at boundaries (j = 1 and j = N_x) depends on the specific B.C.s which is usually much simpler. The coupled system of equations can be expressed in an equivalent matrix form

$$H\begin{Bmatrix}\overline{\phi_1}\\ \overline{\phi_2}\\ \overline{T}\end{Bmatrix}=h \tag{A-81}$$

where *H* is the coefficient matrix and *h* is the known terms in the current time step.

A.7 Finite Differential Solution of Coupled Neutron and Gamma-Ray Radio-Thermo Equations

The governing equations of the neutron and gamma-ray coupled radio-thermo analysis are

$$\frac{1}{v_1}\frac{\partial\phi_1(x,t)}{\partial t}-\nabla\cdot\mathcal{D}_1(x,t)\nabla\phi_1(x,t)+\Sigma_{R1}\phi_1(x,t)=0 \tag{A-82}$$

$$\frac{1}{v_2}\frac{\partial\phi_2(x,t)}{\partial t}-\nabla\cdot\mathcal{D}_2(x,t)\nabla\phi_2(x,t)+\Sigma_{a2}\phi_2(x,t)=\Sigma_{s12}\phi_1(x,t) \tag{A-83}$$

$$\begin{gathered}\frac{1}{c}\frac{\partial\Phi_g(x,t)}{\partial t}-\nabla\cdot\mathbb{D}_g(x,t)\nabla\Phi_g(x,t)+\mu_g\Phi_g(x,t)=\sum_{g'=1}^{g-1}\mu_{sg'g}\Phi_{g'}+\Sigma_{\gamma g}\phi_2+\Sigma_{ing}\phi_1 \\ g=1,2,\dots,G\end{gathered} \tag{A-84}$$

$$
\begin{aligned}
c_p\rho(x,t)\frac{\partial T(x,t)}{\partial t}
&= \nabla\cdot k(x,t)\nabla T(x,t) + 1.6\times 10^{-13}\Sigma_c\mathcal{E}_b\phi_2(x,t) \\
&+ \sum_{g=1}^{G} 1.6\times 10^{-13}\mathcal{E}_{\gamma g}\mu_{ag}\Phi_g(x,t)
\end{aligned}
\tag{A-85}
$$

The same backward Euler method is used for the finite difference spatial discretization of derivatives at t_{n+1} as shown in Equation (A-74) to Equation (A-77). Then, Equation (A-82) to Equation (A-85) can be converted into discrete form at interior nodes (j = 2 to $N_x - 1$) as shown below

$$
\begin{aligned}
-\frac{1}{2(\delta x)^2}\left(\mathcal{D}_{1,j+1}^{n+1}+\mathcal{D}_{1,j}^{n+1}\right)\phi_{1,j+1}^{n+1} + \left[\frac{1}{2(\delta x)^2}\left(\mathcal{D}_{1,j+1}^{n+1}+2\mathcal{D}_{1,j}^{n+1}+\mathcal{D}_{1,j-1}^{n+1}\right)+\frac{1}{v_1\delta t}+\Sigma_{R1}\right]\phi_{1,j}^{n+1} \\
-\frac{1}{2(\delta x)^2}\left(\mathcal{D}_{1,j-1}^{n+1}+\mathcal{D}_{1,j}^{n+1}\right)\phi_{1,j-1}^{n+1} - \frac{\phi_{1,j}^{n}}{v_1\delta t} = 0
\end{aligned}
\tag{A-86}
$$

$$
\begin{aligned}
-\frac{1}{2(\delta x)^2}\left(\mathcal{D}_{2,j+1}^{n+1}+\mathcal{D}_{2,j}^{n+1}\right)\phi_{2,j+1}^{n+1} + \left[\frac{1}{2(\delta x)^2}\left(\mathcal{D}_{2,j+1}^{n+1}+2\mathcal{D}_{2,j}^{n+1}+\mathcal{D}_{2,j-1}^{n+1}\right)+\frac{1}{v_2\delta t}+\Sigma_{a2}\right]\phi_{2,j}^{n+1} \\
-\frac{1}{2(\delta x)^2}\left(\mathcal{D}_{2,j-1}^{n+1}+\mathcal{D}_{2,j}^{n+1}\right)\phi_{2,j-1}^{n+1} - \Sigma_{s12}\phi_{1,j}^{n+1} - \frac{\phi_{2,j}^{n}}{v_2\delta t} = 0
\end{aligned}
\tag{A-87}
$$

$$
\begin{aligned}
-\frac{1}{2(\delta x)^2}\left(\mathbb{D}_{g,j+1}^{n+1}+\mathbb{D}_{g,j}^{n+1}\right)\Phi_{g,j+1}^{n+1} + \left[\frac{1}{2(\delta x)^2}\left(\mathbb{D}_{g,j+1}^{n+1}+2\mathbb{D}_{g,j}^{n+1}+\mathbb{D}_{g,j-1}^{n+1}\right)+\frac{1}{c\delta t}+\mu_g\right]\Phi_{g,j}^{n+1} \\
-\frac{1}{2(\delta x)^2}\left(\mathbb{D}_{g,j-1}^{n+1}+\mathbb{D}_{g,j}^{n+1}\right)\Phi_{g,j-1}^{n+1} - \sum_{g'=1}^{g-1}\mu_{sg'g}\Phi_{g',j}^{n+1} - \Sigma_{ing}\phi_{1,j}^{n+1} - \Sigma_{\gamma g}\phi_{2,j}^{n+1} \\
-\frac{\Phi_{g,j}^{n}}{c\delta t} = 0
\end{aligned}
$$

$$
g = 1,2,\ldots,G
$$

$$
\begin{aligned}
-\frac{1.6\times 10^{-13}\Sigma_c\mathcal{E}_b\phi_{2,j}^{n+1}(x,t)\delta t}{c_p\rho_j^n} - \frac{1.6\times 10^{-13}\delta t}{c_p\rho_j^n}\sum_{g=1}^{G}\mathcal{E}_{\gamma g}\mu_{ag}\Phi_{g,j}^{n+1}(x,t) \\
-\frac{\delta t}{2(\delta x)^2 c_p\rho_j^n}\left(k_{j+1}^{n+1}+k_j^{n+1}\right)T_{j+1}^{n+1} \\
+\left[\frac{\delta t}{2(\delta x)^2 c_p\rho_j^n}\left(k_{j+1}^{n+1}+2k_j^{n+1}+k_{j-1}^{n+1}\right)+1\right]T_j^{n+1} \\
-\frac{\delta t}{2(\delta x)^2 c_p\rho_j^n}\left(k_{j-1}^{n+1}+k_j^{n+1}\right)T_{j-1}^{n+1} - T_j^n = 0
\end{aligned}
\tag{A-45}
$$

The equations at boundaries (j = 1 and j = N_x) depend on the specific B.C.s, which is usually much simpler. The coupled system of equations can be expressed in an equivalent matrix form

$$\mathcal{H}\begin{Bmatrix}\overline{\phi_1}\\ \overline{\phi_2}\\ \overline{\Phi_g}\\ \bar{T}\end{Bmatrix}=\mathscr{h} \tag{A-46}$$

where $\mathcal{H}$ is the coefficient matrix and $\mathscr{h}$ is the known terms in the current time step.

A.8 Derivation of the Multigroup Approximation of Neutron Diffusion Theory

The energy-dependent neutron diffusion equation can be obtained based on the neutron transport equation (Equation (4-1)):

$$\begin{aligned}\frac{1}{v}\frac{\partial\phi(\boldsymbol{r},\mathcal{E},t)}{\partial t}-\boldsymbol{\nabla}\cdot\mathcal{D}(\boldsymbol{r},\mathcal{E},t)\boldsymbol{\nabla}\phi(\boldsymbol{r},\mathcal{E},t)+\Sigma_t\phi(\boldsymbol{r},\mathcal{E},t)\\ =\int_{\boldsymbol{0}}^{\infty}\boldsymbol{d}\mathcal{E}'\,\Sigma_s(\mathcal{E}'\rightarrow\mathcal{E})\phi(\boldsymbol{r},\mathcal{E}',t)+\boldsymbol{S}(\boldsymbol{r},\mathcal{E},t)\end{aligned} \tag{A-90}$$

In order to eliminate the energy variable, the entire particle energy range is subdivided into G contiguous energy intervals ($\mathcal{E}_g$, $\mathcal{E}_{g-1}$), g = 2,3,…,G+1, and the whole equation is integrated over the gth energy group ($\mathcal{E}_g < \mathcal{E} < \mathcal{E}_{g-1}$):

$$\begin{aligned}\frac{\partial}{\partial t}\int_{\mathcal{E}_g}^{\mathcal{E}_{g-1}}\boldsymbol{d}\mathcal{E}\frac{1}{v}\phi(\boldsymbol{r},\mathcal{E},t)-\boldsymbol{\nabla}\cdot\int_{\mathcal{E}_g}^{\mathcal{E}_{g-1}}\boldsymbol{d}\mathcal{E}\,\mathcal{D}(\boldsymbol{r},\mathcal{E},t)\boldsymbol{\nabla}\phi(\boldsymbol{r},\mathcal{E},t)+\int_{\mathcal{E}_g}^{\mathcal{E}_{g-1}}\boldsymbol{d}\mathcal{E}\,\Sigma_t\phi(\boldsymbol{r},\mathcal{E},t)\\ =\int_{\mathcal{E}_g}^{\mathcal{E}_{g-1}}\boldsymbol{d}\mathcal{E}\int_{\boldsymbol{0}}^{\infty}\boldsymbol{d}\mathcal{E}'\,\Sigma_s(\mathcal{E}'\rightarrow\mathcal{E})\phi(\boldsymbol{r},\mathcal{E}',t)+\int_{\mathcal{E}_g}^{\mathcal{E}_{g-1}}\boldsymbol{d}\mathcal{E}\,\boldsymbol{S}(\boldsymbol{r},\mathcal{E},t)\end{aligned} \tag{A-91}$$

Define the neutron flux in group g as:

$$\phi_g(\boldsymbol{r},t)\equiv\int_{\mathcal{E}_g}^{\mathcal{E}_{g-1}}\boldsymbol{d}\mathcal{E}\,\phi(\boldsymbol{r},\mathcal{E},t) \tag{A-92}$$

Total cross section for group *g:*

$$\Sigma_{tg}\equiv\frac{1}{\phi_g}\int_{\mathcal{E}_g}^{\mathcal{E}_{g-1}}\boldsymbol{d}\mathcal{E}\,\Sigma_t\phi(\boldsymbol{r},\mathcal{E},t) \tag{A-93}$$

Diffusion coefficient for group *g:*

$$D_g\equiv\frac{\int_{\mathcal{E}_g}^{\mathcal{E}_{g-1}}\boldsymbol{d}\mathcal{E}\,\mathcal{D}(\boldsymbol{r},\mathcal{E},t)\boldsymbol{\nabla}\phi(\boldsymbol{r},\mathcal{E},t)}{\int_{\mathcal{E}_g}^{\mathcal{E}_{g-1}}\boldsymbol{d}\mathcal{E}\,\phi(\boldsymbol{r},\mathcal{E},t)} \tag{A-94}$$

Neutron speed for group *g:*

$$\frac{1}{v_g} \equiv \frac{1}{\phi_g} \int_{\mathcal{E}_g}^{\mathcal{E}_{g-1}} \boldsymbol{d}\mathcal{E} \frac{1}{v} \phi(\boldsymbol{r}, \mathcal{E}, t) \tag{A-95}$$

Group-transfer cross section*:*

$$\Sigma_{sg'g} \equiv \frac{1}{\phi_{g'}} \int_{\mathcal{E}_g}^{\mathcal{E}_{g-1}} \boldsymbol{d}\mathcal{E} \int_{\mathcal{E}_g}^{\mathcal{E}_{g'-1}} \boldsymbol{d}\mathcal{E}' \, \Sigma_s(\mathcal{E}' \to \mathcal{E}) \phi(\boldsymbol{r}, \mathcal{E}', t) \tag{A-96}$$

Then the multigroup diffusion equations are*:*

$$\frac{1}{v_g} \frac{\partial \phi_g}{\partial t} - \nabla \cdot D_g \nabla \phi_g + \Sigma_{tg} \phi_g = \sum_{g'=1}^{G} \Sigma_{sg'g} \phi_{g'} + S_g \tag{A-97}$$
$$g = 1,2, \ldots, G$$

In order to calculate those group parameters defined from Equation (A-92) to Equation (A-96), the neutron flux ϕ_g is needed, which, however, is the function to be solved in the first place by discretizing the energy-dependent diffusion equation. In practice, some approximation for the neutron flux density within a group must be made in order to obtain these parameters.